I. Theory of Laser Driven Molecular Wires.
II. Light Diffraction by Colloidal Crystals – Numerical Simulations for Realistic Finite Systems Using Single Scattering Theory.

by

Alexander Tikhonov

M. Sc., Moscow Institute of Physics and Technology, Moscow, Russia, 1991

Submitted to the Graduate Faculty of

Arts and Sciences in partial fulfillment

of the requirements for the degree of

Doctor of Philosophy

University of Pittsburgh

2006

UNIVERSITY OF PITTSBURGH

FACULTY OF ARTS AND SCIENCES

This dissertation was presented

by

Alexander Tikhonov

It was defended on

October 27, 2006

and approved by

Prof. S. Asher

Prof. K. Jordan

Prof. H. Petek

Dissertation Advisor: Prof. R. Coalson

I. Theory of Laser Driven Molecular Wires.

II. Light Diffraction by Colloidal Crystals – Numerical Simulations for Realistic Finite Systems Using Single Scattering Theory.

Alexander Tikhonov, Ph. D.

University of Pittsburgh, 2006

Part I considers electron transport through a molecular bridge coupled to two metal electrodes in the presence of a monochromatic ac radiation field. Coherent current flow through the wire is calculated within a nondissipative one-electron tight binding model of the quantum dynamics. Using Floquet theory, the field-driven molecular wire is mapped to an effective time-independent quantum system characterized by a tight-binding Hamiltonian with the same essential structure as the nondriven analog. Thus, the Landauer formalism and scattering Green's Function methods for computing current flow through the wire, which have been profitably applied to the molecular wire problem in the absence of driving, can also be used to analyze the corresponding field-driven system.

The theory developed here is applied to an experimentally relevant system, namely a xylyl-dithiol molecule in contact at either end with gold electrodes. Net current through the wire is calculated for two – STM and molecular junction - configurations of the electrode-wire-electrode system for a range of experimental inputs, including bias and the intensity and frequency of the laser. Via absorption/emission of photons, the electron tunneling occurs through an interference of many pathways and may lead to a significantly enhanced laser-driven current at experimentally accessible laser field strengths.

In **Part II** we apply a single particle scattering methodology to calculate diffraction efficiencies of finite Crystalline Colloidal Arrays (CCA's). We developed an extension of the well-known Kinematic theory and tested it by comparing computed light scattering efficiencies with exact results for 1D slab model. We discuss some applications of the method to finite CCA's of different shapes and sizes. In particular, the dependence of diffraction intensities on the incident

angle is analyzed near the Bragg diffraction maximum for several different crystal planes. We also study the effect of the incident beam shape and cross sectional profile on the CCA diffraction. Finally, the effective penetration depth for the incident light is calculated and compared for several incident directions, and the effect of stacking faults on diffraction efficiencies is analyzed using the methodology developed herein..

TABLE OF CONTENTS

List of tables

List of figures

PREFACE

This dissertation contains two separate topics, therefore, I organize them into two separate parts, PART 1 and PART 2. Each part contains a separate introduction and separate bibliography list.

Some of the work presented in this dissertation was published, specifically, for the "Laser driven molecular wires", the material of Chapters 2 and 3 was published in two correspondent papers:

- A. Tikhonov, R. D. Coalson, Y. Dahnovsky, J. Chem. Phys., *"Calculating electron transport in a tight binding model of a field-driven molecular wire: Floquet theory approach"*, **116**, 10909 (2002).
- A. Tikhonov, R. D. Coalson, Y. Dahnovsky, *"Calculating Electron Current in a Tight-Binding Model of a Field-Driven Molecular Wire: Application to Xylyl-Dithiol"*, J. Chem. Phys. **117,** 567 (2002).

  The material in Chapter 4 is unpublished.

In the second project "Light Diffraction by Colloidal Crystals – Numerical Simulations for Realistic Finite Systems Using Single Scattering Theory" most of the material in Chapters 6 and Chapters 7 is unpublished, but there are two relevant publications:

- S.A. Asher, J.M. Weissman, A. Tikhonov, R.D. Coalson and R. Kesavamoorthy, *"Diffraction in Crystalline Colloidal-Array Photonic Crystals"*, Phys. Rev. E, **69**, 066619 (2004).
- C. Reese, A. Mikhonin, M. Kamenjicki, A. Tikhonov and S.A. Asher, *"Nanogel Nanosecond Photonic Crystal Optical Switching"*, J. Am. Chem. Soc., **126**, 1493 (2004).

Part 1

Theory of Laser Driven Molecular Wires.

Chapter 1. Introduction

Conduction of electrons through a single molecule connecting two metal electrodes has received significant attention recently, fueled by the drive toward further miniaturization of electronics [1-6]. Simple molecular electronic devices usually consist of individual molecules or small groups of molecules sandwiched between metal electrodes. The field of development of such molecular electronic devices has been very active lately, and many devices have been proposed. They include rectifiers, light-emitting diodes, single-molecule transistors and molecular switch tunnel junctions [1, 7-9]. The most basic element of molecular electronics is a single-molecule transport junction, and both theoretical and experimental studies of charge transport though the junctions are of fundamental importance.

The nanoscale transport junctions considered most often are a single-molecule junction or junction through a self-assembled monolayer of molecules. In the former case the single molecule is connecting two metal (typically noble metal) electrodes (Fig. 1.1), in the later case many molecules self-assemble on a metallic surface and electronic transport occurs through simultaneously several molecules. In Fig. 1.1 we sketch the typical experimental molecular junction setup, where organic xylyl-dithiol molecule is attached between two metal leads, and electrical current results from the tunneling through the molecular bridge under the driving force of external constant voltage potential.

There are many experimental setups to study charge transport through molecular junctions [1]. Depending on type of tunnel junctions typical experimental studies use scanning tunneling microscopies (STM) and mechanical break junctions [1, 10, 11]. The experimental configuration consisting of an STM tip in proximity to an adsorbate on a metal surface provides a good example of an asymmetric electrode-molecular wire-electrode system, where the molecule is much closer to one electrode then to another. Current-voltage (I-V) characteristics can be recorded when the tip is positioned above the adsorbate. In the case of mechanical break

junction the molecule is chemisorbed to both electrodes, resulting in strong interaction between molecule and metals. A related problem of recent interest is conductance through mesoscopic systems composed of semiconductor heterostructures [6, 7]. Spectroscopic techniques have been extensively utilized to probe the features of charge transfer through the molecule-metal lead interface and details of electronic structure [14-16].

The theory of conductance through molecular wires is well developed. For the STM geometry of the junction perturbation theory based on the Tersoff-Hamann approach has been extensively used [17]. Assuming a weak coupling between the tip and the molecule on the surface, the tunneling current is proportional to the local density of surface states, evaluated at the position of the tip at the Fermi energy. A non-perturbative approach, in which the relevant electron transport is considered as a one-electron scattering process with the molecular bridge treated in a tight-binding approximation, has also seen wide application [18-22]. Although lacking the sophistication and accuracy of more advanced ab-initio electronic structure methods, the tight-binding based scattering formalism was very successful in developing qualitative understanding of physical effects affecting the current through molecular wires. In this approach, one examines how the molecular orbitals of a bridge line up relative to the Fermi energy of the metal leads, which connect to an external (macroscopic) circuit. As a result of attaching the molecule to the leads, the electron charge rearranges, the geometry of the molecule reorganizes, and an electrostatic potential develops across the junction. Because of the large polarizability of the metal, an image charge is formed, thereby affecting the populations and charge distribution near the interface with the molecule. Upon applying a constant voltage bias between the electrodes, current flows through the junction, its value determined primarily by the relative position of the molecular levels with respect to the Fermi energy at the leads and by the magnitude of the coupling between the molecule and the leads.

As a result, the magnitude of the current is largely an interface problem and very sensitive to the details of connection between the molecule and the leads. More advanced electronic structure methods, usually based on density-functional methods have been applied to the problem [23-27], but the agreement between theory and experiment remains tenuous. The main problem is argued to lie in the difficulties of experimental reproducibility of the parameters of the junction, and the large sensitivity of the current to such parameters.

When the bridge molecule is relatively short (on the order of *1* nm or shorter) and the gap between the molecular levels and the Fermi energy is larger than the applied voltage bias, the charge transfer across the junction is said to be non-resonant, i. e., in the superexchange regime. The principal electronic transport mechanism in this case is believed to be coherent elastic (ballistic) tunneling and is usually described by the Landauer formalism [12], in which the conductance g at the Fermi energy E_F is given:

$$g = \frac{2e^2}{\hbar} T(E_F) \tag{1.1}$$

where T is the transmission function, and e and $\hbar$ are the electronic charge and Planck's constant, respectively. The maximum conductance per molecule, corresponding to the $T=1$ is $g = 2e^2/\hbar = (12.9\,\mathrm{k\Omega})^{-1}$, and is sometimes called quantum of conductance. The total current I flowing through the junction is given in the Landauer formalism by the formula

$$I = \frac{e}{\hbar} \int dE \big(f_L(E) - f_R(E) \big) T(E) \tag{1.2}$$

where f_L and f_R are the occupation probabilities (Fermi functions) of states in the left and right electrodes.

During coherent elastic tunneling an electron never localizes on the bridge. This is a dominating transport mechanism for relatively short wires, where the "tunneling traversal time" is less then *~1 fs* and much shorter then the typical time scale for nuclear motion [28]. For longer wires and resonant charge transfer (occurring for at small energy difference between the bridge molecular levels and Fermi energy) the tunneling time can be substantially lengthened and inelastic tunneling/dephasing may become significant. In inelastic electronic "hopping" the electron actually resides on the bridge and "hops" between the bridge sites as a result of thermal activation [29, 30]. Dynamic localization of the electron on the femtosecond time scale, polaron formation and the strength of nuclear-electronic coupling has recently been investigated via two-photon photoemission [14-15].

In the Landauer approach the leads are assumed to be in their own thermal equilibrium, characterized by the Fermi population distribution and unaffected by the tunneling process. It is also assumed, that the tunneling process is independent on the population distribution on the leads, and disregards effect of electron-electron correlations on the tunneling process. Recent calculations based on an approach that is more rigorous than the Landauer approach, namely, the

non-equilibrium green function (NEGF) formalism [31, 32], have been carried out and the model has been extended to include electron-phonon interactions [33].

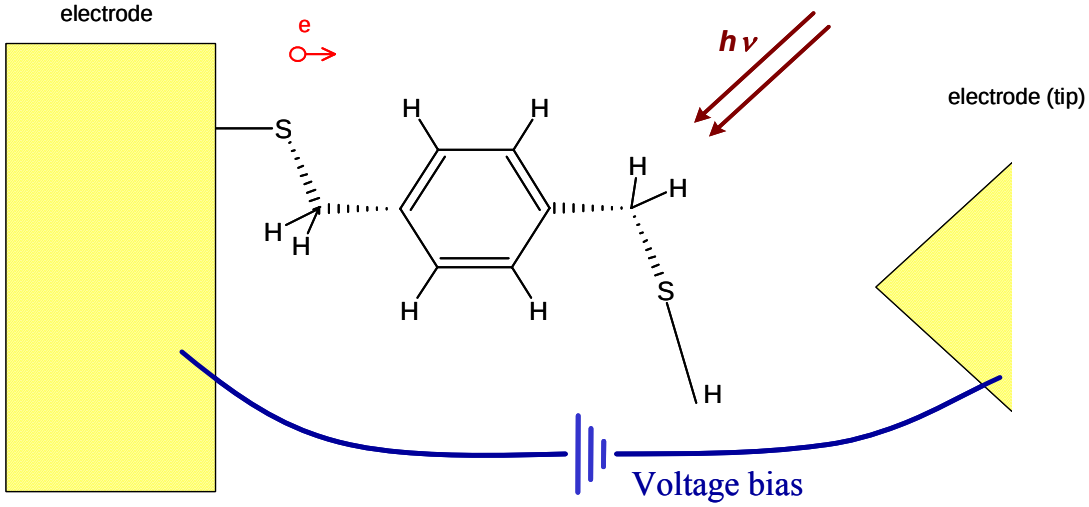

Figure 1-1. Xylyl-dithiol organic molecule sandwiched between two metal electrodes. Asymmetric connection between the molecule and electrodes is shown – the molecule is closer to the left then to the right electrode. Electrons tunnel trough the molecule under the driving force of external voltage bias. Illuminating the junction with the external laser field modifies the electronic current through the system.

In the present work we explore the prospect of controlling the current through a molecular junction by imposing a monochromatic *ac* electromagnetic field. Previous theoretical studies suggest that illumination of a molecular electron transfer system by a laser field can alter its conductance properties. Specific motifs that have been studied in this context include: long range metal-metal intramolecular electron transfer complexes [34-36], double-barrier semiconductor heterostrucures [37], periodically driven scattering in one dimension [38, 39], adiabatic pumping [40, 41], quantum coherent control [42] and systems in which the gap between a metal surface and an STM tip (with no intervening adsorbate) is illuminated [43]. For a recent review of driven quantum transport and an extensive list of references we refer the reader to reference [44].

To date, experimental evidence for *ac* field modified transfer of electron transfer/transport is rather scant. However, one encouraging example is provided by the studies of B. J. Keay and coworkers [13]. Upon illumination of a multi quantum well semiconductor

heterostructure with an appropriate monochromatic radiation source, they were able to strongly alter the current flow through the heterostructure. In particular, these authors were able to reverse the direction of current flow relative to the direction dictated by an applied *dc* bias potential. These findings provide some motivation to search for similar effects in molecular wire systems. Another experimental achievement in mesoscopic driven transport was reached in coherent coupling of quantum dots [45, 46]. Photocurrent measurements in metal-insulator-metal junctions under illumination with ultra-short laser pulses reveal that both field-assisted tunneling and photoemission of excited electrons are dominant transport mechanisms [47].

The purpose of the present report is to develop a scattering theory for the effect of radiation on coherent electronic conduction between two metal electrodes. We also apply the developed theory to a simple organic molecule ("molecular wire") connecting two gold electrodes, and discuss an interplay of different physical mechanisms affecting the total field-driven current.

When an external radiation is applied to the molecular junction, one can distinguish several physical processes affecting the electronic transport. Field assisted tunneling can modify the probability of the electron transmission through the junction. In another mechanism, a laser field can photoemit electrons from one electrode to another. The strong interaction of laser field with the metal material of a nano-junction results in strong enhancement of the local electromagnetic field, creation of various excitations near the junction and modification of the population distribution of electrons [48, 49] and their field-induced localization [50], which may also affect the current through the junction.

We outline here a theoretical framework for understanding field assisted tunneling charge transport mechanism through a molecular wire in the presence of a monochromatic *ac* driving field. For linguistic simplicity, we shall refer to this as a "laser field". We adopt the simple one-electron theoretical model, assuming, similar to the Landauer picture, the following set of simplifications: coherent electronic transport through the junction, no electron-electron correlations and the absence of environmental coupling (e.g., disorder, dissipation, etc.). We assume the simplest possible model of metal leads electronic population distribution by disregarding the effect of the adsorbed molecule on the metal leads population. The last assumption can be later corrected by adding into the model more realistic population distribution profile, accounting for adsorbate induced population modification, image and surface states. We

also disregard the modification of electronic populations by the laser field on both the molecule and the leads, and assume the equilibrium Fermi distribution of a non-driven isolated system. The importance of both adsorbate and laser field induced modification of the electron population distribution in the leads has been demonstrated in two photon photoemission spectroscopic studies [14, 15].

The assumption of coherent electronic transport as a dominating transport mechanism is valid for a small molecular chains conducting in non-resonant superexchange regime. A strong laser field may open up the resonant conducting channels, where electrons in the lead absorb/emit photons and resonantly couple to the molecular levels of the bridge. This resonant tunneling may lead to the increase of the "tunneling time" and consequent increase in the coupling between the electron and nuclear motion. Thus, reports of many orders of magnitude of increase in field-assisted electron transfer rates by considering only coherent one-electron charge transport picture should be taken with a "grain of salt" – the dissipation and dephasing as well as coulomb blockade effects may considerably change the magnitude of the enhancement effect.

As a first step toward the understanding of realistic picture of a current through the molecular wires illuminated by the laser field, we focus here on the understanding of a field assisted tunneling within a nondissipative one-electron tight binding model of the quantum dynamics. Using Floquet theory, the field-driven molecular wire is mapped to an effective time-*in*dependent quantum system characterized by a tight-binding Hamiltonian with the same essential structure as the nondriven analog. Thus, the scattering Green's Function methods and Landauer formula for computing current flow through the wire, which have been profitably applied to the molecular wire problem in the absence of driving, can also be used to analyze the corresponding field-driven system.

For a Hamiltonian with periodic time dependence, one can apply the Floquet theory to map the time-dependent problem into the effective time-independent one, at the cost of increasing the dimensionality of the relevant effective Hamiltionian. The Floquet theory [51, 52, 44] is based on the Bloch-Floquet theorem, which states that eigensolutions of differential equations with periodic coefficients may be expressed as a product of plane waves and lattice-periodic functions. Thus any solution for a Schrödinger equation can be expressed as a linear combination of Bloch functions

$$e^{-i\varepsilon_a t/\hbar}\phi_a(t) \tag{1.3}$$

where the functions $\phi_a(t)$ are time periodic with the same periodicity as the external driving field, and the exponential phase factor contains the quasi-energy ε_a which can be selected to lie within the first Brillouin zone.

Consequently, $\phi_a(t)$ periodic functions can be expanded into appropriate Fourier series, and the arbitrary wave function solution of the Schrödinger equation $\psi(t)$ can be expanded in corresponding plane waves:

$$\psi(t) = \sum_{m=-\infty}^{\infty} \varphi_m(t) e^{im\omega t} \tag{1.4}$$

Inserting these expansions into the differential equation results in an infinite matrix-eigenvalue problem, which, suitably truncated, provides the expansion coefficients φ_m for every quasi-energy $m\omega$. Following our main source of the insight about the Floquet method [51], we call φ_m as "Floquet states" corresponding to the "Floquet replica" m. We note, that this notation is different from the more popular notation [44] denoting $\phi_a(t)$ and ε_a of the Bloch function (1.3) as correspondingly "Floquet states" and "quasienergies".

The formalism we develop here is exact for the one-electron tight-binding model, in the sense that the scattering Green's function formula applied to the effective time-independent Hamiltonian gives an exact solution for motion under the original time-dependent Hamiltonian. We tested this numerically by comparing the tunneling rates obtained by the scattering Green's function formula with those obtained by exact numerical integration of time-dependent Schrödinger equation.

We extensively studied first a simple model "toy" system, with the bridge molecule consisting of only several sites (states), and then studied a realistic molecular wire system consisting of a xylyl-dithiol molecule coupled electronically to two gold electrodes. We have chosen the xylyl-dithiol molecule because it has been extensively studied both experimentally [11, 19, 53] and theoretically [19, 54, 55] and provides a concrete example on the basis of which to estimate parameters in the system Hamiltonian and to test convergence issues associated with the theoretical analysis.

The current through the molecular wire in the absence of laser field is determined by the summation of the tunneling rates of all electrons located in the gap between the Fermi energies of the metal electrodes. By illuminating the molecular junction with a laser field we expand the

number of electronic states participating in the current. The electrons, even located far bellow the Fermi energies of both electrodes, can absorb one or several photons, tunnel through the molecular wire and end up on the empty states of the opposite electrode.

We consider two different geometries of the molecular wire/electrode system: 1) A symmetric configuration in which the contacts with the gold electrode on either side of the molecule are equivalent. Such a situation obtains, approximately, in molecular break-junction experiments. Hence will shall term this the "break junction" configuration. 2) An asymmetric configuration in which the left contact distance is small (ca. 2 Å), corresponding to chemisorption of the thiol group on one end of the xylyl-dithiol to a gold electrode, while the other contact distance is considerably larger (ca. 5 Å), corresponding to the location of an STM tip. This will be designated as an "STM" configuration. The geometrical differences in these electrode/molecule systems lead to different interactions with the laser field, which in turn results in different induced currents, and to the so-called "ratchet" effect – existence of directed electronic motion (field-induced current) at zero *dc* voltage bias as a result of interference of many *ac* field induced tunneling processes.

We expand our theoretical treatment by developing perturbative theory based on the partitioning of the full Floquet Hamiltonian. This perturbation theory expansion allows us to simplify the full Floquet Hamiltonian and provides a clear physical description of field-driven electron tunneling as an interference of many pathways. Each such process has a specific physical interpretation as the electron site to site "hop" accompanied by possible photon absorption-emission. We use a diagrammatic technique to identify all possible pathways for electron transport and assign specific algebraic term to each such pathway.

We test this perturbation approach by analyzing tunneling rates through the xylyl-dithiol molecule connecting two gold electrodes and show that for a relatively strong laser field intensities of less then 10^7 *V/cm* by taking into account just the first and second perturbation terms the exact tunneling rates are well numerically reproduced.

Other Floquet based methodologies have been developed [58-61] similar to our approach to the problem of driven molecular wires. In ref. [58], the time-dependent part of Hamiltonian was considered as a small perturbation, making the approach applicable for only small intensities of laser fields. The expression for a current driven by a periodic but otherwise arbitrary *ac* field was derived in [60, 61] and the formulas were extended to include the phonon damping. A rather

simple case of the molecular wire was studied – the simple model for a wire consisting of several atomic sites, where the energies of the first and last sites of a molecular bridge were placed near the Fermi energies of the leads, and other bridge states are placed much higher then the Fermi energy. The coupling between the wire and the leads was considered as a small perturbation. As a result of these approximations, there is a single dominating tunneling channel which can be described simply by the rotating-wave approximation. In contrast, our studies with the realistic xylyl-dithiol molecular wire showed that the bridge energy level structure is rather dense and complicated, and the current is best described as an interference of many resonant channels. Since the electrons in the metal occupy the wide range of states below the Fermi energy, there are always many possible electrons in the leads, which can absorb/emit photons and resonantly jump to one of the bridge molecular level. Thus, the photon assisted electron transfer between the leads and the bridge is important for realistic molecule, and the approximation of weak interface coupling is perhaps overly simplistic.

The outline of this part of the theses is as follows. In chapter 2 we develop methodology and test the method on the simple model. In section 2.1 we briefly review the one-electron tight binding model of electron transport through a (non-driven) molecular wire connected to two metal electrodes, ignoring, for simplicity, dissipative coupling to non-electronic environmental degrees of freedom. We summarize the description of current flow through the wire, focusing on a well-known Green's function based formula that prescribes the magnitude of this current in terms of the properties of the bridge molecule, the metal electrodes, and the electronic coupling between them. In Section 2.2, we introduce an applied monochromatic *ac* electric field (provided by a laser), and indicate how this modifies the relevant tight-binding Hamiltonian. Using Floquet theory, we then show in Sect. 2.3 how to map the time-dependent Hamiltonian which describes the field-driven system precisely into a time *in*dependent Hamiltonian corresponding to an augmented state space. The essential structure of this Floquet Hamiltonian is identical to that of the standard (non-driven) molecular wire problem -- only the details of the effective molecular wire, the reservoirs and the coupling between them change. Thus, the Green's function formula for current flow through the non-driven wire can be readily adapted to calculate current flow for the *field driven* wire. In Section 2.4, we provide an approximate way to simplify the Floquet Hamiltonian associated with the field-driven system which enables the current to be analyzed in terms of a physically appealing “independent channel” picture. The conditions of validity of the

independent channel approximation (ICA) are discussed. In Section 2.5, prototypical numerical illustrations are presented for a simple model of a field-driven wire. Exact numerical integration of the time-dependent Schrödinger Equation is compared to Green's function analysis of the Floquet Hamiltonian -- good agreement is obtained. In addition, results of the ICA are presented to illustrate the range of its accuracy.

The organization of the chapter 3 is as follows. In Sect. 3.1, elementary quantum chemical calculations are performed to determine the parameters which enter into the tight-binding model of xylyl-dithiol coupled to gold electrodes. Next, in Sect. 3.2, we present some tests of the accuracy of the Floquet/Green's function analysis of current flow through the field-driven wire. It will be seen that this procedure, carried out to full numerical convergence, provides an exact description of the field-driven system. This motivates our reliance on Floquet/Green's function analysis for the main results of the chapter, which are presented in Sect. 3.3. Here we compute electric current through the xylyl-dithiol wire for both break-junction and STM configurations. A variety of experimental inputs (applied *dc* voltage, laser amplitude and frequency) are considered. We highlight conditions which enable significant laser enhancement of electric current through the wires.

Finally, in chapter 4 we use perturbative approach to structure and analyze the Floquet effective Hamiltonian and employ a diagrammatic technique to describe the total tunneling rates as an interference of many channels, each channel representing a specific tunneling process entailing the absorption/emission of a specific number of photons. Then we test this method by comparing the exact and perturbative theories numerical results for both “toy” and realistic xylyl-dithiol molecular wires. We show that in the case of an xylyl-dithiol molecular bridge, which comprises many tight-binding states, and for the laser field intensities less then 10^7 *V/cm,* the exact result is numerically reproduced by taking into account just the first two terms in the perturbation series.

Chapter 2. Calculating electron transport in a tight binding model of a field-driven molecular wire: Floquet theory approach

2.1 TIGHT-BINDING MODEL OF A (NONDRIVEN) MOLECULAR WIRE

In this section we review relevant features of an electron transfer system consisting of a molecule ("molecular wire") bridging between two metal electrodes in the presence of an applied *dc* voltage. Additional features associated with illumination of this system via monochromatic light are discussed in the next section.

A simple 1-electron (Tight Binding or Hückel) model of a molecular wire [18-21] is schematically depicted in Fig. 2.1. It features two reservoirs, Left and Right, which represent metal electrodes. Connecting them is a molecular bridge ("wire"). The overall system Hamiltonian is defined by the following features. The Left reservoir states are denoted as $|i\rangle$ and have energy ε_i. They are not directly coupled to each other. The same is true of the Right reservoir states, which are denoted as $|f\rangle$ and have energy ε_f. Left and Right reservoir states are not coupled directly to each other. The molecular electronic structure is also represented by a Tight Binding Hamiltonian. The N atomic orbitals are denoted $|I\rangle$, with site energies ε_I. These states are coupled by matrix elements $V_{I,J}$. Finally, coupling between the L-reservoir state i and atomic orbital I on the molecular bridge is designated by $V_{i,I}$. Analogously, $V_{f,I}$ designates coupling between R-reservoir state f and bridge atomic orbital I.

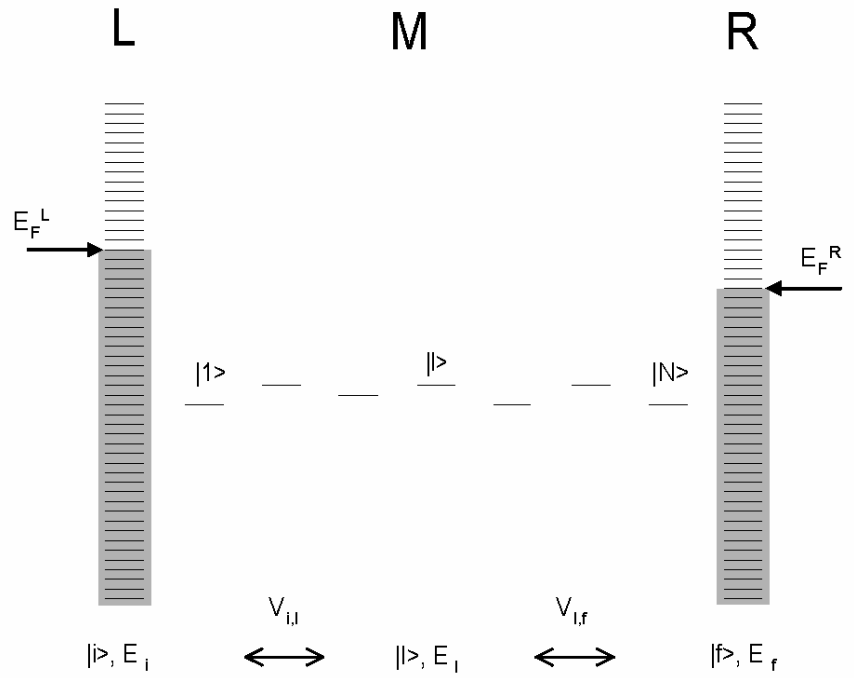

Figure 2-1. Energy level and coupling diagram for a non-driven molecular wire coupled to reservoirs of metallic states. Positions of Left and Right Fermi levels [for applied voltage $V_{ap} = (E_F^L - E_F^R)/e_0$] are indicated.

The site energy levels just introduced refer to the system in the absence of any external perturbations. In order to get current to flow through the wire, some external field must be applied. In the usual case, a static, *dc*, field is applied across the metal electrodes using a battery [1-6, 10-12, 18-23]. Such a static field modifies the electronic Hamiltonian, and in particular, in the one-electron picture adopted here, changes the site energies associated with the Tight Binding model. We shall term the *dc* field-dependent site energies as E_i for the Left reservoir, etc. If the electric potential associated with the applied electric field is designated as $\phi(\vec{r})$, then:

$$\begin{aligned} E_i &= \varepsilon_i \\ E_I &= \varepsilon_I - e_0\phi_{I,I} \\ E_f &= \varepsilon_f - e_0 V_{ap} \end{aligned} \qquad (2.1)$$

where e_0 is the magnitude of the electronic charge, and $\phi_{I,I} = \langle I | \phi(\vec{r}) | I \rangle$. Here the electric potential ϕ is taken, without loss of generality, to be zero throughout the Left reservoir and have

the value V_{ap} throughout the Right reservoir. The precise functional form of ϕ is complicated by a number of factors [19-21], but does not affect the formal development of the one-electron model of molecular wire theory.

Bearing this shift in the "bare" site energies (i.e., the molecular site energies in the absence of applied *dc* voltage) in mind, the Hamiltonian operator for the system when a static voltage is applied across the electrodes reads:

$$\hat{H} = \sum_i E_i |i\rangle\langle i| + \hat{H}^M + \sum_f E_f |f\rangle\langle f| + \sum_I \sum_i V_{i,I} (|i\rangle\langle I| + |I\rangle\langle i|) + \sum_I \sum_f V_{f,I} (|f\rangle\langle I| + |I\rangle\langle f|) \tag{2.2}$$

with the bridge Hamiltonian given by:

$$\hat{H}^M = \sum_I E_I |I\rangle\langle I| + \sum_{I \neq J} V_{I,J} |I\rangle\langle J| \tag{2.3}$$

Associated with the Hamiltonian H is a state vector of the form

$$|\psi(t)\rangle = \sum_i c_i(t)|i\rangle + \sum_I c_I(t)|I\rangle + \sum_f c_f(t)|f\rangle \tag{2.4}$$

Thus the time dependent Schrödinger Eq. (SE), $i|\dot{\psi}(t)\rangle = \hat{H}|\psi(t)\rangle$, is converted into a set of first order ODE's of the form $i\dot{c}_\alpha(t) = \sum_\beta H_{\alpha,\beta} c_\beta(t)$ with $\alpha, \beta = i, I, f$. [Note: we set $\hbar = 1$ throughout.]

The basic dynamical scenario of interest is as follows. The system (electron) is prepared at $t = 0$ in a single state i_0 of the L-reservoir. We wish to calculate the time evolution of the system for $t > 0$, and in particular the probability that the electron makes a transition to state f_0 of the R-reservoir, i.e., $|c_{f_0}(t)|^2$. From this we can compute the electrical current through the wire.

Formally, $c_{f_0}(t) = \langle f_0 | \exp(-i\hat{H}t) | i_0 \rangle$, and thus is related to the (retarded) Green's function [62] of the system via:

$$\int_0^\infty dt e^{iEt-\eta t} \langle f_0 | e^{-i\hat{H}t} | i_0 \rangle = \frac{1}{i} \langle f_0 | (\hat{H} - E - i\eta)^{-1} | i_0 \rangle \tag{2.5}$$

with $\eta \to 0^+$. The structure of the Hamiltonian enables a useful simplification of the overall Green's function, namely:

$$\int_0^\infty dt\, e^{iEt-\eta t} \langle f_0 | \exp(-i\hat{H}t) | i_0 \rangle = \frac{1}{E_{i_0} - E} \frac{1}{E_{f_0} - E} \vec{v}^L \cdot \mathbf{g}(E) \cdot \vec{v}^R \tag{2.6}$$

with $\mathbf{g}$ the Green's function for a modified version of the *bridge* Hamiltonian. Specifically, it is the $N \times N$ matrix:

$$\mathbf{g}(E) = \left[\mathbf{H}^M - \mathbf{\Sigma}(E) - E \right]^{-1} \tag{2.7}$$

where $\mathbf{H}^M$ is the matrix representing the bridge Hamiltonian (Eq. (2.3)), and $\mathbf{\Sigma}$ is an E-dependent "self-energy" matrix, which decomposes as

$$\mathbf{\Sigma}(E) = \mathbf{\Sigma}^L(E) + \mathbf{\Sigma}^R(E), \tag{2.8}$$

with elements:

$$\Sigma^L_{I,J}(E) = \sum_i \frac{V_{i,I} V_{i,J}}{E_i - E - i\eta}, \tag{2.9}$$

and likewise for $\mathbf{\Sigma}^R(E)$. Furthermore, the elements of the *N-d* vector $\vec{v}^L$ are given by $v^L_I = V_{i_0,I}$, and likewise for $\vec{v}^R$.

The Fourier-Laplace (FL) transform given in Eq. (2.6) can be inverted to yield the time evolution of $c_{f_0}(t)$:

$$c_{f_0}(t) = e^{-iE_{f0}t} \int_0^t dt' e^{i(E_{f0}-E_{i0})t'} \int_0^{t'} dt'' g(t'-t'') e^{iE_{i0}(t'-t'')} \tag{2.10}$$

where $g(t)$ is the inverse FL transform of $\vec{v}^L \cdot \mathbf{g}(E) \cdot \vec{v}^R$, i.e.:

$$\int_0^\infty dt\, g(t) e^{iEt-\eta t} = \vec{v}^L \cdot \mathbf{g}(E) \cdot \vec{v}^R \tag{2.11}$$

Now, if the set of L,R-reservoir states is dense, the function $g(t)$ will decay to zero after some transient time. If the set of reservoir states is *infinitely* dense, $g(t)$ will then remain zero for all time. If it is not, then there will be some "recurrence time" at which $g(t)$ becomes nonzero again. However, for a sufficiently dense set of reservoir states this recurrence time can be pushed off to (almost) infinity -- longer than the time scale of the experimental measurement.

So, on the "intermediate" time scale -- after $g(t)$ has decayed to zero, but before it recurs,

$$|c_{f_0}(t)|^2 = |\vec{v}^L \cdot \mathbf{g}(E_{i_0}) \cdot \vec{v}^R|^2 \frac{\sin^2[(E_{f_0}-E_{i_0})t/2]}{[(E_{f_0}-E_{i_0})/2]^2} \rightarrow 2\pi t\, |\vec{v}^L \cdot \mathbf{g}(E_{i_0}) \cdot \vec{v}^R|^2\, \delta(E_{f_0}-E_{i_0}) \tag{2.12}$$

where the arrow recognizes that for sufficiently long time the factor $\dfrac{\sin^2[(E_{f_0}-E_{i_0})t/2]}{[(E_{f_0}-E_{i_0})/2]^2}$ becomes highly peaked about $E_{f_0} = E_{i_0}$, with integrated strength $2\pi t$ [63].

2.1.1 Current through the Molecular Wire

An important consequence of the discussion above is that the electron transfer in a (nondriven) molecular wire is *isoenergetic*. An electron with initial energy E_{i_0} can tunnel only into states in the R-reservoir with the same energy (cf. Eq. (2.12)). A second important point is that the states of the metal reservoirs are all occupied below the Fermi level and unoccupied above (at temperature $T = 0$, a condition which we assume applies in the present discussion). When the metal reservoirs are connected by a wire with no applied voltage, the Fermi levels of the L and R-reservoirs are at the same energy. Thus tunneling from any occupied state of the L reservoir is "blocked", because all isoenergetic states of the R-reservoir are occupied.

The situation changes when a voltage is applied across the metal contacts (reservoirs). This causes the Fermi level of the L-reservoir to be above that of the R-reservoir (by the amount of the applied voltage V_{ap}). Now the electrons in the L-reservoir with energy above the Fermi level of the right level can tunnel isoenergetically to the R-reservoir. We want to calculate the total rate of electron transfer (current) for a given applied voltage V_{ap}.

The overall probability to make a transition to the R-reservoir is obtained by summing $|c_{f_0}(t)|^2$ over final states f_0. This probability is finite and proportional to t, thus establishing a well-defined transition rate r_{i_0}:

$$r_{i_0} \equiv \frac{1}{t}\sum_{f_0} |c_{f_0}(t)|^2 = 2\vec{v}^{\,L} \cdot \mathbf{g}(E_{i_0})\mathbf{\Delta}^R(E_{i_0})\mathbf{g}^{\dagger}(E_{i_0}) \cdot \vec{v}^{\,L} \tag{2.13}$$

with $\mathbf{\Delta}^R$ an $N \times N$ "spectral density" matrix given by:

$$[\mathbf{\Delta}^R(E)]_{I,I'} = \pi \sum_f V_{f,I} V_{f,I'} \delta(E - E_f) \tag{2.14}$$

Again, assuming that the temperature is sufficiently low that the $T = 0$ limit of the Fermi distribution can be invoked, the total current I is given as the sum of contributions from all incident electronic states in the range $E_F^R < E_{i_0} < E_F^L$:

$$I = \frac{2}{\pi} \int_{E_F^R}^{E_F^L} dE \, tr\{\mathbf{\Delta}^L(E)\mathbf{g}(E)\mathbf{\Delta}^R(E)\mathbf{g}^\dagger(E)\} \tag{2.15}$$

with:

$$[\mathbf{\Delta}^L(E)]_{I,I'} = \pi \sum_i V_{i,I} V_{i,I'} \delta(E - E_i) \tag{2.16}$$

2.2 TIGHT-BINDING MODEL OF LASER-DRIVEN MOLECULAR WIRE

Suppose that a monochromatic electric field of frequency ω and amplitude E_0 is applied along the axis of the bridge molecule. Because the wavelength of light (typically in the near-IR or visible region for the problem of interest here; see below) is much longer than the dimensions of the molecular wire, we would naturally expect it to be constant at a given time over the entire spatial extent of the molecule, if the latter was "free-standing" (not attached to electrodes).

This expectation is clouded by the presence of the two metal contacts, which are also illuminated by the light. In the present work, we assume the metal contacts are perfect conductors, so that the electric field inside them is identically zero [64]. We further assume that the electric field imposed by radiation from the light source is not strongly disturbed in the region where the molecular wire is situated, and hence can be considered constant and equal to its free-space value here. With these assumptions, the Hamiltonian of the system is modified to $\hat{H} \to \hat{H} - e_0 \phi^l \cos(\omega t)$, where ϕ^l is the spatially dependent electric potential established by the

light source. ϕ^l is taken to be zero in the Left reservoir, vary linearly across the junction region (where the molecule sits), and be constant inside the Right reservoir. Furthermore, its slope in the junction region is given by $-d\phi^l/dx = E_0$, with x the direction perpendicular to the electrodes (again, we assume the electric field radiated by the light source is polarized in this direction -- basically, along the molecular wire).

Thus, in the junction region, the spatial dependence of the radiated electric field takes the form $-e_0\phi^l = \mu E_0$, where μ is the x component of the (negative of the) electric dipole operator: $\mu \equiv e_0 x$. We assume further that the electric dipole operator is diagonal in the basis of atomic orbitals ("site-orbitals"), due to the small spatial overlap between different orbitals (this overlap falls off exponentially with inter-orbital separation). Moreover, the diagonal dipole matrix elements are assumed to be given to a good approximation by the position of the site orbital (with all zeroth order states in the L-reservoir characterized by the same position, and likewise for the R-reservoir). That is, $\langle I|\mu|I\rangle = \mu_I = e_0 x_I$, where x_I is the position of the I'th atomic site orbital of the bridge molecule. Finally, since the electric potential is assumed to be constant in both reservoirs, we assume that ϕ^l is diagonal in the reservoir states, and has the same value in all L-reservoir states, namely $\mu_L = e_0 x_L = 0$ (taking the position of the surface of the left electrode to be at $x = 0$). Consequently, in the R-reservoir, the diagonal element of ϕ^l implies a value $\mu_R = e_0 x_R$, where x_R is the position of the surface of the metal contact corresponding to the R-reservoir.

We note that to the extent that the dipole moment operator is not diagonal in the original site basis $|I\rangle$, one can perform an orthogonal linear transformation which renders it so. This does not compromise the essential structure of the tight-binding Hamiltonian under consideration here. Further details of this procedure will be given in chapter 3. In the present discussion, we shall assume that $\hat{\mu}$ is "naturally diagonal" in the molecular bridge site basis adopted in order to specify our Hamiltonian operator.

The tight-binding Hamiltonian for a general field-driven molecular wire then reads:

$$\hat{H}(t) = \sum_i (E_i + \mu_L E_0 cos(\omega t)) |i\rangle\langle i| +$$
$$\hat{H}^M(t) + \sum_f (E_f + \mu_R E_0 cos(\omega t)) |f\rangle\langle f| + \qquad (2.17)$$
$$\sum_I \sum_i V_{i,I} (|i\rangle\langle I| + |I\rangle\langle i|) + \sum_I \sum_f V_{f,I} (|f\rangle\langle I| + |I\rangle\langle f|)$$

with the (driven) bridge Hamiltonian:

$$\hat{H}^M(t) = \sum_I (E_I + \mu_I E_0 \cos(\omega t)) |I\rangle\langle I| + \sum_{I \neq J} V_{I,J} |I\rangle\langle J| \qquad (2.18)$$

As in the non-driven case, associated with this Hamiltonian is a state vector of the form indicated in Eq. (2.4), and the time-dependent Schrödinger Eq. (SE), $i|\dot{\psi}(t)> = \hat{H}(t)|\psi(t)>$, is converted into a set of first order ODE's of the form $i\dot{c}_\alpha(t) = \sum_\beta H_{\alpha,\beta}(t) c_\beta(t)$ with $\alpha, \beta = i, I, f$. Furthermore, the basic dynamical problem is the same as in the zero-field case: calculate the time-evolution of a system (electron) is prepared at $t = 0$ in a single state i_0 of the L-reservoir.

The field-off limit of this system, $E_0 = 0$, has been extensively and profitably analyzed using Green's function methods (described above). For the field-driven case, it is less obvious how to apply Green's function (GF) techniques, since these require a time-independent Hamiltonian. However, using Floquet theory ([51-52]), the periodically time-driven Hamiltonian of interest here can be mapped to a (modified and augmented) time-independent form with the same essential structure as in the field-free case. Thus, the GF method can still be applied, and ultimately used to calculate current flow through the wire.

2.3 FLOQUET MAPPING OF FIELD-DRIVEN MOLECULAR WIRE TO AN EQUIVALENT FIELD-OFF MOLECULAR WIRE

To exploit Floquet theory in our analysis of the field-driven wire, it is useful to transform to an interaction picture (IP) with respect to the time-dependent driving terms. That is, we introduce

the IP coefficients $b_\alpha(t)$ [i.e., $c_I(t) = \exp[-i\mu_I E_0 \sin(\omega t)/\omega] b_I(t)$, etc.]. This removes the driving terms from the diagonal elements of the Hamiltonian and puts them into the off-diagonal ones. Specifically,

$$\begin{aligned}\hat{H}_I(t) = &\sum_i E_i |i\rangle\langle i| + \hat{H}_I^M(t) + \sum_f E_f |f\rangle\langle f| + \\ &\sum_I \sum_i V_{i,I} (|i\rangle\langle I| e^{-ia_{IL}\sin(\omega t)} + |I\rangle\langle i| e^{-ia_{LI}\sin(\omega t)}) + \\ &\sum_I \sum_f V_{f,I} (|f\rangle\langle I| e^{-ia_{IR}\sin(\omega t)} + |I\rangle\langle f| e^{-ia_{RI}\sin(\omega t)})\end{aligned} \tag{2.19}$$

with the IP bridge Hamiltonian:

$$\hat{H}_I^M(t) = \sum_I E_I |I\rangle\langle I| + \sum_{I \neq J} V_{I,J} |I\rangle\langle J| e^{-ia_{JI}\sin(\omega t)} \tag{2.20}$$

In these expressions, the dimensionless field amplitudes $a_{\alpha\beta}$ ($\alpha, \beta = i, I, f$), are given by:

$$a_{\alpha\beta} = E_0(\mu_\alpha - \mu_\beta)/\omega = -a_{\beta\alpha} \tag{2.21}$$

with all $\mu_i = \mu_L$, and all $\mu_f = \mu_R$ [65]. The IP Schrödinger then reads:

$$i\dot{b}_\alpha(t) = \sum_\beta (H_I)_{\alpha,\beta}(t) b_\beta(t); \qquad \alpha, \beta = i, I, f \tag{2.22}$$

Following the procedure prescribed by Floquet theory, the IP Schrödinger coefficients are expanded in a Fourier series based on the periodicity of the driving force. That is,

$$b_\alpha(t) = \sum_{m=-\infty}^{\infty} b_{\alpha,m}(t) e^{im\omega t}; \qquad \alpha = i, I, f \tag{2.23}$$

The auxiliary Floquet coefficients $b_{\alpha,m}$ remain to be determined. This is done by substituting Eq. (2.23) into the IP Schrödinger Eq. simultaneously with the following Fourier expansion of the driving terms appearing there:

$$e^{ia\sin\omega t} = \sum_{m=-\infty}^{\infty} J_m(a) e^{im\omega t} , \tag{2.24}$$

where J_m is the Bessel function of order m. Identifying the net coefficient of each $\exp(im\omega t)$ term generates a set of coupled linear 1st order ODE's for the Floquet coefficients $b_{\alpha,m}$. In fact, these ODE's have the form of a Schrödinger Eq. characterized by a time- *in*dependent Hamiltonian which nevertheless bears an intimate resemblance to the physical Hamiltonian. The Floquet Hamiltonian $\mathbf{H}^F$ is associated with an augmented state space. For each physical state $b_\alpha(t)$ in the physical system, there is a discrete manifold of states $b_{\alpha,m}(t)$ in the Floquet system. In other words, in the equivalent Floquet system, there are replicas of the physical states shifted by all integer multiples of the photon quantum. These Floquet states are thus naturally labelled by *two* indices (α, m), where, again, $\alpha = i, I, f$ describes the physical state which is replicated and $m = \ldots -1, 0, 1 \ldots$ labels the replica number. The energy of Floquet state (α, m) (referred to as a "quasienergy", in order to distinguish it from the site energies of the various physical states) is

$$E_{\alpha,m} = E_\alpha + m\omega , \tag{2.25}$$

Off-diagonal matrix elements in the Floquet Hamiltonian include: coupling of L-reservoir Floquet states to bridge Floquet states:

$$H^F_{(i,k_L),(I,k_B)} = V_{i,I} J_{k_L - k_B}(a_{LI}) ; \tag{2.26}$$

coupling of Floquet bridge states to other Floquet bridge states:

$$H^F_{(I,k_B),(I',k'_B)} = V_{I,I'} J_{k_B - k'_B}(a_{II'}) ; \tag{2.27}$$

and, finally, coupling of Floquet bridge states to R-reservoir Floquet states:

$$H^{F}_{(f,k_R),(I,k_B)} = V_{f,I} J_{k_R - k_B}(a_{RI}) \tag{2.28}$$

It is useful to construct a state/coupling diagram for the effective field-off system generated by Floquet analysis, as is done in Fig. 2.2. This diagram shows clearly that the Floquet Hamiltonian relevant to the driven system has the same generic structure as that of a *non*driven molecular wire: both the bridge and the reservoirs are expanded (augmented) in a straightforward manner, and the various couplings coefficients are modified, too.

To represent the physical initial condition $b_{i_0}(0) = 1$ (all other coefficients equal 0), we will choose $b_{i_0,k_L=0}(0) = 1$ (all other Floquet coefficients equal 0).

From Fig. 2.2 and the details presented in the preceding paragraphs, it follows immediately that the Green's function analysis utilized in the case of the non-driven molecular wire can be applied to the Floquet Hamiltonian for the *ac* field-driven wire.

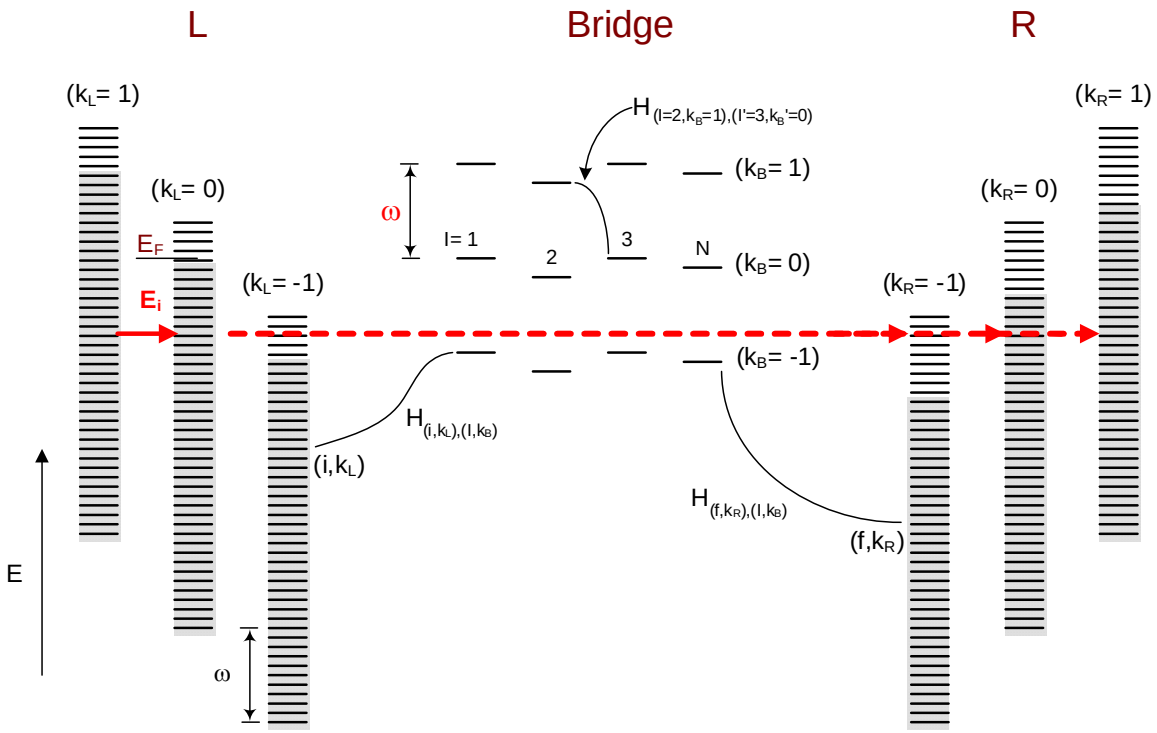

Figure 2-2. Floquet state diagram for driven molecular wire system. (Site energies of the physical bridge molecule and metal states are labeled by $k_L = 0$, $k_B = 0$, $k_R = 0$).

One important aspect of the connection between the quantum dynamics obtained from the Floquet Hamiltonian and that of the corresponding physical system should be emphasized. As stressed at the outset, for a time-independent Hamiltonian of the type under consideration here, i.e. having the essential structure of Eq. (2.2), the principle of energy conservation holds: after short time transients, the molecule can only tunnel *isoenergetically*, i.e. such that the (quasi)energy of the final state in the R-reservoir is equal to that of the initially populated Floquet state in the L-reservoir. Relating this property to the dynamics of the underlying physical, time-driven system is aided by the following observations.

When one computes (e.g., numerically), dynamics under the time-driven Hamiltonian system prescribed by Eq. (2.17), it is found that an electron starting from energy level E_{i_0} can end up in the final state $E_{f_0} = E_{i_0} + n\omega$, where n is an integer (positive, negative or zero), corresponding to net absorption of n photons (with negative values of n corresponding to emission).

To connect the behavior of the time-independent Floquet Hamiltonian to that of the underlying time-driven system, one simply has to recognize that different isoenergetic transitions in the Floquet dynamics correspond to photon absorption/emission in the physical system (i.e., have physical final state energies that are shifted from E_{i_0} by integral multiples of the photon quantum). Transitions to the $k_R = 0$ R-reservoir replica correspond to net zero photon absorption, transitions to $k_R = 1$ correspond to net 1-photon emission, etc., or, equivalently, a transition from an L-reservoir state with energy E_{i_0} to an R-reservoir state with energy $E_{i_0} + n\omega$ corresponds in the Floquet picture to an isoenergetic transition (at energy E_{i_0}) from L-reservoir replica $k_L = 0$ to R-reservoir replica $k_R = -n$. In this way the currents associated with electrons arriving at the various allowed final state energies in the field-driven system can be quantitatively accounted for via Floquet analysis.

Finally, we discuss the issue of how to truncate the formally infinite manifold of Floquet states. Fortunately, the principle of "state mixing", i.e., that two zeroth order states couple more strongly if they are nearly degenerate than if they are not, assures that only Floquet replicas which are nearly iso-energetic with E_{i_0} need be retained. In practice we keep the few "most nearly degenerate" Floquet reservoir and bridge replicas and ignore the rest. The number of replicas is expanded until numerical convergence is attained. Typically, the number of replicas which must be retained is modest -- examples are given in Sect. 2.5.

2.4 AN "INDEPENDENT CHANNEL APPROXIMATION" TO FIELD-DRIVEN TRANSPORT

The mapping of the Floquet Hamiltonian given in Sect. 2.3 to a time- *in*dependent Hamiltonian with the same form as the canonical tight-binding molecular wire Hamiltonian is precise, and thus leads to a precise way to calculate current flow through a laser-driven molecular wire. As described there, the effective Hamiltonian generated by the Floquet mapping has an augmented bridge comprising $N_b N$ sites, where N is the number of sites in the physical bridge molecule

and N_b is the number of Floquet bridge replicas retained in the calculation. Associated with this augmented bridge is a Floquet bridge Hamiltonian and a Floquet self-energy matrix (the latter being a function of the parameter E). The linear dimension of both matrices is $N_b N$, where the value of N_b is formally infinity, though in practice convergence can be obtained with a finite and often modest value (corresponding to N_b replicas), as noted above. Nevertheless, as the calculation gets more complicated, physical insight can become obscured.

Some insight can be restored by considering an approximation in which off-diagonal terms coupling different Floquet replicas in the $N_b N$ augmented bridge Hamiltonian and self-energy are neglected. This renders both matrices block diagonal with an $N \times N$ block representing each Floquet replica. Consequently, the Green's function attains the same block diagonal structure.

We denote the self-energy modified bridge Green's function associated with the Floquet Hamiltonian as $\mathbf{g}^F(E)$. It has the structure indicated in Eq. (2.7), bearing in mind that the appropriate bridge Hamiltonian is the augmented (multi-replica) version depicted schematically in Fig. 2.2: thus $\mathbf{g}^F$ is an $N_b N \times N_b N$ matrix. Similarly, the appropriate L- and R-reservoirs which determine the self-energy matrix that enters into $\mathbf{g}^F$ are the multi-replica versions also depicted in Fig. 2.2. (The coupling elements connecting sites of the extended bridge to states of the extended reservoirs are specified in Eqs. (2.26)-(2.28). Formally, an infinite number of reservoir replicas has to be considered, but in practice the number of contributing replicas is modest because $|J_n(a)| \to 0$ as $n \to \infty$ (for fixed a). The elements of $\mathbf{g}^F$ are explicitly prescribed in Appendix A.

In general, the transition probability for an initial state i_0 of the L-reservoir to a final state f_0 of the R-reservoir which is nearly on-resonance with a net N_p-photon emission (corresponding in the Floquet Hamiltonian system to transitions to the R-reservoir replica $k_R = N_p$) is:

$$|b_{f_0}(t)|^2 \cong 2\pi t \delta(E_{f_0} + N_p\omega - E_{i_0}) |\vec{v}^L \cdot \mathbf{g}^F(E_{i_0}) \cdot \vec{v}^R|^2 \qquad (2.29)$$

with the $N_B N$ dimensional array $\vec{v}^L$ consisting of the coupling elements

$V_{i_0,I} J_k(a_{IL})\,;\, I = 1,2,...,N\,, k = 1,2,...,N_B$

Similarly, $\vec{v}^R$ consists of elements $V_{f_0,I} J_{N_p - k}(a_{RI})$.

As noted above, within the ICA the Green's function $\mathbf{g}^F$ becomes block diagonal, each block having the dimension N of the physical molecular bridge. Thus, the ICA implies:

$$\vec{v}^L \cdot \mathbf{g}^F(E_{i_0}) \cdot \vec{v}^R \cong \sum_{k_L=-\infty}^{\infty} \vec{v}^L_{k_L} \cdot \mathbf{g}^{eff}(E_{i_0} - k_L\omega) \cdot \vec{v}^R_{N_p - k_L} \tag{2.30}$$

The matrix $\mathbf{g}^{eff}$ on the r.h.s. of this expression is an effective molecular Green's function. It has the dimensions of the physical bridge, i.e. $N \times N$, and also the same generic structure as in the field-off case, namely:

$$\mathbf{g}^{eff}(E) = (\mathbf{H}^M_{eff} - \mathbf{\Sigma}^{eff}(E) - E)^{-1} \tag{2.31}$$

In this expression, $\mathbf{H}^M_{eff}$ is an effective molecular bridge Hamiltonian matrix, dimension $N \times N$. Its diagonal elements are the bridge site-energies E_I and its off-diagonal elements are renormalized bridge coupling parameters $V_{II'} J_0(a_{II'})$. The corresponding effective $N \times N$ effective self-energy matrix $\mathbf{\Sigma}^{eff} = \mathbf{\Sigma}^{L,eff} + \mathbf{\Sigma}^{R,eff}$ is defined as:

$$\Sigma^{L,eff}_{I,J}(E) = \sum_{m=-\infty}^{\infty} J_m(a_{LI}) J_m(a_{LJ}) \Sigma^L_{I,J}(E - m\omega)\,, \tag{2.32}$$

$\mathbf{\Sigma}^L$ being the left reservoir spectral density of the physical (field-off) wire, as prescribed in Eq. (2.9); and analogously for $\Sigma^{R,eff}_{I,J}(E)$. Finally, the elements of the N-dimensional vectors $\vec{v}^{L,R}_k$ are given by:

$$(\vec{v}_k^{\,L})_I = V_{i_0,I} J_k(a_{IL}); \qquad (\vec{v}_k^{\,R})_I = V_{f_0,I} J_k(a_{RI})$$

The decomposition provided by the ICA enables more rapid numerical evaluation because of its "divide and conquer" flavor. In particular, the size of the matrices which have to be inverted is dramatically reduced (particularly for large N_b). However, the primary utility of the channel decomposition is that it provides a way to anticipate the origin of large contributions to the current by associating individual contributions to Eq. (2.30) with specific electron transfer pathways or "channels". This interpretation is discussed next, as is the expected regime of validity of the ICA.

2.4.1 Interpretation and Validity Regime of the Independent Channel Picture

Each term on the r.h.s. of Eqs. (2.30) can be described as the probability amplitude for the electron to make a transition from i_0 of the left reservoir to f_0 of the R-reservoir in three steps, namely: (i) emission of k_L photons to access the molecular bridge from the L-reservoir (controlled by the term $\vec{v}_{k_L}^{\,L}$), (ii) isoenergetic tunneling across the bridge, i.e. at energy $E_{i_0} - k_L\omega$ [controlled by the term $\mathbf{g}^{eff}(E_{i_0} - k_L\omega)$], and finally (iii) emission of $N_p - k_L$ photons in the transition from the bridge to the R-reservoir (controlled by the term $\vec{v}^{\,R}_{N_p-k_L}$). Typical channels are depicted schematically in Fig. 2.3. The product of the three factors just delineated determines the amplitude for the process described. Each integer value of k_L defines a distinct channel, and the contribution from all channels must be included in the sum (at the amplitude level).

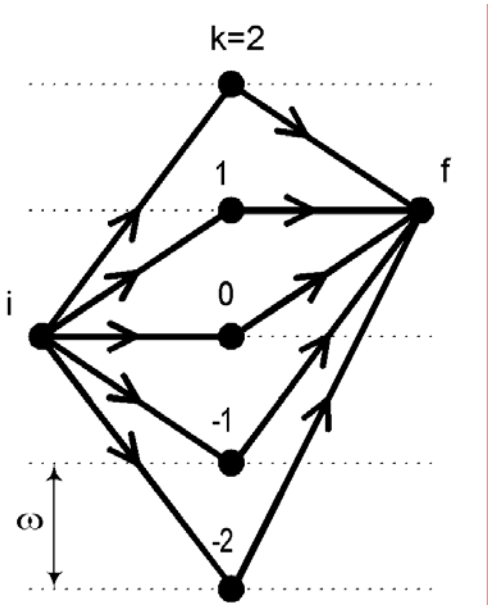

Figure 2-3. Schematic illustration of net 1-photon absorption pathways through a molecular bridge in the Independent Channel Approximation.

The rationale behind this interpretation is straightforward. The term J_k is associated with k-photon emission. Thus the factor $\vec{v}^{L}_{k_L}$ connects the L-reservoir to the bridge (via k_L photon emission) and the factor $\vec{v}^{R}_{N_p-k_L}$ connects the bridge to the R-reservoir (via $N_p - k_L$ photon emission). Note further the properties of the effective molecular bridge Green's function $\mathbf{g}^{eff}(E)$. The site energies of $\mathbf{H}^{M}_{eff}$ are just the site energies of the bridge molecule, while the hopping elements are the physical bridge hopping elements slightly modified by an appropriate factor of J_0. Usually we will have $a_{II'} << 1$ for site orbitals which are connected by large values of $V_{II'}$. Thus, the effective molecular bridge closely resembles the physical bridge, and in particular the molecular orbital energies are close to the physical bridge MO's. Consequently, resonances in $\mathbf{g}^{eff}(E)$ reflect the MO energies of the bridge molecule. In particular, the amplitude (ii) for isoenergetic tunneling through the bridge will be significant when $E_{i_0} - k_L\omega$ is approximately equal to an MO energy of the bridge, that is, when emission of k_L photons brings the energy of the tunneling electron into resonance with one of the MO's of the bridge. This interpretation is particularly easy to appreciate in the special (but conceptually important) case that the L-

reservoir couples only to the orbital $I = 1$ of the bridge (located closest to the left electrode), and the R-reservoir couples only to the orbital $I = N$ (located closest to the right electrode). In this case the ICA transition rate formulae simplify considerably, as discussed in Appendix B.

We should stress that this picture of independent electronic channels or pathways between the Left and Right metallic contacts is an approximate one, being predicated on the neglect of off-diagonal matrix elements in the Floquet Green's function which couple different Floquet bridge replicas. It will be thus be most accurate when electronic coupling matrix elements are small, the laser-field is weak, or there is a large energy gap between the quasi-energies of different bridge replicas arising from a high photon frequency. In the first two circumstances the elements of the inter-replica coupling blocks go to zero, while in the third there is poor "mixing" between the zeroth order states in separate replicas due to the large gaps between their zeroth order (quasi)energies. The best way to ensure that the ICA is valid is to correct it by coupling several bridge replicas together and verifying that the effects of such coupling are small.

Another way to include inter-replica coupling is to carry out the perturbation expansion [62] of the generic form: $G = G_0 - G_0 V G_0 + G_0 V G_0 V G_0 - \ldots$, where G here is the full Floquet Green's function, G_0 is the block diagonal part of this and V is the off-diagonal, inter-replica coupling part of the full Floquet Hamiltonian which is neglected in G_0. For sufficiently small V, this expansion is convergent, and in such cases, it provides insight by enumerating possible pathways for electron transport across the bridge. The G_0 term (ICA approximation) corresponds to photon absorption/emission only between L,R reservoirs and the bridge (no photon absorption/emission as the electron hops between bridge states), while the $G_0 V G_0$ term adds in processes that include one photon absorption/emission within the manifold of bridge states, etc. A full description of this expansion, its range of validity, and insights that can be gleaned from it will be presented elsewhere [66].

As noted above, we have opted in the present work to include inter-replica coupling effects by performing basis set inversion with an expanded number of bridge Floquet replicas. The basis set method, when convergence can be obtained (which we have found to be the case here), avoids any potential errors encountered in truncating the perturbation expansion at some finite and often low order.

2.5 RESULTS FOR A MODEL SYSTEM

In this section we present numerical results for a simple model system. Our goal is to illustrate the features of the underlying quantum dynamics of *ac*-field assisted electron transport in a molecular electron transfer system attached to metallic reservoirs. We do not attempt to extract "realistic" current-voltage characteristics here. This will be done in a chapter 3. Thus, our model consists of a symmetric three-site molecule coupled symmetrically to finite-width Left and Right metallic reservoirs, as sketched in Fig. 2.4. The reservoir states span the energy regime $-1 < E < 1$. All three bridge site energies are taken to have the same value, namely $E_B = 0.8$ -- thus they lie within the reservoir energy band [66]. We assume only nearest neighbor electronic coupling between orbitals in the bridge Hamiltonian. Furthermore, only bridge state 1 interacts with the L-reservoir, and only bridge state 3 interacts with the R-reservoir. The strength of the bridge-electrode interaction and reservoir density of states is prescribed by the Newns-Anderson spectral density:

$$\Delta(E) = \frac{V^2}{\gamma}\sqrt{1-(E/2\gamma)^2}, \quad |E/2\gamma| < 1 \tag{2.33}$$

where $\frac{V^2}{\gamma} = 0.12$ (and $\gamma = 0.5$). We choose driving field parameters such that the reservoir-bridge field parameter $a_{L,R} = 2$ throughout, with the parameters $a_L \equiv a_{1,L}$ and $a_R \equiv a_{R,3}$ (cf. Eq. (2.21) above). For simplicity, and to focus on consequences of the *ac*-driving field, we set the applied *dc* electric field to zero (i.e., no modification of the one-electron orbital site-energies by a static applied voltage).

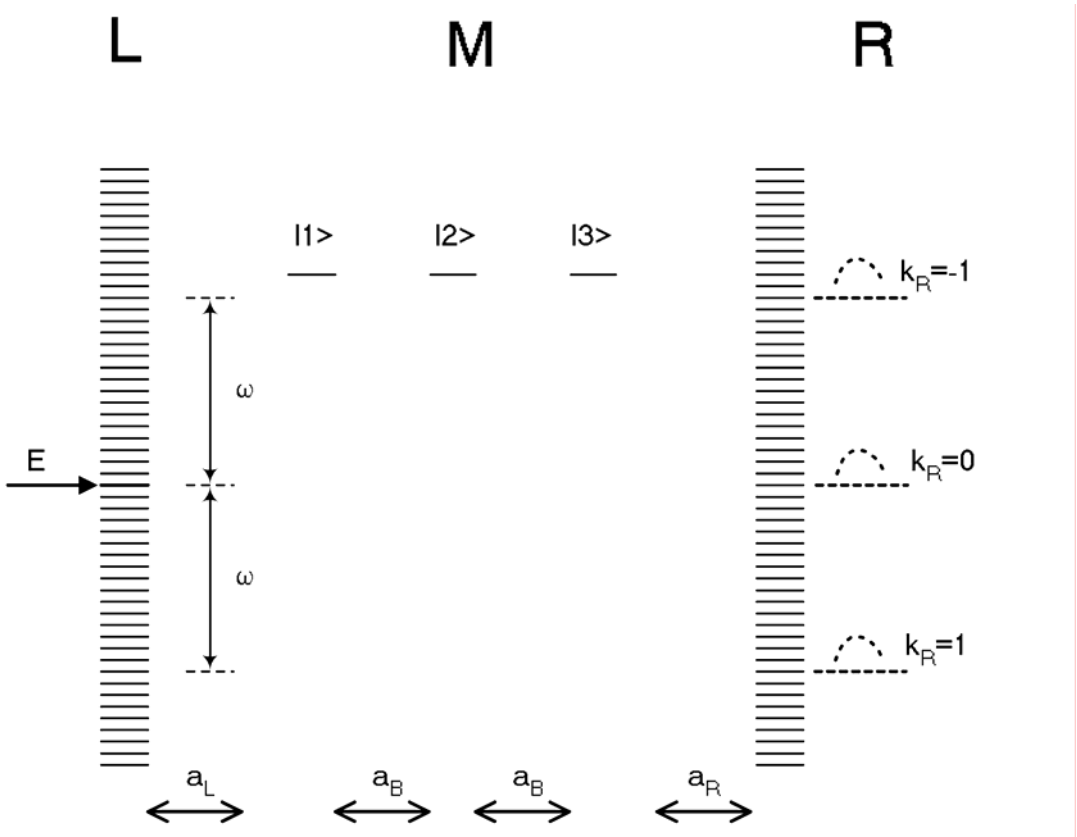

Figure 2-4. Schematic representation of a molecular wire system corresponding to a 3 state molecular bridge. "Blips" associated with $k_R = 0,\pm 1$ depict allowed final state energy regimes for the indicated laser frequency. See text for further details.

In the calculations presented below, we consider the dynamics of an *isolated* electron according to the 1-electron Hamiltonian (2.17). To illustrate how solutions to this time-dependent Schrödinger Eq. can be obtained using the approach developed in the previous sections, we ignore effects due to the presence of other electrons in the reservoirs, including the exclusion of the tunneling electron from any occupied R-reservoir state. Clearly, such effects have to be included in any complete calculation of current through a molecular wire attached to electrodes. We defer this important exercise to chapter 3.

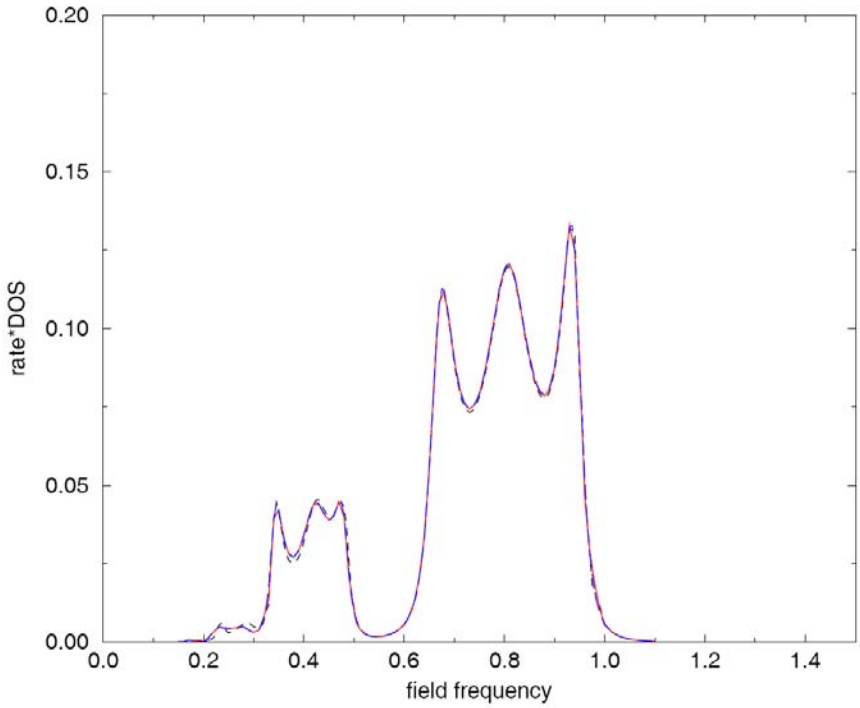

Figure 2-5. Rate of transitions to the R-reservoir of the electron initially prepared in state $E = 0$ of the L-reservoir as a function of the laser field frequency. (In this and subsequent figures, transition rates to the R-reservoir from an incident electron at $E = 0$ of the L-reservoir are scaled by the density of states [DOS] at this energy.) Results obtained from integration of the Schrödinger Eq. for the (physical) time-driven system are shown via the dashed line. Corresponding results obtained by direct integration of (time-independent) Floquet Hamiltonian are shown via the solid curve. Results obtained from the Floquet Green's function analysis presented in text are indistinguishable from the solid curve. The following parameters were utilized: $a_B = 0.1$, $V_B = 0.1$, $a_{L,R} = 2$; $V_{ap} = 0$.

Fig. 2.5 shows the rate of transitions to all states of the R-reservoir for a system prepared initially in an $E = 0$ state of the L-reservoir, for driving-field parameter choices $a_B = 0.2$, where $a_B \equiv a_{2,1} = a_{3,2}$, and intra-bridge coupling $V_B = 0.1$. (Again, we fix the value $a_{L,R} = 2$ in all results presented in this section, and we have set the applied *dc* bias $V_{ap} = 0$.) Three different calculations are displayed. The dashed line shows the result obtained by direct integration of the time-dependent *ac*-field driven Schrödinger Eq. In practice, this was done by representing the Left and Right electronic reservoirs using a finite set of states, evenly spaced in energy, and coupled to the bridge via matrix elements $V_{i,1}$ and $V_{f,N}$ (cf. Eq. (2.2)) selected in accordance

with the spectral densities $\mathbf{\Delta}^{(L,R)}$. (The formal definition of the spectral densities was given in Eq. (2.14), and the specific functional form in Eq. (2.33) above.) Convergence was obtained by increasing the number of discrete states in the reservoirs, while maintaining the desired (finite) spectral density by reducing the individual reservoir-bridge coupling elements accordingly.

The solid line in Fig. 2.5 shows the result of direct numerical integration of the time-independent Floquet Hamiltonian, keeping 6 bridge replicas (specifically, $k_B = -4...1$) and 7 L- and R-reservoir replicas (specifically, $k_{L,R} = -3...3$). [The discretization of the reservoir continua outlined in the previous paragraph was employed here, too.] This result is identically reproduced to within the resolution of the figure by the Green's function formula recorded in Sect. 2.1, as implemented for the Floquet Hamiltonian described in Sect. 2.3, including the same range of reservoir replicas in the calculation of the relevant self-energies (cf. Appendix A). The agreement between direct simulation of the time-driven system and computations based on the Floquet mapping to an effective time-independent system is seen to be quite good. Moreover, the Green's function analysis of the dynamics of the (time-independent) Floquet Hamiltonian system is completely satisfactory. Thus, in the remainder of the numerical studies to be presented in this work we will simply use the Green's function formulae to obtain transition rates from the Left to the Right reservoirs through the molecular bridge.

Before considering other illustrations, it is worthwhile to study the results portrayed in Fig. 2.5 in more detail. In these plots, the transition rate to the R-reservoir is scanned as a function of laser frequency, holding the laser intensity parameters $a_{L,R}$ and a_B fixed [67]. The shape of the spectrum thus generated reflects the details of the molecular bridge Hamiltonian. In particular, as discussed above, the molecular Green's function has *resonances* at the values of the molecular orbital energies. In the present example, the molecular orbital energies of the bridge are far from the incident energy of the electron in the L-reservoir. Thus, in the absence of the applied laser field, the electron transport (tunneling) is extremely weak. However, by absorbing (or in the general case, emitting) an integral number of photons, the energy of the tunneling electron is boosted by the appropriate multiple of the photon quantum. This can bring it into resonance with the molecular orbitals of the bridge Green's function and thus dramatically enhance the Green's function transmission factor. In the system studied in Fig. 2.5, the energy difference between the incident electron and the center of the bridge molecule molecular orbital

energy level distribution is 0.8. Thus, the triplet of peaks at ca. $\omega = 0.8$ is due to 1-photon absorption by the incident electron. The triplet of peaks at ca. $\omega = 0.4$ corresponds to 2-photon absorption resonance, while that at ca. $\omega = 0.27$ corresponds to a 3-photon absorption resonance.

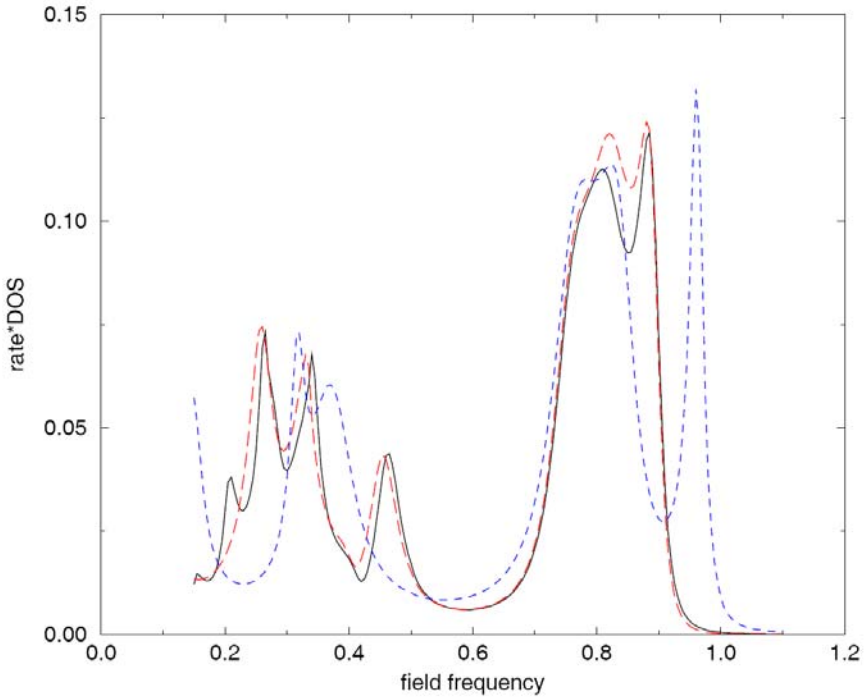

Figure 2-6. Dependence of the current vs frequency curve on the number of Floquet replicas in the Floquet Hamiltonian. Solid line shows results with (10,9) (bridge,reservoir) replicas (see text for full details). Long-dashed line shows corresponding result for (6,7); short-dashed line shows corresponding result for (3,5). The following parameters were utilized: $a_B = 2.0$, $V_B = 0.5$.

The number of Floquet replicas needed to obtain good agreement with the (physical) time-driven system dynamics depends on the intra-bridge field parameter a and coupling matrix elements V_B. In Figure 6 we present calculations in which the relatively large parameters $a_B = 2$ and $V_B = 0.5$ are used. In this case, a larger number of Floquet bridge and reservoir replicas (10 and 9, respectively) are needed to accurately model the field-on curve, specifically $k_B = -6...3$ and $k_{L,R} = -4...4$.

A Green's function calculation utilizing this number of replicas is shown via the solid line. The long-dashed curve shows the results of a Green's function calculation for a Floquet

Hamiltonian with a smaller number of replicas, specifically 6 for the bridge ($k_B = -4...1$) and 7 for the reservoirs ($k_{L,R} = -3...3$). Using an even smaller number of Floquet replicas, namely 3 for the bridge ($k_B = -2...0$) and 5 for the reservoirs ($k_{L,R} = -2...2$) produces an even less accurate result, indicated by the dotted line.

When the applied laser field is weak (hence all a-parameters are small), or the electric coupling matrix elements are small, we can approximately set non-diagonal blocks of the Floquet Hamiltonian to zero, i.e. invoke the Independent Channel Approximation. In the ICA, once an electron "hops" from the L-reservoir to a particular bridge replica, it then hops between states of the same replica until it reaches the R-reservoir. The total rate of electron transfer is the sum (at the amplitude level) of contributions from all such channels.

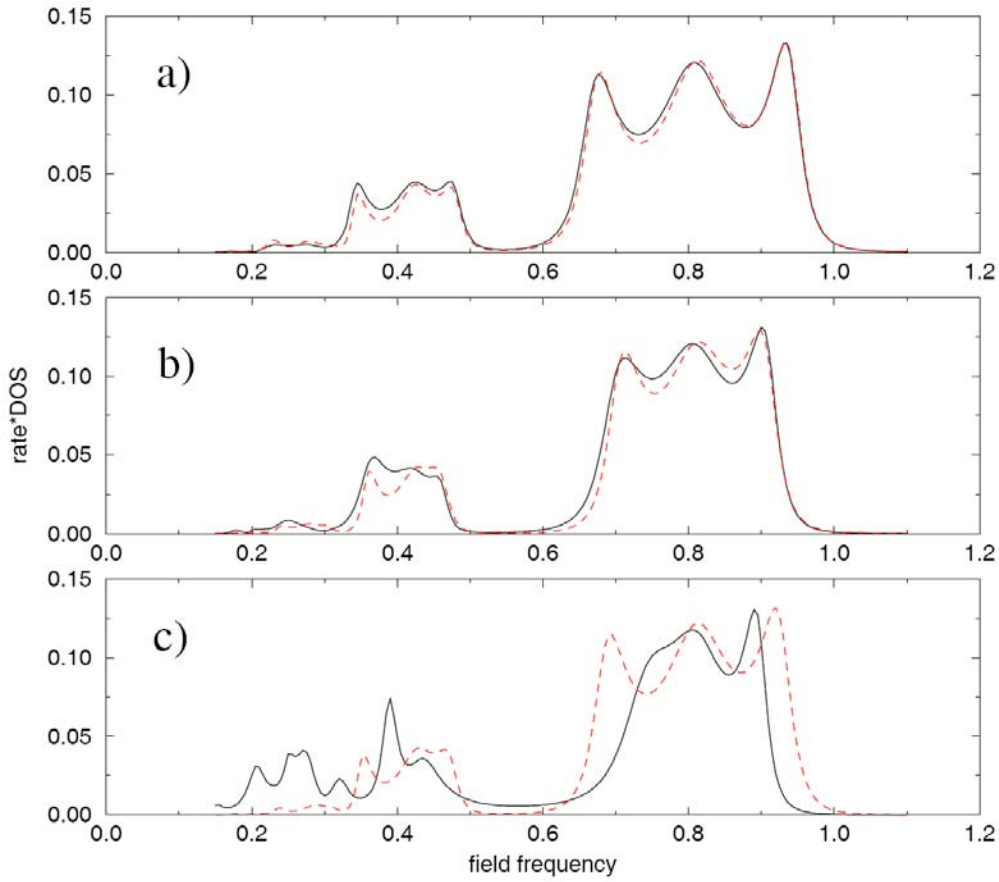

Figure 2-7. Illustration of the range validity of the Independent Channel Approximation (ICA) for different values of intra-bridge field parameter. In each panel, the solid line shows exact result for transition rate to the R-reservoir vs laser frequency; dashed line shows corresponding result within the ICA. Panel (a) $a_B = 0.2$,

$V_B = 0.1$ (weak coupling); panel (b): $a_B = 1.0$, $V_B = 0.15$ (intermediate coupling); panel (c): $a_B = 2.0$, $V_B = 0.5$ (strong coupling).

In Fig. 2.7 we test the accuracy of the ICA by comparing molecular wire systems with different intra-bridge field parameters. The system is the same as that considered in Fig. 2.7 except for the values of a_B and V_B, which are varied as follows. In the top panel, which is characterized by an intra-bridge field parameter $a_B = 0.2$ and intra-bridge coupling $V_B = 0.1$ (both of which are small), the agreement between the exact (solid line) and ICA (dashed line) results is good. The bottom panel shows results for the same system, but with a large intra-bridge field parameter $a_B = 2$ and intra-bridge coupling strength $V_B = 0.5$ -- here the agreement between the exact and approximate curves is poor. The middle panel shows results for an intermediate case, where $a_B = 1$ and $V_B = 0.15$. The results presented in Fig. 2.7 demonstrate that under appropriate conditions (*vide supra*) the ICA is valid and useful.

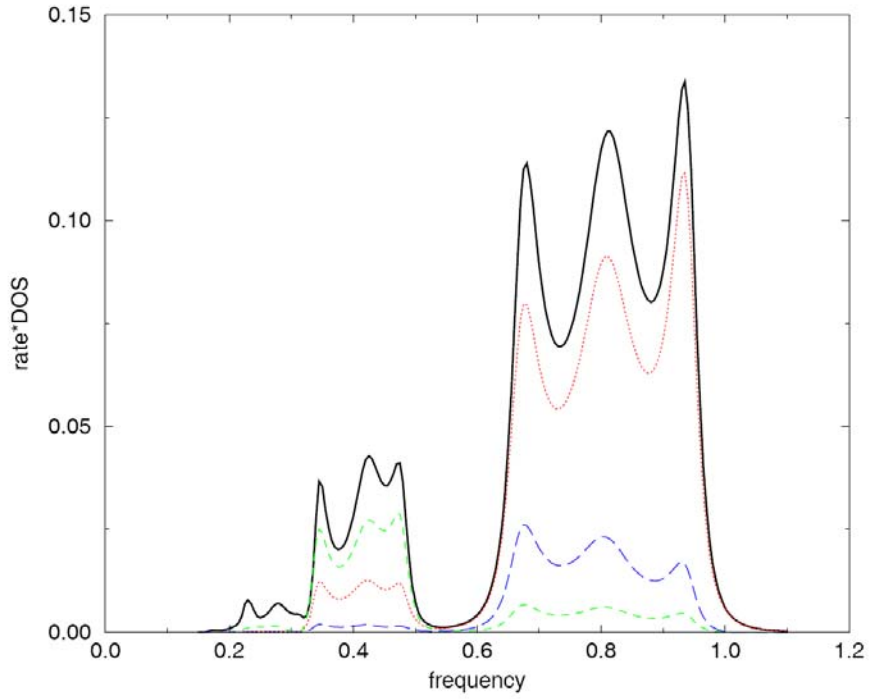

Figure 2-8. Contribution of $0,\pm1$ net photon absorption processes to overall rate of transitions to R-reservoir. Dotted line corresponds to $N_p = 0$, long-dashed line to $N_p = 1$ and short-dashed line to $N_p = -1$. The total transition rate (obtained by summing over contributions from all open channels) is indicated by the solid line. System parameters are the same as considered in Fig. 2.5.

In Fig. 2.8, for the same molecular wire system considered in Fig. 2.5, we decompose the total current to the right electrode (thick solid line) into contributions to various Right reservoir Floquet replicas. The dotted line represents the current to the right electrode replica $k_R = 0$, i.e. direct tunneling in the physical system with no net absorption/emission of photons. The long dashed line is the current to the replica $k_R = 1$ (corresponding to accumulation of electrons at an energy one photon below the tunneling electron energy; cf. Fig. 2.4), and the dashed line is the current to the replica $k_R = -1$ (corresponding to electron accumulation at an energy one photon above the tunneling electron energy). Note that the relative weights of the contributions of the $N_p = \pm 1, 0$ channels change for the 1 vs 2 photon absorption resonance portions of the spectrum. These weights are readily explained by the exposition contained in Appendix B. For the one-photon absorption resonance region near $\omega = 0.8$, the dominant term in the ICA rate formula is $k_l = -1$. Thus, since Δ_R is a weakly varying function of energy within the region $-1 < E < 1$, the relative intensities of the $N_p = 1, 0, -1$ peaks is approximately $J_2^2(2)$, $J_1^2(2)$, $J_0^2(2)$, respectively. On the other hand, for the two-photon absorption portion resonance part of the spectrum, in the region $\omega = 0.4$, the ratio of these peaks is approximately given by $J_3^2(2)$, $J_2^2(2)$, $J_1^2(2)$.

In the case of the 1-photon absorption resonance at $\omega = 0.8$, the $k_R = 0, \pm 1$ channels are the only ones possible. (Other values of k_R correspond to final state energies outside the energetic width of the R-reservoir.) Thus, in this portion of the spectrum the sum of the intensities for $k_R = 0, \pm 1$ processes adds up to the total intensity (solid line). For two and higher photon absorption resonances, there are other (undisplayed) open final state channels besides $k_R = 0, \pm 1$. Thus, the $k_R = 0, \pm 1$ intensities shown in Fig. 2.8 do *not* sum to the total intensity in these parts of the spectrum.

2.6 DISCUSSION AND CONCLUSIONS

In this chapter we have considered the effect of monochromatic light on transport of electrons through molecular wires. As has been done before in the field-off limit [18-21], we adopted a tight-binding model of the electron transport, neglecting complications due to disorder, dissipation, electron correlation, etc. Of course these complications should be incorporated as the theory is developed further, but again, following the success of non-dissipative tight binding models in describing I-V curves for "standard" (i.e., not light-driven) molecular wires, we expect that the same level of description will be useful in the field-driven case.

In the absence of external *ac* driving, the current-voltage characteristics of non-dissipative tight binding models of electron transport through molecular wires can be profitably analyzed via a Green's function scattering approach [18-21]. We have shown in this work, using Floquet theory, that in the case of the *ac* driven analog (generated experimentally by illuminating the wire/electrode system with a monochromatic laser), the relevant time-dependent Hamiltonian can be mapped to a time- *in*dependent Hamiltonian in an extended state space and with modified interstate couplings. The modified/augmented Floquet Hamiltonian has the same essential structure as its field-off analog, and so the Green's function analysis can be directly employed to analyze the quantum dynamics of the Floquet system. This dynamics can then be converted to dynamics of the physical (time-driven) system.

Our Floquet analysis is formally exact, and in practice can be numerically converged with a relatively modest amount of effort. We also presented an approximate analysis, premised on certain weak-coupling assumptions which are clearly set forth above. In this approximation, the numerical effort is further reduced, and, more importantly, insight is provided into the "channels" of multiphoton absorption/emission which contribute strongly to current flow through a wire with particular molecular characteristics under given experimental conditions (applied *dc* voltage, amplitude and frequency of the light source, etc.). We stress that this channel picture should be used as a guide, but when in doubt the full Floquet treatment should be carried out to numerical convergence.

Some prototypical illustrations of the theory and methodology were provided in the present work. We stopped short of calculating I-V curves for a "real" molecular wire (treated at the non-dissipative tight binding level). Such an analysis requires considerable effort, including

careful examination of the molecular electronic structure of the molecular bridge, the metal electrodes and the coupling between them. This will be described in a chapter 3. The goal of such a calculation, from the point of view of outlining a design principle for significantly enhancing (and ultimately, controlling) electron transport through molecular wires, is to demonstrate how the laser illumination with a *cw* light source of an appropriate frequency can convert non-resonant tunneling processes into resonant ones (by absorption or emission of photons to "boost" the tunneling electron to an energy where there are molecular orbital energies to assist tunneling through the bridge), thus dramatically enhancing the electron tunneling rate. Clearly, the smaller the laser power needed to do this, the more robust the control scheme will be. These important issues will also be addressed in chapter 3.

ACKNOWLEDGEMENT

We thank Prof. A. Nitzan for several helpful conversations concerning this work.

APPENDIX A

ELEMENTS OF THE FLOQUET GREEN'S FUNCTION MATRIX

Even after "integrating out" the reservoir states, the dimension of the Floquet Green's function matrix $\mathbf{g}^F(E)$ is formally infinite, since the number of bridge replicas is infinite. If N_b bridge

replicas are retained explicitly, this matrix has finite linear dimension $N_b N$. Its elements are given by inverting the appropriate $N_b N$ dimensional matrix:

$$\mathbf{g}^F(E) = \left[\mathbf{H}_M^F - \overline{\mathbf{\Sigma}} - E\right]^{-1} \tag{2.34}$$

where $\mathbf{H}_M^F$ is an $N_b N$ dimensional matrix whose elements are prescribed by Eqs. (2.25–2.28) in the text. Furthermore, the $N_b N$ dimensional Floquet self-energy matrix $\overline{\Sigma}$ is the sum of contributions from L and R electrodes:

$$\overline{\Sigma}(E) = \overline{\Sigma}^L(E) + \overline{\Sigma}^R(E)$$

where

$$\overline{\Sigma}^L_{(I,k_B),(J,k_{B'})}(E) = \sum_{k_L=-\infty}^{\infty} J_{k_L-k_B}(a_{LI}) J_{k_L-k_{B'}}(a_{LJ}) \Sigma^L_{I,J}(E - k_L\omega)$$

with $\mathbf{\Sigma}^L$ being the (laser-field off) molecular L-reservoir self-energy; $\overline{\Sigma}^R$ is defined analogously.

It is instructive to comment on the sources of coupling that link the $N \times N$ blocks of the inverse Floquet Green's function matrix. First (type i), there are off-diagonal elements of $\mathbf{H}_M^F$, namely $V_{I,I'} J_{k_B - k'_B}(a_{II'})$ with $k_B \neq k_{B'}$. Such terms can only couple different bridge base states (since $V_{I,I} = 0$). Inter-channel coupling (type ii) is also provided by self-energy matrix elements, noted above, with $k_B \neq k_{B'}$. Coupling between the same bridge basis state in different Floquet replicas is accomplished by these terms. Note that both types of coupling vanish as the laser intensity tends to zero. Also, small intra-bridge elements $V_{I,I'}$ and small reservoir-bridge coupling elements $V_{i,I}$, $V_{f,I}$ suppress type i and ii coupling, respectively. Finally, all other terms being equal, increasing the laser frequency ω (with a concomitant increase in the laser amplitude to keep all a parameters constant) also suppresses inter-channel coupling, since the

diagonal matrix elements of different $N \times N$ diagonal blocks of that comprise each channel in $\mathbf{H}_M^F$ are separated by multiples of the laser quantum.

APPENDIX B

PHOTON EMISSION RATES FOR THE CASE OF MINIMAL RESERVOIR–BRIDGE COUPLING

When only bridge orbital 1 couples to the L-reservoir and only bridge orbital N couples to the R-reservoir, the ICA transition probability formulae simplify considerably. In this case we can employ simplified notation: $V_{i_0} = V_{i_0,1}$, $V_{f_0} = V_{f_0,N}$, $a_L = a_{1,L}$, $a_R = a_{R,N}$. Then, for net N_p photon emission:

$$|b_{f_0}(t)|^2 \cong 2\pi t \delta(E_{f_0} + N_p\omega - E_{i_0}) V_{i_0}^2 V_{f_0}^2 \left| \sum_{k_L=-\infty}^{\infty} J_{k_L}(a_L) g_{1N}^{eff}(E_{i_0} - k_L\omega) J_{N_p - k_L}(a_R) \right|^2 \qquad (2.35)$$

Then the rate of N_p photon emission $R_{i_0} \equiv \frac{1}{t}\sum_{f_0}' |b_{f_0}(t)|^2$, with the prime on the sum indicating restriction to the local energy region near $E_{f_0} = E_{i_0} - N_p\omega$, is:

$$R_{i_0} = 2V_{i_0}^2 \Delta_R(E_{i_0} - N_p\omega) \left| \sum_{k_L=-\infty}^{\infty} J_{k_L}(a_L) g_{1N}^{eff}(E_{i_0} - k_L\omega) J_{N_p - k_L}(a_R) \right|^2 \qquad (2.36)$$

A particularly important situation is when the laser is tuned into $-k_l$ photon absorption resonance with the molecular orbital energies of the bridge. In this case the $k_L = k_l$ term dominates in the above sums, and we can approximate:

$$R_{i_0} \cong 2V_{i_0}^2 \Delta_R (E_{i_0} - N_p \omega) J_{k_l}^2 (a_L) \left| g_{1N}^{eff} (E_{i_0} - k_l \omega) \right|^2 J_{N_p - k_l}^2 (a_R) \tag{2.37}$$

Of course, the validity of this formula requires a laser intensity such that the $-k_l$ absorption process has significant amplitude, i.e., $J_{k_l}^2 (a_L) \neq 0$.

Chapter 3. Calculating Electron Current in a Tight-Binding Model of a Field-Driven Molecular Wire: Application to Xylyl-Dithiol

We apply Floquet theory-based formalism for computing electron transport through a molecular bridge coupled to two metal electrodes in the presence of a monochromatic radiation field is applied to an experimentally relevant system, namely a xylyl-dithiol molecule in contact at either end with gold electrodes. In this treatment, a non-dissipative tight-binding model is assumed to describe the coherent electric transport, calculated using Landauer formalism. Net current through the wire is calculated for two configurations of the electrode-wire-electrode system. In one, symmetric, configuration, the electrodes are close (ca. 2 Å) and equidistant from the bridge molecule. In the other, asymmetric configuration, one electrode is farther away (ca. 5 Å), representing an STM tip at this distance from the bridge molecule (the other end being chemisorbed to a gold substrate). For both configurations, electron current is calculated for a range of experimental inputs, including bias and the intensity and frequency of the laser. Via absorption/emission of photons, resonant conditions may be achieved under which electron transport is significantly enhanced compared to the unilluminated analog. Calculations show that this can be accomplished with experimentally accessible laser field strengths.

3.1 PARAMETRIZATION OF THE MODEL

In order for our estimations of laser-induced modifications of electron tunneling through a molecular wire to have at least qualitative value, it is necessary to select a bridge molecule and

metal electrodes, and to establish reasonable electronic structure parameters for the one-electron tight-binding model introduced above. For this reason, we consider for concreteness the xylyl-dithiol molecule as our "wire", and gold electrodes (cf. Fig. 3.1). Xylyl-dithiol is among the simplest systems which has been studied in the context of molecular wires. Its electronic structure has been characterized, at least at the extended Hückel level of electronic structure theory, and it has been shown that this admittedly crude level of treatment produces reasonable agreement with measured current-voltage curves, in the absence of laser-induced perturbations [7]. (To our knowledge, a systematic experimental study of laser illumination on molecule wire performance has not yet been carried out.)

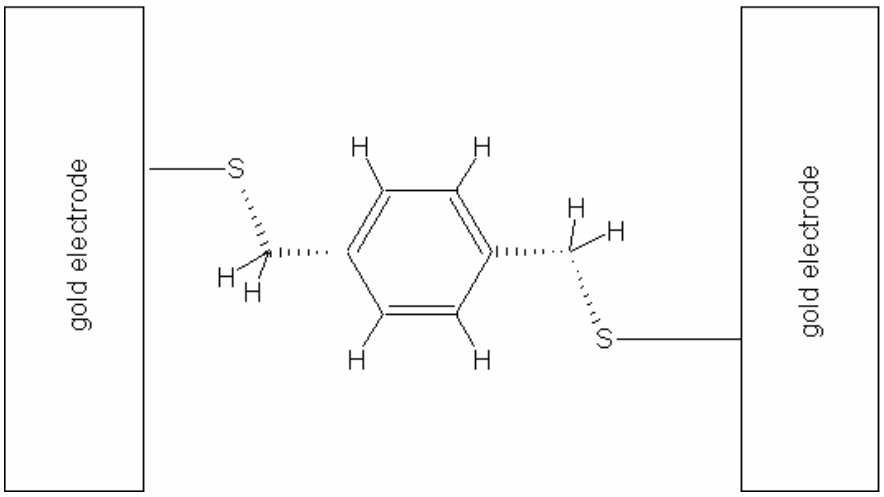

Figure 3-1. Chemical structure of xylyl-dithiol molecule connecting two gold electrodes.

In the next subsection, we discuss how to determine the parameters in the bridge molecule Tight-Binding Hamiltonian. Then we discuss, in turn, how to estimate the electronic coupling between bridge molecule and reservoir, and how to compute the matrix elements of the electric dipole operator (needed to include coupling to a static or an *ac* electric field).

3.1.1 Site-basis Representation of the Bridge Molecule

Following the treatment given in Refs. [19-21, 54, 55], we have used Extended Hückel (EH) theory to estimate site energies and coupling matrix elements in the Tight-Binding Hamiltonian for the xylyl-dithiol molecule. The site-orbitals were chosen to be atomic orbitals (AO) (details are provided below). The site energy ε_I associated with a given AO was taken to be the negative of the ionization potential for removing an electron from that orbital. Specific numerical values were taken from Ref. [71]. Intersite coupling elements were determined by invoking the Wolfsberg-Helmholtz approximation [72]:

$$V_{I,J} = \kappa S_{I,J} \frac{E_I + E_J}{2} \tag{3.1}$$

with $S_{I,J}$ the overlap matrix element for basis atomic orbitals I and J, and $\kappa = 1.75$ an empirically determined scale factor.

The xylyl-dithiol molecule has eight hydrogen atoms, eight carbon atoms and two sulfur atoms. In our calculations we included the $1s$ orbital for the hydrogen, $2s2p$ orbitals for carbon, and $3s3p$ orbitals for sulfur, bringing the total number of basis functions to $N = 48$. The geometric structure of the molecule was obtained by geometry optimization of the isolated molecule using GAUSSIAN 94 [73], which was also used to determine the overlap matrix $S_{I,J}$ in the STO-3G basis set.

The Extended Hückel (EH) method is based on rather crude approximations. It was designed to predict the molecular geometry and charge distribution of limited types of molecules, mainly non-polar hydrocarbons [72]. For energy level structure, EH is expected to be only qualitatively correct. For more accurate electron transport calculations one would need a more realistic tight-binding molecular Hamiltonian. A possible step in this direction would be to use a one-electron model with matrix elements deduced from Hartree-Fock theory [74, 75]. Effects resulting from the connection of the molecule to the gold surface should also be taken into the account: this may alter the equilibrium geometric structure of the xylyl-dithiol molecule.

Furthermore, the molecule can acquire additional partial charge which creates an electrostatic potential along the molecule-electrode connection [19-21].

To calculate the current through the wire it is crucial to know the position of the Fermi energy level of the metal with respect to the HOMO-LUMO gap of the bridge molecule. The work function of gold metal is 5.3 eV, hence the Fermi energy is -5.3 eV. Our EH calculations on xylyl-dithiol molecule yield a HOMO energy of -12.3 eV and a LUMO energy of -8.5 eV. As noted above, the Extended Hückel model was not designed to provide accurate absolute orbital energies, so we need to decide how to locate the EH orbital molecular energies relative to the Fermi energy E_F of the gold. Determination of the Fermi energy location should in principle take into account the possibility of charge transfer occurring as a result of attaching the molecule to the electrode. Both experimental and theoretical estimations [7,17] put the Fermi energy of the electrodes somewhere in the HOMO-LUMO gap, close to the middle of the gap. An *ab initio* HF calculation on isolated xylyl-dithiol using GAUSSIAN 94 with a STO-3G basis set gives a HOMO level energy of about -7 eV, which supports the idea of placing the Fermi energy at the center of the gap.

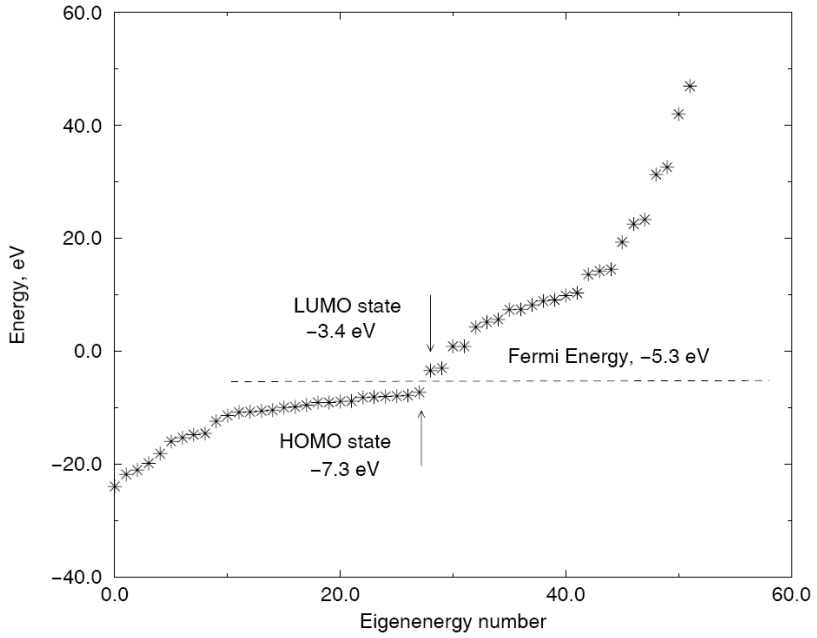

Figure 3-2. Extended Hückel (EH) energies for an isolated xylyl-dithiol molecule, after upward shift of EH levels by 5 eV.

The calculated energy spectrum of the isolated xylyl-dithiol molecule is presented in Fig. 3.2. Because the molecule has 54 valence electrons, HOMO and LUMO states correspond to states 27 and 28, as indicated by the arrow. We shifted the EH energy spectrum up by 5 eV, so that the gold Fermi energy lies midway between the HOMO and LUMO states of the molecule. The new HOMO and LUMO energies are then -7.3 eV and -3.4 eV.

3.1.2 Reservoir-Bridge Coupling Matrix Elements: Spectral Density and Self-Energy Functions

To obtain estimations of the electronic coupling between the electronic states of the metal and those of the molecular wire, we adopt a cluster model for the metal (in our case, gold), and use Extended Hückel theory (*vide supra*). The xylyl-dithiol molecule binds strongly to the gold surface through a thiol group [53]. The sulfur atom can bind to the gold either over a hollow site on the surface between three gold atoms or directly over a gold atom. Although recent experiments and calculations suggest that binding over the hollow site is more energetically favorable [55], in the present work we assume the binding takes place over a single gold atom since this is somewhat simpler to analyze. Given the crude electronic structure model used here, this choice should not qualitatively alter our essential conclusions.

We also describe the electronic structure of the reservoirs and the molecule-reservoir coupling using the Extended Hückel scheme. As noted above, in the model employed here the connection between the molecule and the gold pads occurs through the bond between a single gold (111) atom and the adjacent molecular sulfur atom. For each gold atom we include nine orbitals ($5d6s6p$). The distance between the sulfur atom and the gold atom that it "sits over" is taken to be 1.9 Å (as in [19-21]). The sulfur-gold overlap matrix was obtained using GAUSSIAN 94 with the gold valence basis functions parameters taken from Ref. [76]. Most of the overlap between the sulfur and gold occurs through the s orbital of the sulfur. Thus, we can simplify our calculations by assuming only $V_{i,1} \neq 0$, where 1 corresponds to the 3s orbital of the sulfur atom adjacent to the Left electrode ("L-electrode"), and, analogously, only $V_{f,N} \neq 0$, where N labels the 3s orbital of the sulfur atom adjacent to the Right electrode ("R-electrode").

The gold electrode band structure was obtained from Extended Hückel calculations for a 5x5x5 gold (111) cluster using tight-binding parameters from Ref. [77]. This was then utilized to calculate the spectral density associated with the coupling of the electrode to the 3s orbital of the adjacent sulfur atom. Specifically, we computed:

$$\Delta(E) = \pi \sum_{p} V_p^2 \delta(E - E_p), \tag{3.2}$$

where the summation was taken over the (Extended Hückel -level) eigenstates p of the gold atom cluster. We assumed that only the 6s orbital of the gold atom over which the sulfur atom is "bound" has a nonzero overlap with the 3s orbital of this sulfur atom. The Wolfsberg-Helmholtz prescription (3.1) was used to calculate the Hamiltonian matrix element connecting these two atomic orbitals, which was then scaled by the appropriate superposition coefficient in each EH eigenstate of the gold cluster to obtain V_p (i.e., the matrix element $V_{i,1}$ in the notation of the previous paragraph).

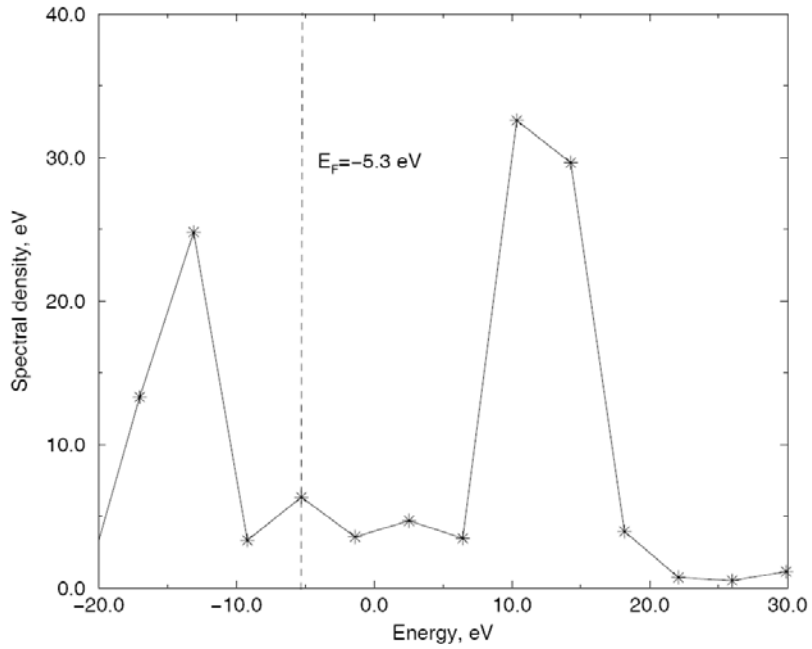

Figure 3-3. Spectral density of states for the model where sulfur binds to a single gold (111) atom. The Fermi Energy is located in a region with almost constant spectral density of states comprised mainly of gold s-band states.

The resulting spectral density of states is shown in Fig. 3.3. The "crudeness" of the plot results from numerical fluctuations of the calculations performed on a finite gold cluster. We carried out calculations for three different gold cluster sizes, 3x3x3, 5x5x5 and 7x7x7 -- these give similar results for the spectral density (the bigger the size of the cluster the smoother the numerical result). We see from Fig. 3.3 that the Fermi Energy corresponds to states in a broad band with nearly constant $\Delta(E) \approx 4.0\ \text{eV}$. The largest contribution to the spectral density near the Fermi Energy comes from the $6s$ gold band, which is a wide band with relatively constant local density of states at the Fermi Energy.

From $\Delta(E)$ we can obtain the self-energy $\Sigma(E)$ as [18-21]:

$$\Sigma(E) = \frac{P}{\pi}\int_{-\infty}^{+\infty}\frac{\Delta(E')\,dE'}{E'-E} + i\Delta(E) \tag{3.3}$$

Numerical calculation of the principal value integral (3.3) based on the spectral density depicted in Fig. 3.3 gives the real part of the self energy to be almost zero within an interval of several eV around the Fermi level. Thus, within this energy regime we can approximate:

$$\Sigma(E) \cong 0.0 + 4.0i \tag{3.4}$$

We have just described how we calculated the density of states $\Delta_{i,1}$, and corresponding self energy $\Sigma_{i,1}$, where 1 represents the 3s orbital of a sulfur atom which is chemisorbed at a distance of 1.9 Å from the L-electrode. If the sulfur atom on the right hand side of the molecule is chemisorbed to the R-electrode, the same density of density of states is used for $\Delta_{f,N}$ and the same self energy function for $\Sigma_{f,N}$. For the STM configuration, where the right electrode is 5 Å from the right sulfur atom, we estimate the relevant spectral density of states using the following empirically established property. In simple models of vacuum STM tunneling [78], the current decreases by about one order of magnitude when the tip-surface distance changes by one Angstrom. Hence we multiply the spectral density of states obtained above for the chemisorbed

sulfur atom by an appropriate coefficient of proportionality, reflecting the change in separation between the atom and the R-electrode.

3.1.3 Basis Transformation to Obtain a Diagonal Dipole Operator

As discussed above, our model assumes a constant dc electric field in the junction region, as well as an ac field of constant magnitude (at any given instant of time) in this region. Thus, the electric dipole operator plays a critical role in our dynamical theory. In particular, if the relevant (static and ac) external electric fields are polarized perpendicular to the metal electrodes (in the x direction), we need to evaluate $\mu_x = e_0 x$, the (negative of the) x-component of the dipole operator. It was tacitly assumed in constructing the relevant tight-binding Hamiltonian (see above) that μ_x is diagonal in the molecular site basis. This turns out to be roughly, but not precisely true for the AO site basis introduced above. Thus, it is useful to perform a linear transformation of the site orbitals to a set of basis states which are strictly diagonal with respect to the μ_x operator. Details are given next.

The dipole matrix, represented in a localized atomic site basis, was obtained as output from the Gaussian program. The origin of the coordinate system was chosen at the left electrode, hence the dipole moment is zero at the left electrode and increases towards the right electrode. Our Floquet analysis of the system Schrödinger Eq. assumes [chapter 2] that the field-wire coupling occurs only through the diagonal terms in the Hamiltonian. Thus we wish to construct a new orthogonal basis of bridge states in which the bridge dipole matrix is diagonal. We accomplish this through two successive basis transformations. First, from the original non-orthogonal site basis $|\chi_j>$, $j=1..N$ we construct an orthonormal basis ϕ_j, $j=1..N$ via the transformation $\phi_j = \sum_{k=1}^{N} S_{jk}^{-1/2} |\chi_j>$, where S is the overlap matrix in the χ (site) basis. Next we express the x-component of the electric dipole operator in the orthonormal ϕ basis (using the known matrix elements of μ_x in the $|\chi_j>$ basis). Diagonalization of this matrix determines another orthonormal basis, say $|\psi_j>$, $j=1..N$ in which the operator μ_x is diagonal. Finally, the Hamiltonian operator can be expressed in terms of the ψ basis. Inspecting the Hamiltonian matrix elements coupling the wire and electrodes in this basis, we find that the main

contributions to the left electrode-bridge coupling occur through two wire basis functions, and two other wire basis functions interact with the right electrode. Thus, for simplicity, in our electric current calculations we set all other small coupling matrix elements to zero.

Note that since there is more than one bridge basis state that couples to the reservoirs, the spectral density and self energy matrices introduced in Sect. 2.1 have more than one non-zero element. However, we assume here that only the $3s$ orbital of the sulfur atom couples electronically to electronic states of the gold electrode. This implies that if we use as bridge basis states the ψ states described in the preceding paragraph, then all non-zero spectral density matrix elements will be proportional to $\Delta(E)$ computed in Sect. 3.2; likewise, all non-zero self-energy matrix elements will be proportional to $\Sigma(E)$ (again, cf. Sect. 3.2). The relevant proportionality constants are obtained from the coefficients utilized to expand the ψ basis functions in terms of the original AO (χ) site basis orbitals.

3.2 TESTS OF THE FLOQUET MAPPING PROCEDURE

In this section we illustrate the accuracy of the Floquet method developed in chapter 2 to study the quantum dynamics of a field-driven molecular wire, moving beyond the simplistic model studied in chapter 2, and focusing instead on a realistic (or at least defensible) set of bridge states and interstate couplings. We consider for this purpose the STM configuration, in which the left end of the xylyl-dithiol molecule is located 1.9 Å from the left electrode, while the right end of the xylyl-dithiol molecule is significantly farther, specifically 5 Å, from the right electrode.

We solved the time-driven Schrödinger Equation corresponding to the Hamiltonian (2.17) by direct numerical integration of the appropriate set of linear ordinary differential equations. Starting with population in a single state i_0 of the L-reservoir, we calculated the total probability to be in a particular energetic region of the R-reservoir (based on energy conservation modulo photon absorption/emission). After short-time transients [chapter 2], a linear growth of the final-state probability was observed, thus defining a transition rate (cf. Eq. (2.13)). We then sought to verify via numerical comparison that the Floquet Green's function method outlined in Sect. 2.1 reproduces these rates reliably.

[In practice, direct integration of the time-driven system was done by representing the Left and Right electronic reservoirs using a finite set of states, evenly spaced in energy, and coupled to the bridge via matrix elements $V_{i,1}$ and $V_{f,N}$ selected in accordance with the spectral densities specified in the previous section. Convergence was obtained by increasing the number of discrete states in the reservoirs, while maintaining the desired (finite) spectral density by reducing the magnitude of the individual reservoir-bridge coupling elements accordingly.]

For a laser frequency of $\omega = 3.8$ eV and a laser field strength of $E_0 = 2 \times 10^7$ V/cm (with no applied static voltage, i.e., $V_{ap} = 0$), we show via the solid line in Fig. 3.4 the rate of transitions from a range of initially populated states below the Fermi energy (-5.3 eV) of the L-reservoir to all final states in the R-reservoir above the Fermi level (i.e., transitions to final states with energies less than E_F are blocked). These rates are scaled by the density of electronic states of the L-reservoir at the Fermi energy, in order to obtain a finite result in the limit of a dense set of reservoir states. The shape of this "spectrum" reflects the complicated molecular orbital structure of the xylyl-dithiol bridge molecule.

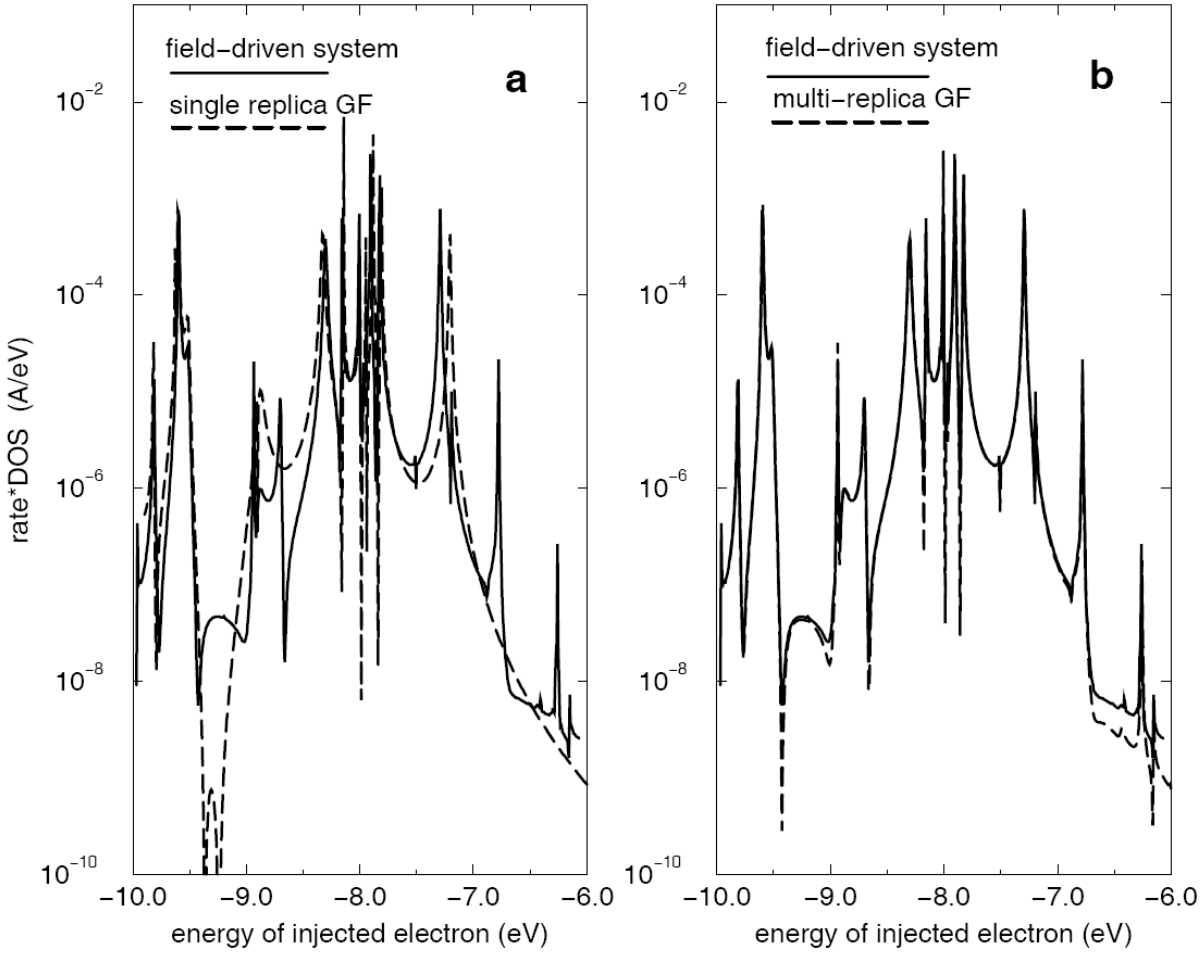

Figure 3-4. Tunneling rate dependence on initial energy of the electron in the L-electrode. The solid line in both panels shows the result obtained by direct integration of the time-dependent Schrödinger Eq. for the laser-driven system. In panel a, the dashed line shows the result of a restricted Floquet Green's function that retains only one (resonant) replica. See text for details. In panel b, the dashed line shows a Floquet Green's function calculation including 6 bridge and 9 L- and R- reservoir Floquet replicas. Note the good agreement with the result obtained by direct numerical integration of the time-dependent Schrödinger Equation in this case. Relevant field parameters are: $\omega = 3.8$ eV, $E_0 = 2\times10^7$ V/cm, and $V_{ap} = 0$ in both panels.

The dashed line in Fig. 3.4(a) shows a minimum basis attempt to extract the behavior of the time-driven system via Floquet analysis. Specifically, only the replicas $k_L = 0$, $k_B = 0$ and $k_R = -1$ are retained in the calculation. This corresponds to the following pathway for the incident electron: direct tunneling (without photon absorption/emission) from the L-reservoir to

the bridge, tunneling across the bridge (without photon absorption/emission), then 1-photon absorption to a final state of the R-reservoir. It can be seen that this single channel accounts for much of the detail in the exact spectrum, but misses some significant features (resonances). To correct for this shortcoming, we performed a larger basis Floquet Green's function computation: 6 bridge replicas (specifically, replicas -3...2) and 9 L- and R- reservoir replicas (specifically, replicas -4...4) were employed. The result is shown via the dashed line in Fig. 3.4(b). It reproduces the result of direct time-integration of the field-driven Schrödinger Eq. in all essential details. Thus, we see that the Floquet-GF method gives a practical way to obtain rates of electron transmission through a field-driven molecular wire coupled to two metal electrodes, provided proper care is taken to ensure convergence by including a sufficient number of Floquet replicas in the calculation. Consequently, in the numerical computations presented below, we use the GF method, since it is considerably faster than direct integration of the full set of ordinary differential equations required for “brute force” time-evolution of the laser-driven system.

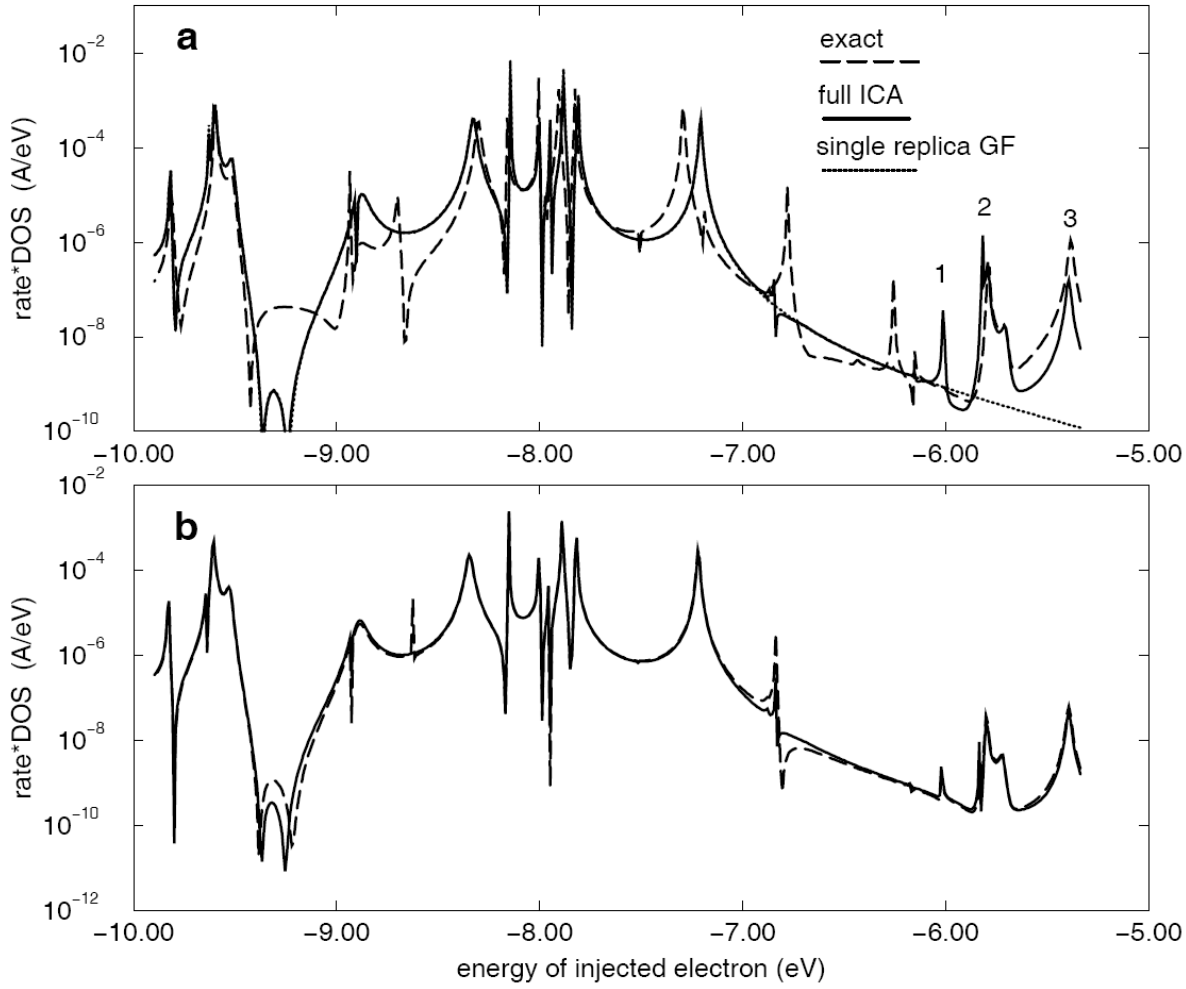

Figure 3-5. (a) The exact transition rate as a function of initial electron energy, calculated via the Floquet Green's function method (dashed line) vs the corresponding ICA result (solid line) for the system considered in Fig. 3.4. For comparison, the ''single channel'' result shown in Fig. 3.4(a) is also indicated via the dotted line. (b) The exact (dashed line) vs ICA (solid line) results for the same system when the dimensionless field strength parameters $a_{I,I'}$ inside the bridge are reduced by a factor of 10.

The minimum basis calculation just described is tantamount to a skeletal approximation to the ICA formula (2.30) in which only one term in the sum over amplitudes is retained. We show in Fig. 3.5(a) how this single term approximation compares to the full ICA result (using the same field parameters employed in Fig. 3.4). There is no substantial difference between the full ICA result and the single replica approximation to it in the incident electron energy regime considered in Fig. 3.4. Failures of the ICA and the single replica approximation in this regime

are thus due to inter-(bridge) replica coupling (representing photon absorption/emission on the bridge). In Fig. 3.5 we have extended the regime of incident energies above -6.0 eV. We see that the full ICA captures the additional peaks in this regime rather well. The origin of these peaks can be traced to other terms in the full ICA sum. In particular, the peaks marked 1 and 2 arise from the $k_B = 1$ term and peak 3 arises from the $k_B = -2$ term (in each case we sum over all R-reservoir replicas k_R which correspond to final states of the physical R-reservoir lying above the Fermi level). As a check on our analysis, we show in Fig. 3.5(b) the comparison between a converged multi-replica Floquet Green's function calculation vs the corresponding ICA prediction for the case where all the $a_{I,I'}$ parameters are reduced by a factor of 10. Setting these parameters to zero would imply complete suppression of inter-replica coupling in the Floquet Hamiltonian, thus improving the accuracy of the ICA. We see that the trend is in the right direction -- agreement between ICA and converged Floquet tunnel rate spectra is much better in panel b than in panel a.

Note that none of the transitions indicated in Figs. 3.4 and 3.5 would take place in the absence of the laser field, since they correspond to initial states of the L-reservoir below the Fermi level. By absorption of photons, electrons initially in these states can “get above” the Fermi energy and access an unoccupied state of the R-reservoir.

In fact, it is possible to employ a perturbative expansion for the Floquet Green's function to systematically correct for the deficiencies of the ICA and to provide insight into the specific intra-bridge photon absorption/emission events that contribute to the tunneling rate under various conditions. As noted above, the ICA corresponds to neglect of matrix elements in the inverse of $\mathbf{g}^F$ which connect different Floquet replicas, thus resulting in a block diagonal Floquet bridge Hamiltonian matrix, a block diagonal Floquet self-energy matrix, and hence a block diagonal approximation to $\mathbf{g}^F$. Treating the neglected matrix elements as the perturbation, a standard Green's function perturbation expansion can be invoked [62]. The first correction to the ICA provides the contribution of all process that involve one-photon absorption/emission between bridge states, etc. In a chapter 4 we will present full details of this expansion and demonstrate that it can correct the ICA into an essentially exact calculation, except at extremely high laser intensities, where the perturbation expansion diverges.

3.3 CURRENT THROUGH AN *AC* DRIVEN MOLECULAR WIRE

Here we present numerical calculations of the electrical current through an *ac* field-driven xylyl-dithiol molecular wire for a variety of externally tunable parameters. Having shown in Sect. 2.3 that the Floquet Green's function method enables us to accurately compute the quantum dynamics of the field-driven system, we use it to deduce the current through the wire in all calculations to be presented in the remainder of this chapter. (Care was taken to ensure that enough replicas were included in the numerical calculation to obtain converged results for the output current.)

In Section 3.3.1, we show the predicted current for fixed laser field strength and frequency as a function of applied *dc* voltage for the (symmetric) break-junction configuration. In Section 3.3.2, we present analogous calculations for the (asymmetric) STM configuration. Then, in Sect. 3.3.3, we investigate in more detail how weak the laser-field can be and still produce a significant enhancement of the electron current.

3.3.1 Break-Junction (Symmetric) Configuration

Here we consider a symmetric ("break-junction") system, corresponding to chemisorption (covalent bonding) of the xylyl-dithiol molecule at both ends to gold electrodes. For concreteness we take the electrode molecule distance to be 1.9 Å. Also for concreteness, we choose a laser frequency of 1.9 eV, which corresponds to one-half the HOMO-LUMO energy gap. Furthermore, we fix the laser field amplitude at the value $E_0 = 2\times10^7$ V/cm.

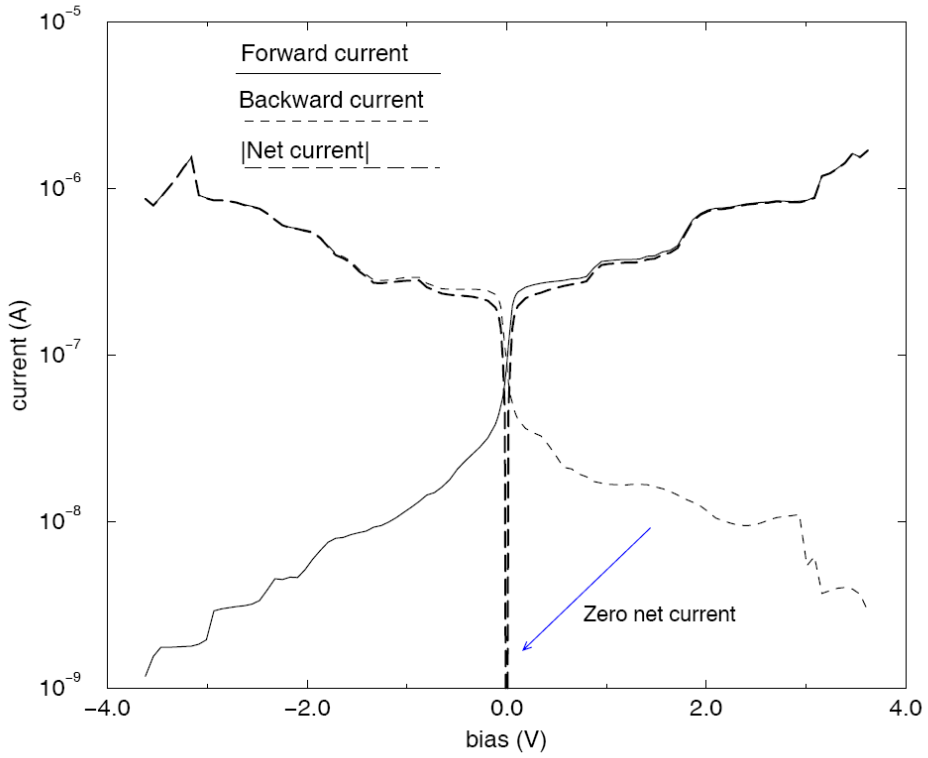

Figure 3-6. Laser-assisted current (in Amperes) through a xylyl-dithiol wire in the break-junction (symmetric) configuration. As a function of applied dc voltage (in Volts), forward (Left to Right) current is shown via solid line, backward (Right to Left) current via short-dashed line, and the absolute value of the net current is shown via long-dashed line. The following field parameters apply: $\omega = 1.9$ eV, and laser field strength $E_0 = 2\times 10^7$ V/cm.

In Fig. 3.6 we show the forward (Left to Right) and backward (Right to Left) currents as a function of applied dc bias [79]. Their difference (forward minus backward) gives the net Left to Right current through the wire. [Because a logarithmic scale is used in the graph, vanishing of net current is indicated by the sharp dip (towards $-\infty$) at zero bias. Note also that the absolute value of the net current is plotted. Current flows in the direction of the applied bias, that is Left to Right for positive bias and Right to Left for negative bias.] Notice that due to the geometrical symmetry of the break-junction configuration, the roles of forward and backward currents should simply be switched when the dc voltage polarity is reversed. Some artificial "symmetry-breaking" is apparent in these figures, due to slight asymmetry in the numerical placement of the

xylyl-dithiol atoms with respect to the metal electrodes. However, this asymmetry is minor, particularly as regards the net, experimentally observable current.

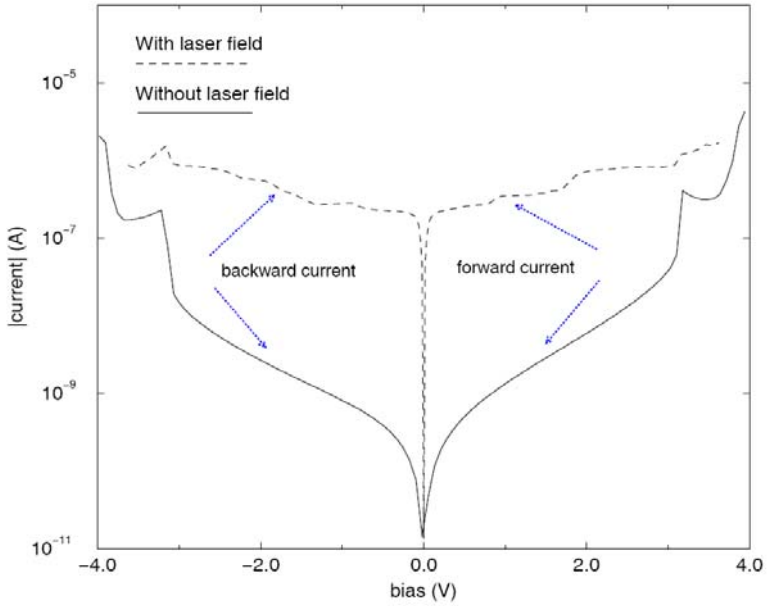

Figure 3-7. Current-voltage characteristic for the molecular wire system in the symmetric, break-junction geometry: the curve without the applied laser field is represented by the solid line, and the curve for the field-driven system is shown by the dashed line. The following field parameters apply: $\omega = 1.9$ eV, and laser field strength $E_0 = 2\times 10^7$ V/cm.

In contrast to the field-off case, where for small bias only electrons near the Fermi energy participate in the tunneling process, in the field-on case, electrons outside the energy regime bracketed by the Fermi levels of the L- and R- reservoirs participate as well (assisted by photon absorption/emission). Even for zero *dc* bias, many electrons in the metal reservoirs having energy well below the Fermi level contribute to forward and backward currents.

It is interesting to remark here that the vanishing of the net current at zero bias is due in the field-on case to perfect cancellation (for a symmetric electrode-wire-electrode configuration) of forward and backward currents. In Fig. 3.7, we again plot the net field-on current, and compare this to the current obtained when the laser field is turned off, all other system characteristics being unchanged. Two points about the magnitude of the current drawn through the wire are relevant. First, for the laser-off system with a modest applied voltage of ca. 1 V, the

current is ca. 10^{-9} Amps, a value which is in order of magnitude agreement with experimental measurements on break-junction systems [11]. Furthermore, it is clear that *large* enhancement of current flow are obtained over a wide range of *dc* voltages when a laser field of the amplitude and frequency noted above is applied.

3.3.2 STM (Asymmetric) Configuration

Here we consider an asymmetric, (STM) system, in which the left electrode - chemisorbed molecule distance is 1.9 Å and the STM tip - molecule distance is 5 Å. Again we choose a laser frequency of 1.9 eV, which corresponds to one-half the HOMO-LUMO energy gap. Furthermore, we again fix the laser field amplitude at the value $E_0 = 2\times10^7$ V/cm.

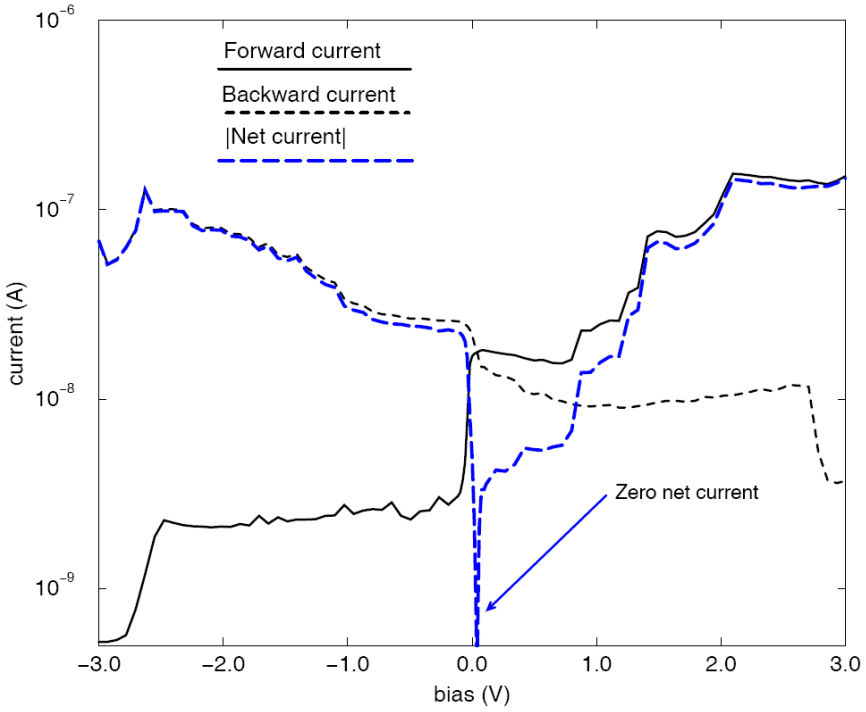

Figure 3-8. Laser-assisted current through a xylyl-dithiol wire in the (asymmetric) STM configuration. As a function of applied *dc* voltage, forward current is shown via solid line, backward current via short-dashed line, and the absolute value of the net current is shown via long-dashed line. The following field parameters apply: $\omega = 1.9$ eV, and laser field strength $E_0 = 2\times10^7$ V/cm.

In Fig. 3.8 we show the forward (Left to Right) and backward (Right to Left) currents as a function of applied *dc* bias. Their difference (forward minus backward) gives the net Left to Right current through the wire. Notice that due to the asymmetric geometry of the STM configuration, the symmetry between forward and backward currents found in the break-junction case (*vide supra*) is broken. In particular, it is interesting to note that the forward and backwards do *not* precisely cancel at zero *dc* voltage. In Fig. 3.9, we show via the dashed line the net current obtained under the input conditions just described as a function of applied *dc* bias. Again, this current represents the difference between forward current and backward current through the wire. The analogous result in the absence of the laser field is indicated via the solid line. We note that the value of current obtained for the "standard" wire (no laser field) is ca 10^{-11} Amps for a ca. 1 V *dc* bias, which agrees in order of magnitude with experimental measurements on xylyl-dithiol systems using an STM apparatus [19-21]. And, as in the break-junction case, it is clear that *large* enhancement of current flow (in fact, even larger than for the break-junction system studied in Sect. 3.3.1) is obtained with a laser field of the amplitude and frequency noted above.

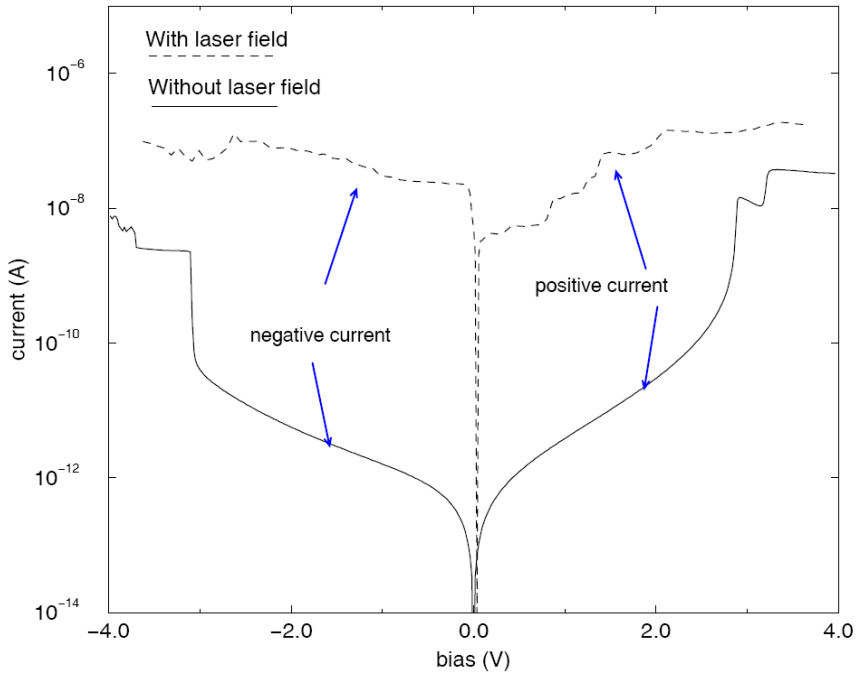

Figure 3-9. Current-voltage characteristic for the molecular wire system in the asymmetric, STM geometry: the result in the absence of the applied laser field is shown via the solid line; the corresponding result with the applied field is shown via the dashed line. The following field parameters apply: $\omega = 1.9$ eV, and laser field strength $E_0 = 2 \times 10^7$ V/cm.

3.3.3 Estimation of Laser Field Strengths Needed for Significant Current Enhancement

Here we tune the laser to resonance with the Fermi-Level to HOMO (and thus the Fermi-level to LUMO) energy gap, i.e. choose $\omega = 2.0$ eV. Then, for fixed applied voltage $V_{ap} = -0.4$ V, we study the dependence of the net electric current on laser field strength. Results are shown for both STM (asymmetric) and break-junction (symmetric) configurations in Fig. 3.10. In both cases we see that the backward current is much larger than the forward current, and hence accounts for almost the entire net current. For comparison, we also show the result obtained in the ICA approximation. The latter is seen to be reasonably good in the STM case and less so in the break junction case. (In the STM case, the large STM tip molecule distance causes photon assist in the "tip to molecule" step of the electron tunneling transition to dominate intra-bridge transitions; the latter require inter-replica coupling and hence are not contained in the ICA.) It is clear that for both configurations substantial enhancement relative to the non-driven (laser-off) system is observed. For a moderate field strength of 2×10^6 eV [80] (located by the dashed vertical line), an enhancement of over one order of magnitude relative to the laser-free limit is obtained for the break-junction geometry, while an enhancement of more than two orders of magnitude is obtained for the STM configuration.

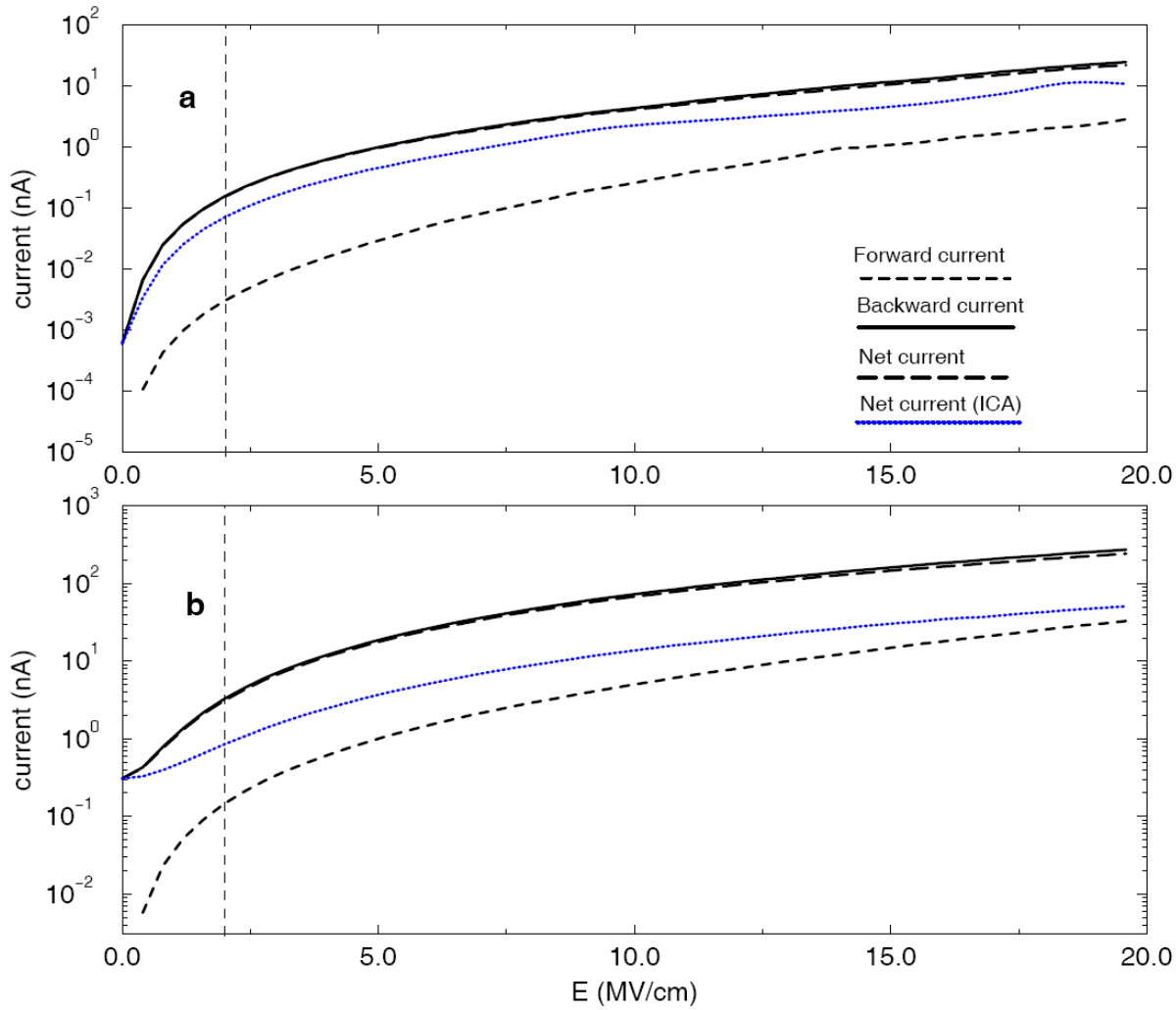

Figure 3-10. Dependence of electron current on laser field strength for the STM case (top panel) and break-junction case (bottom panel). In each panel, the full Floquet Green's function result for forward current is shown via the solid line, backward current via the short-dashed curve, and net current via the long-dashed curve. Net current computed within the ICA is shown via dotted line. The dashed vertical line highlights the large enhancements in net electric current obtained with a moderate laser field strength of 2×10^{6} V/cm. Relevant parameters include: bias $V_{ap} = -0.4$ V and field frequency $\omega = 2$ eV.

The essential effect of laser field illumination is to open up resonant photon-assisted conductance channels. The resultant resonant electron transfer processes depend only weakly on the number of sites through which the hopping takes place, i.e. the length of the molecular wire. In contrast, off-resonant electron transfer decreases *exponentially* with molecular wire length [18]. Since the Fermi level of the metal contacts lies in the (multi-eV) gap between HOMO and

LUMO orbitals of organic molecular wires like xylyl-dithiol and its multi-benzene analogs, current through this class of molecular wire system is predicted, in the absence of laser illumination, to fall off dramatically (exponentially) with the length of the molecular wire (neglecting dissipative effects associated with coupling to a condensed phase environment [81]). Thus we expect a larger field-induced enhancement factor for the electronic current as the molecular wire length increases.

3.4 DISCUSSION AND CONCLUSION

In this chapter we have applied the formalism developed in chapter 2 to study electron transport through *ac* field-driven molecular wires in the particular case of xylyl-dithiol connected at either end to gold electrodes. The simplest possible level of description has been invoked, namely a 1-electron tight-binding model for the electron dynamics. Dissipative coupling to an environment (for example, vibrations in the bridge molecule, phonons in the metal electrodes, and dipolar forces in a liquid solvent) has been neglected. Electron correlation effects, which would require a level of electronic structure theory considerably beyond the tight-binding model, are also ignored. Indeed, even if explicit electron-electron are ignored, the fermionic nature of the multi-electron system involved here has only been treated crudely (via a one-electron model in which certain transitions are blocked based on the expected prior occupancy of the final states accessed by these transitions). Despite the success of this approach in understanding electron transport through non-driven molecular wires [19-21, 54, 55], a more rigorous treatment of Fermi statistics would be of interest in the field-driven case, which is further complicated by photon-assisted transitions. A related issue, unaddressed here, is the importance of hole current in the overall charge carrier transport process.

We showed in chapter 2 that a molecular wire coupled to a monochromatic *ac* driving field such as results under laser illumination can be mapped, using Floquet theory, to an equivalent *ac* field-free ("ordinary") molecular wire system that corresponds to an augmented (formally infinite) electronic state space and appropriately renormalized inter-state couplings. With this mapping, standard Green's function methods, applicable in the field-off case, can be

applied to compute the electron dynamics in the field-driven system. If a sufficiently large number of Floquet replica states are included in the calculation, a numerically exact solution of the field-driven dynamics can be obtained. We also presented in chapter 2 an approximation scheme, termed the Independent Channel Approximation (ICA), which simplifies the analysis of the Floquet Hamiltonian by neglecting certain inter-Floquet state couplings.

In the present chapter this methodology was used to compute the net electric current through a xylyl-dithiol molecular bridge attached at either end to gold electrodes. Two geometric configurations were considered. One was symmetric with respect to the placement of electrodes on either side of the xylyl-dithiol molecule. A small electrode-molecule distance of 1.9 Å was employed in order to represent chemisorption of the sulfur atom from the xylyl-dithiol with gold atom(s) of the adjacent metal electrode. This was termed the "break junction" configuration. A second configuration considered one of the gold electrodes to be significantly farther (5 Å) from the adjacent sulfur atom of the molecule. This asymmetric configuration was chosen to model an STM experiment, in which the STM tip is at this distance from the molecule; hence it was termed the "STM" configuration. The geometric differences between these two configurations generate different electron-laser coupling, and hence lead to different induced currents when the same external fields are applied.

The parameters entering into the tight-binding model for this system were taken largely from Extended Hückel level electronic structure calculations. While these are crude, they have provided useful qualitative estimations in previous studies on similar systems [19-21]. Of course, improved electronic structure calculations would provide a valuable refinement of the overall theoretical treatment of electron transport through molecular wires, with or without laser driving.

The Fermi level of the electrodes (in the absence of applied *dc* voltage) lies near the middle of the HOMO-LUMO gap in xylyl-dithiol. This gap is almost 4 eV. In the absence of laser driving, and for modest applied *dc* bias, the tunneling electrons have energies approximately equal to the Fermi energy. Thus, tunneling is nonresonant and hence very inefficient, and the electron current is very small in the absence of any applied laser field. It is therefore desirable to illuminate the molecular wire/electrode system with light of frequency which brings occupied electrode states *into resonance* with particular bridge molecular orbital energies. This dramatically increases the tunneling. Of course, one has to check that the final energy state of the R-reservoir thus accessed is unoccupied and to balance (subtract) forward and

backward currents. But, we showed in several examples that this is possible to do in such a manner as to obtain a dramatically enhanced overall electric current through the wire, relative to the field-off analog.

Some testing of the accuracy of the ICA approximation in the context of the xylyl-dithiol molecular wire problem was carried out. The ICA was seen to be qualitatively successful in most cases -- successful enough to be used as a rough guide to the mechanism of current enhancement. However, for this particular molecule/model, the ICA was not successful at a quantitatively level. In particular, photon absorption/emission *within* the bridge molecule itself, rather than during the hopping of the electron from electrode to bridge or vice versa, is significant under the experimental conditions considered here. Thus, the ability to converge the Floquet Green's function analysis by coupling together several bridge replicas proved important in obtaining an accurate evaluation of electron transport for this periodically time-driven system.

We cannot be absolutely sure that other effects, not considered in the present model, will not substantially modify these conclusions. Dissipation, the full constraints of fermion statistics, and electron correlation, mentioned above, are three such effects. We were also naive in our treatment of the influence of the laser field on the metal electrodes themselves. We assumed that this laser field did not excite direct electronic transitions between metal states. For real metals, it is well established that light *does* in general induce such transitions [82]. The effect of such processes on the overall tunneling current remains to be ascertained. Clearly, much work remains to be done on this complex but intriguing problem.

Acknowledgement

We thank Prof. Abraham Nitzan for several illuminating conversations on this topic.

Chapter 4. Diagrammatic approach to express the laser driven current through molecular wires as interference of many tunneling pathways.

A single molecule connecting two metal electrodes (molecular wire) is an important molecular electronics system which lately has attracted considerable experimental and theoretical attention [1-33]. Applying electromagnetic fields to the molecular wire systems provide an interesting possibility to enhance and control the current flow through them. In chapters 2 we developed the theory of alternating current (ac) field driven electron transport through a molecular wire and in chapter 3 applied this theory to the realistic case of a xylyl-dithiol molecule connected two gold electrodes. We based this theory on a simple non-dissipative one-electron tight-binding model of molecular wire and describe coherent electronic transport by using the Landauer formula for the current. Floquet methodology [51] was used to construct a time-independent effective Hamiltonian from the original time-dependent Hamiltonian describing field-driven molecular wire. Then, electronic tunneling through the molecular wire system described by the time-independent Floquet Hamiltonian was calculated by using a standard Green's Function based scattering approach. Some insight on physical description of field-assisted electron tunneling was obtained by neglecting appropriate terms in the Floquet Hamiltonian [we called this Independent Channel Approximation (ICA)]. We tested the ICA on a system comprised of a xylyl-dithiol molecule connecting two gold electrodes to show that unfortunately ICA provides only approximate solution to the full quantum dynamics associated with the relevant tight-binding Hamiltonian. We would like to note here that contrary to the statement in ref. [60], our approach is exact for a model one-electron tight-binding Hamiltonian considered, and we fully take into account interference between different Floquet replicas: we use the independent channel approximation only to help to develop physical interpretation of the field-assisted tunneling.

In this chapter we expand our theoretical treatment by developing a perturbation theory approach to calculate electron tunneling rates. We partition the full Floquet Hamiltonian and utilize perturbation theory in a way that provides a clear physical description of field-driven electron tunneling as an interference of many pathways. Each such process has a specific physical interpretation as an electron site-to-site "hop" accompanied by possible photon absorption-emission. We use a diagrammatic technique to identify all possible pathways for electron transport and assign a specific algebraic term to each such pathway.

We test this method by comparing the exact and perturbative theories numerical results for both "toy" and realistic xylyl-dithiol molecular wires. We show that in the case of a xylyl-dithiol molecular bridge, which comprises many tight-binding states, and for the laser field intensities less then 10^7 *V/cm,* the exact result is numerically reproduced by taking into account just the first two terms in the perturbation series.

4.1 FLOQUET BASED THEORY OF LASER-DRIVEN COHERENT ELECTRON TRANSPORT THROUGH MOLECULAR WIRE

A molecular junction consists of a single molecule connecting two metal electrodes. Monochromatic electromagnetic field of frequency ω and amplitude E_0 is applied along the axis of the bridge molecule. The one-electron tight-binding Hamiltonian is used and coherent electron transport is described by using Landauer formula (details of the model and formalism used can be found in chapter 2). We assume that metal electrodes are perfect conductors and thus disregard the generation of field-induced excitations inside the metal.

The essence of our theoretical approach (described in chapter 2 and just briefly reviewed in this section) is the application of Floquet methodology to the Schrödinger Equation written in Interaction Picture representation. This removes the time dependence from the original molecular wire Hamiltonian $\mathbf{H}$ and defines a new time-independent Floquet Hamiltonian $\mathbf{H}^F$. The state diagram corresponding to the new Hamiltonian $\mathbf{H}^F$ has the following strucure: for each basis state of the physical molecular wire system there is a discrete manifold of (quasi) states

("replicas") of the effective Floquet system, shifted by $n \cdot \hbar\omega$ from the energy of the original physical state, where the *n* is an integer number.

The exact mapping of the effective time-independent Floquet Hamiltonian to the original time-dependent Hamiltonian is provided by the following scheme (we follow the notation of chapter 2 throughout): The original molecular wire Hamiltonian (Eq. 2.17) is defined by the following features. The Left reservoir basis states are denoted as $|i>$ and have energy E_i. They are not directly coupled to each other. The same is true of the Right reservoir states, which are denoted as $|f>$ and have energy E_f. Left and Right reservoir states are not coupled directly to each other. The bridge molecule is represented by a Hückel type Hamiltonian. The bridge N atomic orbitals are denoted as $|I>$, with energies E_I. These atomic states are coupled by matrix elements $V_{I,J}$. Finally, the coupling between any L-reservoir state i and a bridge atomic orbital I is designated by $V_{i,I}$. Analogously, $V_{f,I}$ designates the coupling between the R-reservoir state f and the bridge atomic orbital I.

Quasi-states of the effective Floquet system are defined by *two* indices (α, m), where the index $\alpha = i, I, f$ denote the physical state of the original Hamiltonian and the $m = \ldots -1,0,1 \ldots$ labels the replica. Specifically we use labels k_L, k_B, k_R for the replicas of correspondingly left reservoir, bridge and right reservoir quasi-states. The energy of Floquet state (α, m) [referred to as a "quasi-energy" to distinguish it from the physical site energies associated with the original molecular wire basis states], is

$$E_{\alpha,m} = E_\alpha + m\omega, \tag{4.1}$$

The off-diagonal matrix elements in the Floquet Hamiltonian represent the bridge-bridge and bridge-electrode coupling. The coupling between the L-reservoir Floquet states (*i*, k_L) and bridge Floquet states (*I*, k_B) is

$$H^F_{(i,k_L),(I,k_B)} = V_{i,I} J_{k_L - k_B}(a_{LI}); \tag{4.2}$$

where J_n is the Bessel function of order n and the field parameter $a_{\alpha\beta} = E_0(\mu_\alpha - \mu_\beta)/\hbar\omega$ ($\alpha, \beta = i, I, f$) specifies the appropriate dimensionless field-mater interaction strengths. The laser field interaction with the molecular junction is described (the details are provided in chapter 2) through by using the full dipole moment matrix with the elements (we assume them diagonal) μ_α corresponding to the atomic state α. The coupling between the bridge Floquet states is

$$H^F_{(I,k_B),(I',k_B')} = V_{I,I'} J_{k_B - k_B'}(a_{II'}); \tag{4.3}$$

and finally, the interaction between the bridge and R-reservoir Floquet states is

$$H^F_{(f,k_R),(I,k_B)} = V_{f,I} J_{k_R - k_B}(a_{RI}) \tag{4.4}$$

The laser field driven coherent charge transfer across a molecular junction we describe as an electron transfer in an effective system described by time-independent Floquet Hamiltonian. Applying the scattering formalism to the Landauer formula we obtain the one-electron rate of the isoenergetic transition from an initial L-reservoir Floquet state (i, k_L) to the manifold of all final Floquet states of the R-reservoir as:

$$r_{(i,k_L)} = \sum_{f,k_R} \frac{2\pi}{\hbar} |\vec{v}^L \cdot \mathbf{G}(E_{(i,k_L)}) \cdot \vec{v}^R|^2 \, \delta(E_{(f,k_R)} - E_{(i,k_L)}) \tag{4.5}$$

Here the vectors $\vec{v}^L$ and $\vec{v}^R$ describe the coupling between the molecule and the electrodes and vector elements of $\vec{v}^L$ are given by $v^L_{(I,k_B)} = H^F_{(I,k_B),(i,k_L)}$ and likewise for $\vec{v}^R$. The Green's function matrix $\mathbf{G}$ of the molecular junction Floquet Hamiltonian $\mathbf{H}^F$ can be calculated as:

$$\mathbf{G}(E) = \left[E - \mathbf{H}^B - \mathbf{\Sigma}(E)\right]^{-1} \tag{4.6}$$

where $\mathbf{H}^B$ is the bridge Floquet Hamiltonian matrix and $\mathbf{\Sigma}$ is the E-dependent "self-energy" matrix, which decomposes as

$$\mathbf{\Sigma}(E) = \mathbf{\Sigma}^L(E) + \mathbf{\Sigma}^R(E), \tag{4.7}$$

with elements:

$$\Sigma^L_{(I,k_B),(I',k_B')}(E) = \sum_{i,k_L} \frac{V_{(i,k_L),(I,k_B)} V_{(i,k_L),(I',k_B')}}{E - E_{(i,k_L)} + i\eta}, \tag{4.8}$$

and $\eta \to 0^+$. Similar expression may be easily written for $\mathbf{\Sigma}^R(E)$. By using the self-energy defined for an original Hamiltonian of the physical system $\Sigma^{bridge} = \Sigma^{L,bridge} + \Sigma^{R,bridge}$ we can write:

$$\Sigma^L_{(I,k_B),(I',k_B')}(E) = \sum_{k_L=-\infty}^{\infty} J_{k_L - k_B}(a_{LI}) J_{k_L - k_B'}(a_{LI'}) \Sigma^{L,bridge}_{I,I'}(E - k_L \hbar\omega) \tag{4.9}$$

The total current I_{tot} is the difference between the forward (Left electrode to the Right electrode) current I_{for} and the backward current I_{back} and composed from all possible one-electron contributions. We assume that initially electrons are distributed according to the equilibrium Fermi distribution and tunnel from the occupied states of one electrode to the unpopulated states of the opposite electrode. The driven electron transport is accompanied by photon absorption and emission and thus is not necessarily isoenergetic. In our effective Floquet system the electronic transport occur isoenergetically, and photon absorption-emission processes are described as electron tunneling between different Floquet replicas.

To determine the forward current we need to sum all individual contributions from the electrons occupying the L-electrode (as an initial condition we choose that only the L-electrode replica $k_L = 0$ is occupied) tunneling to the unoccupied quasi-states of R-electrode. The electron with energy E_i occupying the zero replica $k_L = 0$ state of the L-electrode may absorb/emit n

net photons and end up at the R-electrode replica $k_R = -n$ ($k_R = n$ in case of emission) state with final energy $E_i + n\hbar\omega$. If (assuming the temperature $T = 0$) this final energy is below the R-electrode Fermi energy, than these final states are already occupied and the tunneling to them is blocked. The forward current thus takes the form:

$$I_{for} = \sum_{i,k_L=0} r_{(i,k_L)} = \sum_{i,k_L=0} \sum_{f,k_R} \frac{2\pi}{\hbar} |\vec{v}^L \cdot \mathbf{G}(E_{(i,k_L)}) \cdot \vec{v}^R|^2 \, \delta(E_{(f,k_R)} - E_{(i,k_L)}) \tag{4.10}$$

where the first sum is performed over occupied L-reservoir quasi-states i located in replica $k_L = 0$ and the second sum is performed over only unblocked k_R's. Likewise we can write the similar expression for the backward current I_{back}. We note here the important difference between field-on and field-off case: in the presence of a laser driving field any electron has a non-zero probability to tunnel to the opposite electrode. In the language of the effective Floquet system this means that for any electron located at one electrode there always exist possible isoenergetic transitions to unoccupied states of some replicas of another electrode. Physically this can be interpreted that even if the electron is initially located far below the Fermi energy, it can still end up at an unoccupied state of another electrode by net absorption of an integer number of photons. Determination of the total field-driven current should consist of careful summation of all possible tunneling channels (pathways) for all electrons in the system (chapter 3). For a not very strong laser field, the bigger the number of photons that are involved in specific tunneling pathway, the less probable is the transition[1]. The electrons located far below the Fermi energy have to absorb many photons to be able to end up at the empty states of the opposite electrode and their tunneling rates are generally lower then the rates from the electrons closer to the Fermi

[1] The typical distance between any two interacting atomic sites i and j is not bigger then several Angstroms. Then the corresponding field parameter a_{ij} is (much) less then 1 for a field strength smaller than that needed to break chemical bonds. In the effective Floquet system, the tunneling pathway involving absorbing-emitting of n photons is described by the coupling matrix elements between the quasi-states of two different replicas with the replica numbers difference equal n. The coupling between such two replicas is proportional to the Bessel function element $J_n(a_{ij})$ and rapidly decreases with increasing n.

energy. In practice we calculate the total current by including the contributions from all initially occupied electronic states located above a preset cutoff energy E_{cutoff} and disregarding the negligible (checked numerically) contribution to the net current from the electrons located below E_{cutoff}.

In contrast with driven molecular wire, when there is no laser field only limited number of electrons participate in current as determined by applied voltage bias and the electron Fermi distribution in the electrodes. In the limit of zero temperature only the electrons having energies between the electrodes Fermi levels participate in current.

We can simplify the "accounting" process of deciding which R-electrode replicas are blocked and which are allowed for tunneling from the L-electrode by noting that the tunneling rate from state i on the L-electrode to the state f on the R-electrode is equal to the rate of opposite process of tunneling from the f to the i. If both states i and f are already occupied, their contributions are equal and opposite to each other and thus cancel in the total current. We introduce new forward current I_{for}' as a sum of contributions from all electrons from the L-electrode allowed to tunnel to all possible (assumed empty) states of R-electrode. In the new forward current we do not block the transport to the previosly occupied states of R-electrode. Mathematically we use all possible k_R's in the second sum in Eq. (4.10). In the limit of temperature $T = 0$ and truncating the summation below energy value E_{cutoff} we can replace the sum by an integral:

$$I_{for}^{'} = \frac{2}{\pi\hbar}\int_{E_{cutoff}}^{E_F} dE\ \mathrm{tr}\{\mathbf{\Delta}^L(E)\mathbf{G}(E)\mathbf{\Delta}^R(E)\mathbf{G}^{\dagger}(E)\} \tag{4.11}$$

with:

$$[\mathbf{\Delta}^L(E)]_{(I,k_B),(I',k_B')} = \pi\sum_{i,k_L} V_{(i,k_L),(I,k_B)} V_{(i,k_L),(I',k_B')}\delta(E - E_{(i,k_L)}) \tag{4.12}$$

and a similar expression for $\mathbf{\Delta}^R(E)$. We define a new backward current I_{back}' in the same manner as the new forward current, and the total current is:

$$I_{tot} = I_{for} - I_{back} = I_{for}' - I_{back}' \tag{4.13}$$

4.2 PERTURBATION THEORY APPROACH TO ELECTRONIC TRANSPORT THROUGH THE EFFECTIVE FLOQUET MOLECULAR WIRE

The central problem in the scattering approach to calculate electronic tunneling rates through a molecular wire system is the calculation of Green's function matrix $\mathbf{G}$ determined by Eq. (4.6). Let us assume the bridge tight-binding set of basis functions consist of N functions (states). The bridge Floquet Green's function matrix $\mathbf{G}$ and the corresponding Floquet Hamiltonian matrix $\mathbf{H}^B$ are formally infinite because of the infinite number of bridge Floquet replicas. In chapter 2 and chapter 3 we retained the finite number of replicas containing quasi-states having quasi-energies closest to the energy of tunneling electron. Numerically we were increasing the number of replicas till converging to a self-consistent result for the electronic tunneling rate. If N_b bridge replicas are retained, the matrixes $\mathbf{H}^B$ and $\mathbf{G}$ have dimensions $N_b N \times N_b N$ where N is the number of bridge atomic basis states. Thus the numerical overload to diagonalize this matrix quickly increases with the increase of the number of replicas.

It is possible to reduce the size of the effective Floquet Hamiltonian matrix by partitioning this Hamiltonian and then applying the perturbation theory to simplify it. The Floquet bridge Hamiltonian matrix consist of the blocks representing individual bridge replicas. For example, the truncated Floquet Hamiltonian matrix of dimension $N_b N \times N_b N$ consist of N_b diagonal blocks representing the replicas of physical bridge, and the $N_B \times N_B - N_B$ non-diagonal blocks representing the coupling between the bridge replicas.

Dynamics of electron transport through the molecular wire is described by the effective bridge Floquet Hamiltonian $\mathbf{H}$, which is just the bridge Floquet Hamiltonian with added self-energy (which takes into account coupling of the bridge molecule with the reservoirs of metal states), $\mathbf{H} = \mathbf{H}^B + \mathbf{\Sigma}(E)$. We choose (we explain this choice later) as a zero order Hamiltonian $\mathbf{H}_0$ the block diagonal part of the effective bridge Hamiltonian $\mathbf{H}$ consisting of only the replicas of the bridge molecule with corresponding self-energy terms. The perturbation $\mathbf{V}$ is chosen as the off-diagonal inter-replica part of the same Hamiltonian and so $\mathbf{H} = \mathbf{H}_0 + \mathbf{V}$.

We partition the effective bridge Floquet Hamiltonian $\mathbf{H}$ into $N_B \times N_B$ blocks, where N_B is the number of bridge replicas. Every diagonal block *(i,i)* with dimensions $N \times N$ contains all matrix elements of the specific bridge replica *i*, and *N* is the number of bridge states. Each individual block (i, j) we label as $\mathbf{H}^{ij}$, where i and j are the bridge replica numbers. We use a similar partitioning scheme and notation for other relevant matrixes, i. e., $\mathbf{G}$, $\mathbf{V}$, $\mathbf{H}_0$. Indices i and j here label the bridge replica number. We label by $\mathbf{h}^{(i)}$ the blocks corresponding to individual bridge replicas (i,i), where $\mathbf{h}^{(i)} = \mathbf{H}^{ii}$. We label matrices denoting off-diagonal blocks of the $\mathbf{H}$ by $\mathbf{V}^{ij}$.

If the total (truncated) Floquet Hamiltonian $\mathbf{H} = \mathbf{H}_0 + \mathbf{V}$ consist of only three bridge replicas, i. e., $N_b = 3$, then the explicit expressions for the $\mathbf{H}_0$ and $\mathbf{V}$ matrixes are:

$$\mathbf{H}_0 = \begin{pmatrix} \mathbf{h}^{(1)} & 0 & 0 \\ 0 & \mathbf{h}^{(2)} & 0 \\ 0 & 0 & \mathbf{h}^{(3)} \end{pmatrix}, \quad \mathbf{V} = \begin{pmatrix} 0 & \mathbf{V}^{12} & \mathbf{V}^{13} \\ \mathbf{V}^{21} & 0 & \mathbf{V}^{23} \\ \mathbf{V}^{31} & \mathbf{V}^{32} & 0 \end{pmatrix} \tag{4.14}$$

Now we calculate molecular wire full Floquet Green's function $\mathbf{G}$ by carrying out the perturbation expansion:

$$\mathbf{G} = \mathbf{G}_0 + \mathbf{G_0 V G_0} + \mathbf{G_0 V G_0 V G_0} + \ldots \tag{4.15}$$

where $\mathbf{G}_0$ is the Green's function for unperturbed Hamiltonian $\mathbf{H}_0$. By performing the necessary matrix algebra we can obtain the expressions for each term in the expansion for $\mathbf{G}$. Using our example with $N_b = 3$ replicas we can write the first and second terms of the expansion as:

$$\mathbf{G}_0 = \begin{pmatrix} \mathbf{g}^{(1)} & 0 & 0 \\ 0 & \mathbf{g}^{(2)} & 0 \\ 0 & 0 & \mathbf{g}^{(3)} \end{pmatrix}, \quad \mathbf{G_0 V G_0} = \begin{pmatrix} 0 & \mathbf{g}^{(1)}\mathbf{V}^{12}\mathbf{g}^{(2)} & \mathbf{g}^{(1)}\mathbf{V}^{13}\mathbf{g}^{(3)} \\ \mathbf{g}^{(2)}\mathbf{V}^{21}\mathbf{g}^{(1)} & 0 & \mathbf{g}^{(2)}\mathbf{V}^{23}\mathbf{g}^{(3)} \\ \mathbf{g}^{(3)}\mathbf{V}^{31}\mathbf{g}^{(1)} & \mathbf{g}^{(3)}\mathbf{V}^{32}\mathbf{g}^{(2)} & 0 \end{pmatrix} \tag{4.16}$$

where $N \cdot N$ matrixes $\mathbf{g}^{(i)}$ denote Green's function matrixes for individual bridge replicas $\mathbf{g}^{(i)} = (E - \mathbf{h}^{(i)})^{-1}$. In general we can express individual blocks $\mathbf{G}^{ij}$ of the full matrix $\mathbf{G}$ by using the blocks $\mathbf{G}_0^{ij}$ and $\mathbf{V}^{ij}$ as:

$$\mathbf{G}^{ij} = \mathbf{G}_0^{ij} + \mathbf{g}^{(i)}\mathbf{V}^{ij}\mathbf{g}^{(j)} + \mathbf{g}^{(i)}\left(\sum_k (\mathbf{V}^{ik}\mathbf{g}^{(k)}\mathbf{V}^{kj})\right)\mathbf{g}^{(j)} + \ldots \tag{4.17}$$

As a reminder we note that off-diagonal blocks $\mathbf{G}_0^{ij} = 0$ $(i \neq j)$, diagonal blocks $\mathbf{G}_0^{ii} = \mathbf{g}^{(i)}$ and $\mathbf{V}^{ii} = 0$.

We carry out further development of the perturbation approach by considering a simple model of the bridge molecule which consists of only three localized atomic states. We assume that only the first bridge state couples with the left electrode and only the third bridge state couples with the right electrode. Inside the bridge we adopt nearest-neighbor interaction model: only adjacent bridge states couple to each other; thus, the first bridge state couples with the second and the second state couples with the third.

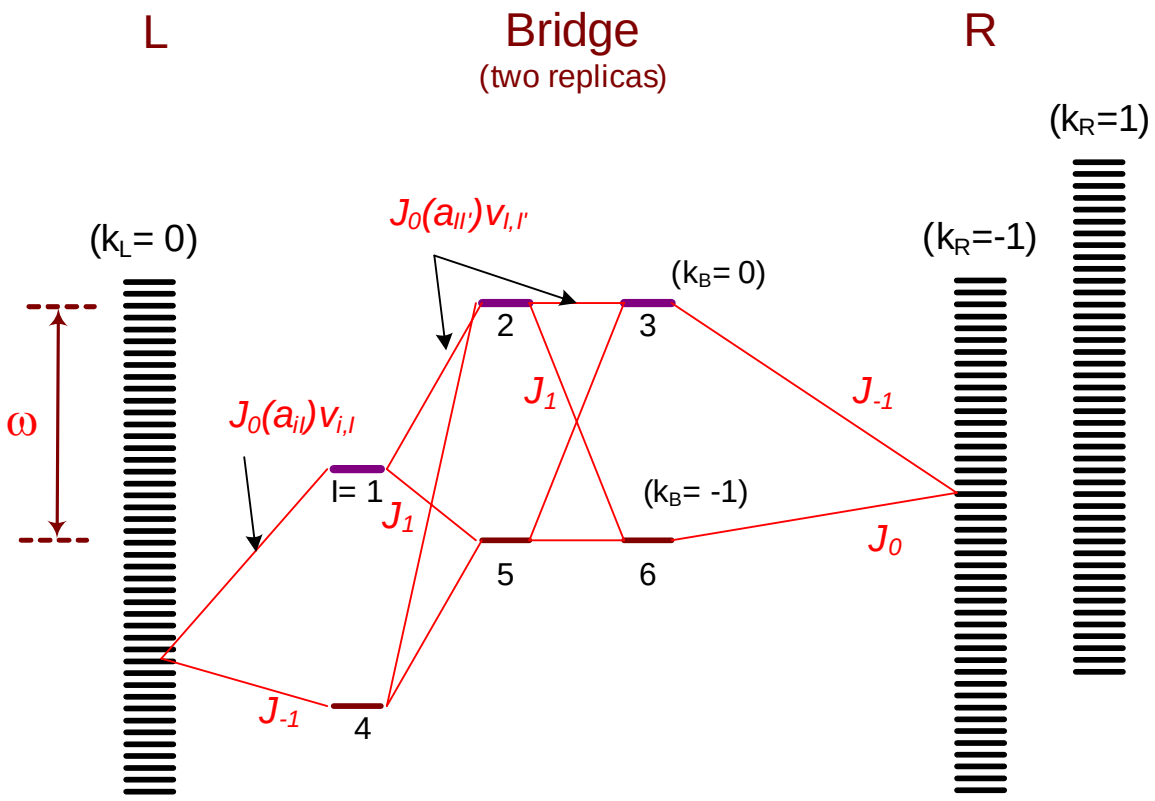

Figure 4-1. Floquet state diagram for field-driven three state bridge molecular wire. Only two replicas of the bridge are shown. Thin red lines depict all coupling matrix elements between the L-electrode states of the replica $k_L = 0$, states belonging to the two bridge replicas, and states of the $k_R = -1$ replica of the R-electrode..

The Floquet state diagram for this model is depicted in Fig. 4.1. For simplicity, we start our analysis by taking into consideration only two bridge replicas $k_B = 0$ and $k_B = -1$. We wish to calculate the tunneling rates for the electron, initially located at the L-reservoir quasi-state of replica $k_L = 0$ to the states of the replica k_R of the R-reservoir. The bridge first replica $k_B = 0$ consists of three (quasi) states labeled as $I = 1,2,3$ while the second replica has states labeled as $I = 4,5,6$. In Fig. 4.1 we plot by red lines the matrix elements of the full Floquet Hamiltonian corresponding to the coupling between the quasi-states of these two bridge replicas, between the bridge and L-reservoir quasi-state i and between the bridge and R-reservoir quasi-state f. The appropriate coupling matrix elements are given by:

$$v_{i,I} = H^F_{(i,k_L=0),(I,k_B)} \tag{4.18}$$

$$v_{I,I'} = H^{F}_{(I,k_B),(I',k_B')} \tag{4.19}$$

$$v_{I,f} = H^{F}_{(I,k_B),(f,k_R)} \tag{4.20}$$

The tunneling rate r from the quasi-state i of the left electrode to the quasi-states f of right electrode replica k_R is determined by:

$$r = \frac{2\pi}{\hbar}\sum_{f} T^2 \delta(E_f - E_i) \tag{4.21}$$

where T is:

$$T = v_{i,1}G_{1,3}v_{3,f} + v_{i,4}G_{4,6}v_{6,f} + v_{i,1}G_{1,6}v_{6,f} + v_{i,4}G_{4,3}v_{3,f} \tag{4.22}$$

Next we calculate matrix elements of the full Green function $\mathbf{G}$ in Eq. (4.22) by using the perturbation expansion (4.15) and the perturbation terms expressions (4.16) and (4.17). We approximate the full Green function by truncating the expansion after several perturbation terms. We call this approximation Independent Channels Approximation (ICA), and it is an extension of the approximation introduced in chapter 2, where we approximated full Green's function by only zeroth order perturbation term $\mathbf{G_0}$. We use the following terminology: ICA0 approximates the full Green's function by keeping only the zeroth order term $\mathbf{G_0}$ in the expansion; in ICA1 we add the first order perturbation term $\mathbf{G_0 V G_0}$ to the $\mathbf{G_0}$, in ICA2 – the second, and so forth. The calculation of the tunneling rate 4.5 can be performed by expanding the total Green function $\mathbf{G}$ as a sum of perturbation terms (4.17). Based on this infinite series (4.17), the final analytical expression for the tunneling rate would include the summation over infinite number of terms, each of them containing the matrix elements of bridge replicas Hamiltonian $\mathbf{h}^{(i)}$, Green's function matrix $\mathbf{g}^{(i)}$ and elements of the inter-replica blocks $\mathbf{V}^{ij}$. The explicit expressions for matrices $\mathbf{h}^{(1)}$ and $\mathbf{V}^{12}$ for our simple model consisting of the 6 bridge Floquet states are (similar expressions for $\mathbf{h}^{(2)}$ and $\mathbf{V}^{21}$ can be easily written):

$$\mathbf{h}^{(1)} = \begin{pmatrix} E_1 + \Sigma_{1,1} & v_{1,2} & 0 \\ v_{2,1} & E_2 & v_{2,3} \\ 0 & v_{3,2} & E_3 + \Sigma_{3,3} \end{pmatrix}, \qquad \mathbf{V}^{1,2} = \begin{pmatrix} \Sigma_{1,4} & v_{1,5} & 0 \\ v_{2,4} & 0 & v_{2,6} \\ 0 & v_{3,5} & \Sigma_{3,6} \end{pmatrix} \tag{4.23}$$

where E_1, E_2, E_3 are the quasi-states energies of the bridge replica $k_B = 0$.

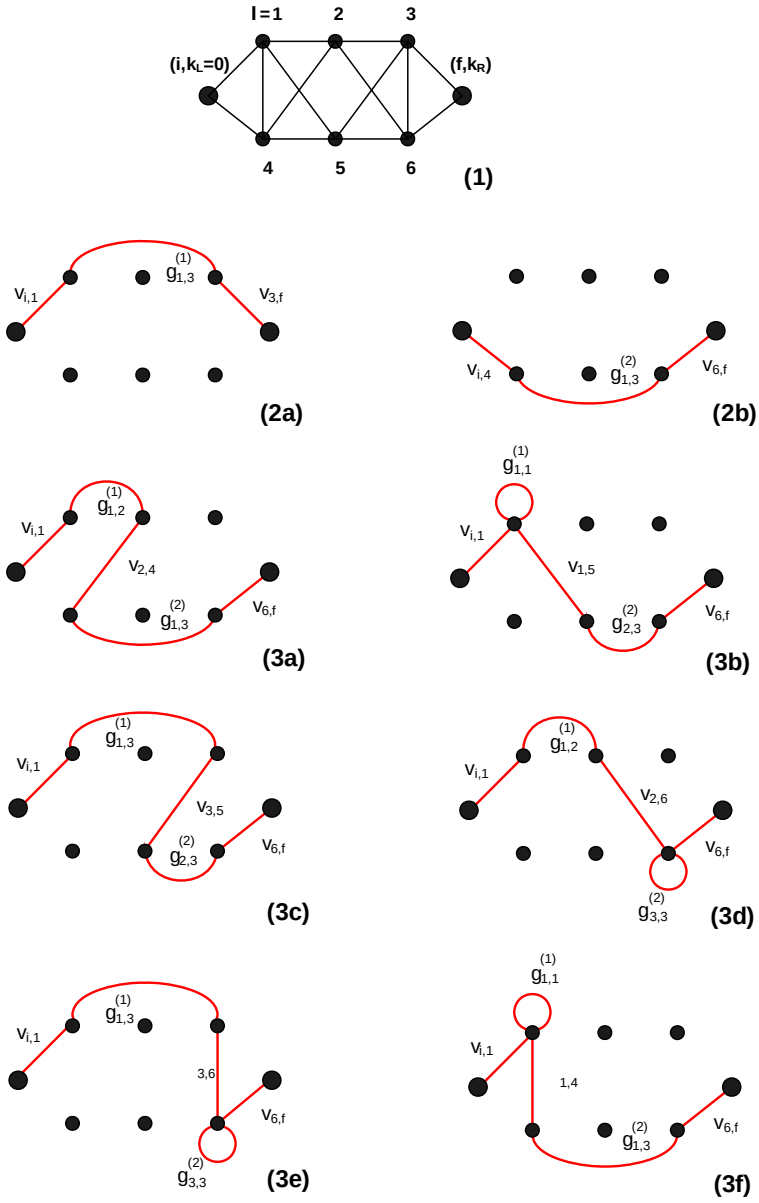

Figure 4-2. Perturbation diagrams: diagram 1 represent coupling scheme between six bridge Floquet states and left and right electrodes. Perturbation terms contributing to the electron tunneling rates are represented by the

diagrams 2a-2b (zero order perturbation) and 3a-3f (first order perturbation). Each continuous line in the perturbation diagram corresponds to a specific term, indicated nearby.

Substituting (4.23) into the expansion (4.17) and then into the tunneling rate expression (4.22), we express the total tunneling rate T as a sum of the infinite number of algebraic terms. Next we introduce the pictorial diagrams corresponding to the every term from this expansion. We build the diagrams sequentially, first for the ICA0 zeroth order perturbation term of Eq. 4.17, then for the ICA1 first order perturbation. In Fig. 4.2 we plot the diagrams corresponding to the all algebraic terms contributing to the ICA0 and ICA1. The T of Eq. (4.22) in the ICA0 approximation consists of only the first two terms and is represented by diagrams 2a and 2b (we explain later the details of our diagram construction). The ICA1 contribution for these two terms is zero, while keeping only the zero-order perturbation terms (ICA0) gives:

$$v_{i,1}G_{1,3}v_{3,f} = v_{i,1}g^{(1)}_{1,3}v_{3,f}, \tag{4.24}$$

$$v_{i,4}G_{4,6}v_{6,f} = v_{i,4}g^{(2)}_{1,3}v_{6,f}, \tag{4.25}$$

The diagrams 3a-3f represent terms responsible for the first order perturbation contribution in the third term of Eq. (4.22):

$$\begin{aligned} v_{i,1}G_{1,6}v_{6,f} = v_{i,1}[&g^{(1)}_{1,2}v_{2,4}g^{(2)}_{1,3} + g^{(1)}_{1,1}v_{1,5}g^{(2)}_{2,3} + g^{(1)}_{1,3}v_{3,5}g^{(2)}_{2,3} + \\ &g^{(1)}_{1,2}v_{2,6}g^{(2)}_{3,3} + g^{(1)}_{1,3}\Sigma_{3,6}g^{(2)}_{3,3} + g^{(1)}_{1,1}\Sigma_{1,4}g^{(2)}_{1,3}]v_{6,f} \end{aligned} \tag{4.26}$$

and the last term appearing in expression for T in Eq. (4.22) is:

$$\begin{aligned} v_{i,4}G_{4,3}v_{3,f} = v_{i,4}[&g^{(2)}_{1,2}v_{5,1}g^{(1)}_{1,3} + g^{(2)}_{1,1}v_{4,2}g^{(1)}_{2,3} + g^{(2)}_{1,3}v_{6,2}g^{(1)}_{2,3} + \\ &g^{(2)}_{1,2}v_{5,3}g^{(1)}_{3,3} + g^{(2)}_{1,3}\Sigma_{6,3}g^{(1)}_{3,3} + g^{(2)}_{1,1}\Sigma_{4,1}g^{(1)}_{1,3}]v_{3,f} \end{aligned} \tag{4.27}$$

The diagram 1 presents the coupling scheme for the six bridge Floquet states $I = 1,2,3,4,5,6$ (smaller dots on the diagram) and two electrodes (larger dots). Straight lines represent the coupling between the specific states. According to the coupling scheme 1 we build

the diagrams, representing all possible pathways between the two electrodes. The diagrams 2a-3f provide pictorial representation of different terms appearing in tunneling rates formula for T by using the following rules: straight red lines connecting the dots I and I' represent the coupling terms $v_{I,I'}$ between the correspondent Floquet states, vertical straight red lines correspond to the indirect coupling between the states adjacent to electrodes through self-energy terms. Non-straight red lines connecting the dots belonging to the same bridge replica represent the Green's function matrix elements for this replica. Thus the continuous red line connecting the (electrode's) dots and consisting of alternating straight and non-straight lines represents the specific algebraic term of the Eq. (4.24-4.26).

By using the diagrammatic representation we can easily generate algebraic expressions contributing to the total tunneling rate T. All terms contributing to the T can be expressed as a combination of all possible pathways connecting two electrodes (represented by large dots). Every pathway consists of alternating straight and curved lines. Different orders of perturbation correspond to the different number of straight lines connecting different bridge replicas: ICA0 approximation does not include any transitions between replicas and thus possible pathways are represented by two diagrams 2a and 2b. By including possible one-photon transitions between bridge replicas (represented by a single straight line connecting states from different replicas), we construct the possible pathways representing ICA1 first-order perturbation terms. Half of the possible pathways are depicted by the diagrams 2a-2f and correspond to the terms of Eq. (4.26). The other half of the diagrams denoting the terms of the equation Eq. (4.27) can be similarly generated by mirror interchange between these two bridge replicas.

The use of diagrams can be easily generalized to any number of Floquet replicas and therefore describes all possible photon-assisted tunneling channels. For the second order perturbation (ICA2), all algebraic terms in the total tunneling rate can be similarly deduced by elucidating all possible pathways involving two inter-replica transitions and writing the corresponding algebraic terms. A similar procedure can be developed for the perturbations of higher orders.

4.3 CASE STUDY: THE BRIDGE MOLECULE CONSISTS OF THREE ATOMIC STATES.

The suggested procedure of expressing the total tunneling rate as a sum of algebraic terms connected to a specific pictorial diagram provides an interpretation of the laser field coherent tunneling as an interference of many channels. Next we utilize this interpretation to explain the specific peaks in calculated tunneling rates as a result of resonant enhancement of a specific channel. In Fig. (4.3) we calculate tunneling rates vs tunneling energy for the molecular bridge consisting of three atomic states. On the top panel, all bridge states have the same energy of 0.8 (a. u.) while at the bottom panel the first bridge state has the energy of 0.2 and other two states energies are 0.8. Other parameters, common for both panels are: the field frequency is 0.6, the intra-bridge and inter-bridge field parameters are correspondingly $a = 1$ and $a = 0.2$, the inter-bridge coupling between the adjacent sites is -0.07. For the exact calculations we use 5 bridge replicas with $k_B = -2..2$ and 7 replicas of each electrode.

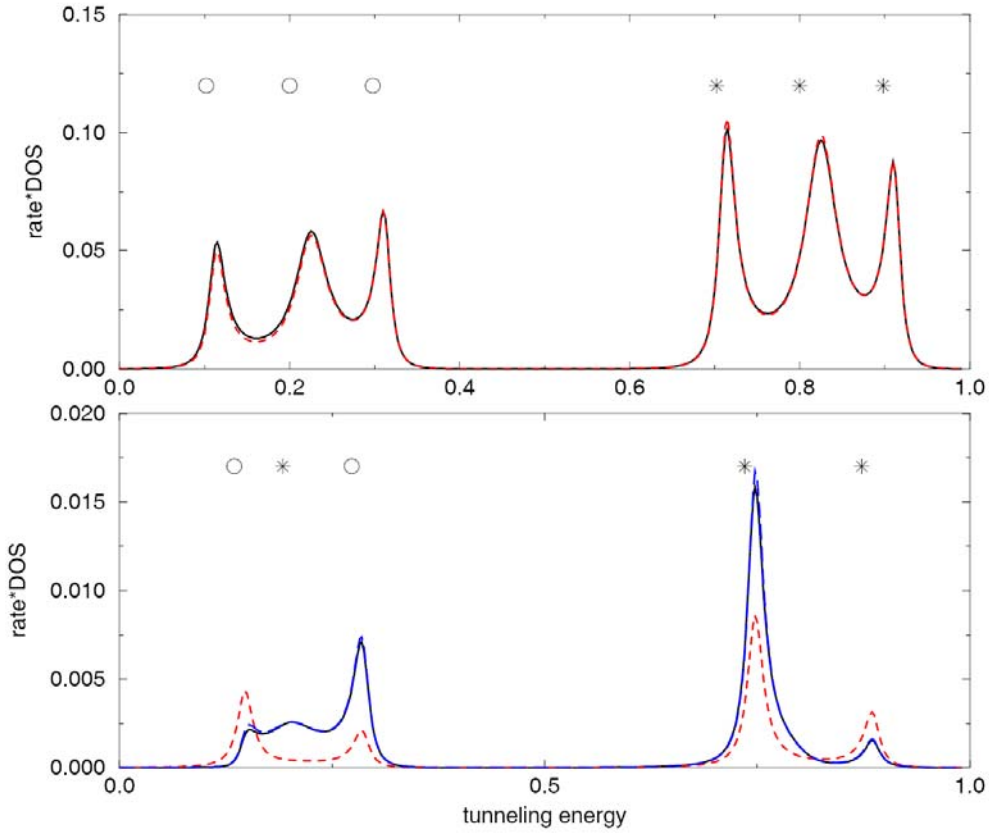

Figure 4-3. Tunneling rates vs electron incident energy are calculated for the two different bridge molecules, each consisting of three atomic states. The top calculations are performed for the bridge with all states having the same energy 0.8 (a. u.). The bridge utilized at the bottom panel has the energy 0.2 of the first state, while other two states have the same energy of 0.8. The solid black line represents the exact result, the dashed blue line depicts ICA0 result and the blue long-dashed line shows ICA1 result and practically coincides with the black line.

We plot the exact tunneling rate dependence vs. incident energy of the electron by the solid black line, the result of ICA0 approximation is plotted by a red dashed line. In the top panel the ICA0 and exact results are very close to each other, hence we can explain the tunneling spectrum by using only ICA0 diagrams. The left-most three peaks are the result of the dominant contribution of the following tunneling pathway: the electron "hops" from the left electrode to the first site of the bridge accompanied by the absorption of one photon, then it tunnels through the bridge and hop to the right electrode states. Positions of the peaks approximately correspond to the eigenenergies of the appropriate $k_b = -1$ bridge replica. The right-most three peaks can be

attributed to a pathway involving the electrons tunneling from left electrode zero replica to the bridge replica $k_b = 0$ and thus do not involve photon absorption-emission during the hop from the left electrode to the bridge. The good agreement between the ICA0 and the exact calculations is the result of the weak laser field strength and the specific structure of the bridge. The eigenenergies for the different bridge replicas (shown by stars for $k_b = 0$ and circles for $k_b = -1$) are well separated from each other, with the result that the tunneling pathways involving the (photon assisted) transitions between the Floquet bridge states corresponding to different replicas (and described by higher then zero order perturbation terms) are relatively unimportant.

The structure of the bridge molecule used in calculations at the bottom and top panel is very similar, except that the second bridge molecule has the energy of the first state changed to the 0.2 value. As a consequence, the eigenergies of the different bridge replicas overlap resulting in larger contributions of inter-replica pathways. The ICA0 curve (red dashed curve) is no longer in good agreement with exact result. Including the pathways involving one-photon transitions between the bridge replicas by using the ICA1 approximation (blue curve) improves the agreement with the exact result. The following ICA1 specific pathway dominates for the electrons with tunneling energies near $0-0.4$: the electron tunnels from the left electrode to the first bridge site, then absorbs one photon and hop to the second bridge state and then tunnel through to the right electrode. The dominating ICA1 pathway for the electrons starting in the range of energies $0.6-1$ involves the tunneling from the left electrode to the first bridge site with emission of one photon, then hopping to the second bridge site accompanied by absorption of one photon and then tunneling through to the right electrode. We checked numerically that these resonant ICA1 channels are dominant and provide most contribution into the total rate.

In the method developed in this section, the total driven-tunneling rate is calculated by the standard scattering formula applied to the (time-independent) effective Floquet Hamiltonian and requires calculation of the matrix elements of the full Green function $\mathbf{G}$ corresponding to this Hamiltonian. By using the proposed partitioning, these (effective Floquet) Green function matrix elements can be expressed as a sum of infinite number of terms, where every term consists of multiplication of the 1) coupling inside the bridge 2) Green function matrix elements of the physical bridge Hamiltonian 3) Bessel functions and field parameters. By using the diagrams it is easy to write down all these individual terms in the expansion for the matrix elements of the effective Green function.

These diagrams provide a useful interpretation of the driven electron transfer across a molecular junction. The individual electron tunneling pathway is interpreted as a series of hops between the bridge sites accompanied by photon absorption/emission. The total tunneling rate is the interference of all available pathways. By using the diagrams one can explain why the specific pathways dominate in electron transport, and predict which pathways can be resonantly important for a specific molecular junction system. In favorable cases, by simple inspection of the energy level structure of a molecular wire one can predict the dominant tunneling pathways and provide the corresponding analytical formula of this pathway.

4.4 APPLICATION OF THE FORMALISM TO THE XYLYL-DITHIOL MOLECULE CONNECTING TWO GOLD ELECTRODES.

In Fig. 4.4 we illustrate the accuracy and convergence of the perturbation expansion by calculating the tunneling rates through the realistic molecular wire system consisting of xylyl-dithiol molecule connecting two gold electrodes. The matrix elements (including self-energy) of this molecular wire Hamiltonian were determined in chapter 3. Fig. 4.4(a) represents the case of relatively strong laser field of 2×10^{7} V/cm. The results of ICA0 (short dashed) and ICA2 (long dashed) curves are not in good agreement with the solid curve representing the exact solution, although they capture most of the peaks positions and amplitude. Taking more perturbation expansion terms into consideration does not improve the agreement - the perturbation series thus does not converge for this field strength. For a weaker, but still strong field of 8×10^{6} V/cm the perturbation expansion does converge, and by taking into account two perturbation terms (using ICA2) we obtain almost perfect agreement with the exact result. We checked numerically that for weaker field strengths than the one used in panel (b) the convergence is even better, as expected, because the perturbation becomes smaller for weaker field intensities.

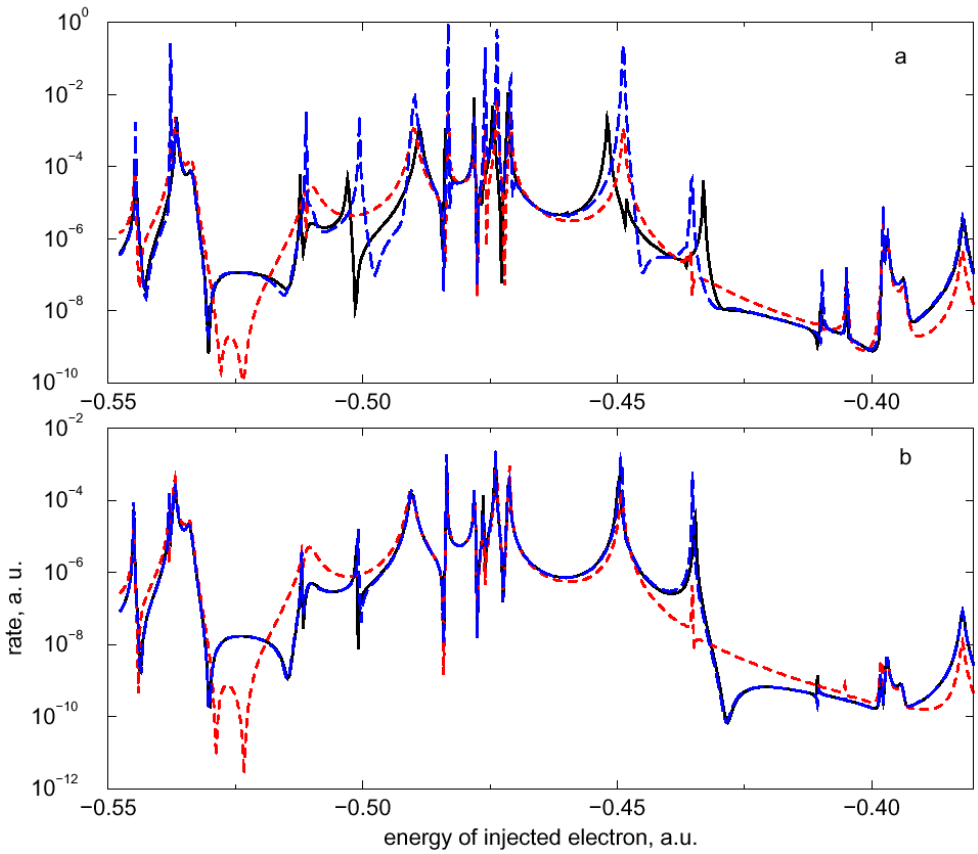

Figure 4-4. Tunneling rate dependence on initial energy of the electron in the L-electrode. The molecular junction consist of the xylyl-dithiol molecule connecting two gold electrodes. The solid black line in both panels shows the exact transition rate, dashed red line shows ICA0 result and the long-dashed blue line shows the ICA2 result. Panel a represents tunneling rates obtained under the strong laser field strength of 2×10^{7} V/cm and panel b represents the lesser, but still strong laser field strength of 8×10^{6} V/cm.

The Fig. 4.4 ICA0 and ICA2 rates were calculated by diagonalizing the matrixes representing several Floquet bridge replicas. This is a numerically straightforward and simple way to estimate the Green's function matrix elements of the full effective Floquet Hamiltonian and the tunneling rates. The perturbative partitioning of the Floquet Hamiltonian reduces the dimensionality of the matrixes that needs to be diagonalized, reducing the numerical time required for calculations.

Based on our calculations for the xylyl-dithiol molecular wire we can explain our specific choice of what part of the total Floquet Hamiltonian to use as a perturbation. The typical distance between the strongly coupled bridge atomic states is about one-two angstroms, resulting of very small values of field parameter a for realistic values of laser field. Thus for small a the effective

coupling between the states of the same replica is multiplied by $J_0(a) \approx 1$, while the effective coupling between the replicas contains the Bessel functions of higher order and thus close to zero. Thus the non-diagonal blocks of Floquet Hamiltonian included in $\mathbf{V}$ contain the matrix elements describing the coupling between the different replicas and thus can be used as a small perturbation (proportional to $J_n(a)$, n=1,2…).

4.5 CONCLUSIONS

In this chapter we partitioned the effective Floquet Hamiltonian for the laser field driven molecular wire and then used perturbation theory to calculate tunneling rates. By partitioning the Floquet Hamiltonian we obtained the analytical expression for the total tunneling rate as a sum of terms representing different tunneling pathways. We suggest the usage of pictorial diagrams to account for all these possible pathways.

Using as an example a simple model of the bridge molecule consisting of three atomic states, we calculated the tunneling rates and explained them in terms of interference of specific resonant pathways, with every pathway interpreted as a "hopping" between the states accompanied by the photons absorption/emission. The use of diagrams helps us to visualize these pathways and understand which of them are important. This understanding may be helpful in design the molecular electronic devices with specific required properties.

We tested the applicability and limits of the perturbative approach for a realistic molecular wire (xylyl-dithiol) and concluded that for a reasonable laser field strength of less then 10^7 *V/cm* the perturbation theory produces numerically accurate results for this system.

BIBLIOGRAPHY

[1] *Introducing Molecular Electronics* edited by G. Cuniberti, G. Fagas, K. Richter, Lecture Notes in Physics, Vol. 680. (Springer-Verlag, Heidelberg, 2005).

[2] A. Nitzan and M. Ratner, Science **300**, 1384 (2003).

[3] D.M. Adams, L. Brus, C.E.D. Chidsey, et al., J.Phys.Chem. B **107**, 6668 (2003).

[4] C. Joachim, New J. Chem. **15**, 223 (1991).

[5] See for example *Atomic and molecular wires*, edited by Christian Joachim and Siegmar Roth, (Dordrecht ; Boston : Kluwer Academic Publishers, 1997).

[6] G. Leatherman, E. N. Durantini, D. Gust, T. A. Moore, A. L. Moore, Z. Zhou, P. Rez, Y. Z. Liu, and S. M. Lindsay, J. Phys. Chem. B **103**, 4006 (1999).

[7] J. Park, A.N. Pasupathy, J.I. Goldsmith, C.C. Chang, Y. Yaish, J.R. Petta, M. Rinkoski, J.P. Sethna, H.D. Abruna, P.L. McEuen, and D.L. Ralph, Nature, **417**, 722 (2002).

[8] W. Liang et. al., Nature **417**, 725 (2002).

[9] Collier, C. P.; Mattersteig, G.; Wong, E. W.; Beverly, K.; Sampaio, J.; Raymo, F. M.; Stoddart, J. F.; Heath, J. R. Science **289**, 1172 (2000).

[10] See for example *Molecular Electronics*, edited by M. A. Ratner and J. Jortner (Butterworth, 1997).

[11] M. A. Reed, C. Zhou, C. J. Muller, T. P. Burgin, and J. M. Tour, Science **278**, 252 (1997).

[12] S. Datta, *Electronic Transport in Mesoscopic Systems* (Cambridge University Press, Cambridge, 1995).

[13] B. J. Keay, S. Zeuner, S. J. Allen, Jr., K. D. Maranowski, A. C. Gossard, U. Bhattacharya and M. J. W. Rodwell, Phys. Rev. Lett. **75**, 4102 (1995).

[14] X.-Y Zhu, J. Phys. Chem. B **108**, 8778 (2004).

[15] X.-Y Zhu, Surface Science Report **56**, 1 (2004).

[16] D.M. Adams, L. Brus, C.E.D. Chidsey, et al., J.Phys.Chem. B **107**, 6668 (2003).

[17] J. Tersoff, and D.R. Hamann, Phys. Rev. B, **31**, 805 (1985).

[18] V. Mujica, M. Kemp and M. A. Ratner, J. Chem. Phys. **101**, 6849 (1994); ibid. **101**, 6856 (1994).

[19] M. P. Samanta, W. Tian, S. Datta, J. I. Henderson and C. P. Kubiak, Phys. Rev. B **53**, R7626 (1996).

[20] W. Tian, S. Datta, S. Hong, R. Reifenberger, J. I. Henderson and C. P. Kubiak, J. Chem. Phys. **109**, 2874 (1998).

[21] S. Datta, W. Tian, S. Hong, R. Reifenberger, J. I. Henderson and C. P. Kubiak, Phys. Rev. Lett. **79**, 2530 (1997).

[22] C. Joachim and J. Vinuesa, Europhys. Lett., **33**, 635 (1996).

[23] N. D. Lang, Phys. Rev. B **52**, 5335 (1995).

[24] M. Di Ventra, S. T. Pantelides and N. D. Lang, Phys. Rev. Lett. **84**, 979 (2000).

[25] M. Di Ventra, N. D. Lang, Phys. Rev. B **65**, 045402 (2002).

[26] Y. Xue, S. Datta, M. A. Ratner, Chem. Phys. **281**, 151 (2002).

[27] P. Damle, A. W. Ghosh, S. Datta, Chem. Phys. **281**, 171 (2002).

[28] A. Nitzan, Ann. Rev. Phys. Chem. **52**, 681 (2001).

[29] D. Segal, A. Nitzan, W.B. Davis, M.R. Wasilewski, and M.A. Ratner, J. Phys. Chem. B, **104**, 3817 (2000).

[30] Y. A. Berlin, G. R. Hutchison, P. Rempala, M. A. Ratner, J. Michl, J. Phys. Chem. A **107**, 3970 (2003).

[31] Y. Xue, S. Datta, and M.A. Ratner, J. Chem. Phys., **115**, 4292 (2001).

[32] M. Brandbyge, J. Mozos, P. Ordejón, J. Taylor, and K. Stokbro., Phys.Rev. B **65**, 165401 (2002).

[33] M.Galperin, A.Nitzan, M.A.Ratner, Phys.Rev. B **73**, 045314 (2006).

[34] Y. Dakhnovskii and R. Coalson, J. Chem. Phys. **103**, 2908 (1995);

[35] D.G. Evans, R.D. Coalson, H.J. Kim and Y. Dakhnovskii, Phys. Rev. Lett. **75**, 3649 (1995).

[36] I.A. Goychuk, E.G. Petrov and V. May, Chem. Phys. Lett. **353**, 428 (1996).

[37] Y. Dakhnovskii and H. Metiu, Phys. Rev. B **51**, 4193 (1995).

[38] M. Henseler, T. Dittrich, K. Richter, Phys. Rev. E **64**, 046218 (2001).

[39] W. Li, L.E. Reichl, Phys. Rev. B **60,** 15732 (1999).

[40] D.J. Thouless, Phys. Rev. B **27**, 6083 (1983).

[41] B.L. Altshuler, L.I. Glazman, Science **283**, 1864 (1999).

[42] M. Shapiro and P. Brumer, Principles of the Quantum Control of Molecular Processes (Wiley, New York, 2003).

[43] M. J. Hagmann, Appl. Phys. Lett. **66**, 789 (1995); M. J. Hagmann, J. Vac. Sci. Technol. B **14**, 838 (1996).

[44] S. Kohler, J. Lehmann, and P. Hänggi, Phys. Rep. **406**, 379 (2005).

[45] R.H. Blick, R.J. Haug, J. Weis, D. Pfannkuche, K. von Klitzing, K. Eberl, Phys. Rev. B **53,** 7899, (1996).

[46] W.G. van der Wiel, S. De Franceschi, J.M. Elzerman, T. Fujisawa, S. Tarucha, L.P. Kouwenhoven, Rev. Mod. Phys. 75 (2003).

[47] A. Thon, M. Merschdorf, W. Pfeiffer, T. Klamroth, P. Saalfrank and D. Diesing, Appl. Phys. A. **78**, 189 (2004).

[48] K. Lance Kelly, Eduardo Coronado, Lin Lin Zhao, and George C. Schatz, J. Phys. Chem. B **107**, 668 (2003).

[49] L. F. Juarez Da Silva, C. Stampfl and M. Scheffler, Phys. Rev. B. **72**, 075424 (2005).

[50] K. A. Pronin, P. Reineker and A. D. Bandrauk, Phys. Rev. B **71**, 195311 (2005).

[51] V.M. Akulin, N.V. Karlov, *Intense resonant interactions in quantum electronics* (Berlin ; New York : Springer-Verlag, 1992).

[52] S-I. Chu, in *Lasers, Molecules, and Methods* edited by Joseph O. Hirschfelder, Robert E. Wyatt and Rob D. Coalson, (Vol. LXXIII in the Willey Series on Advances in Chemical Physics, 1989).

[53] R. P. Andres, T. Bein, M. Dorogi, S. Feng, J. I. Henderson, C. P. Kubiak, W. Mahoney, R. G. Osifchin, and R. Reifenberger, Science **272**, 1323 (1996).

[54] M. Olson, Y. Mao, T. Windus, M. Kemp, M. Ratner, N. Leon and V. Mujica, J. Phys. Chem. B, **102**, 941 (1998).

[55] Eldon G. Emberly and George Kirczenow, Phys. Rev. B **58**, 10911 (1998).

[56] A. Tikhonov, R. D. Coalson, Y. Dahnovsky, J. Chem. Phys. **117,** 567 (2002).

[57] A. Tikhonov, R. D. Coalson, Y. Dahnovsky, J. Chem. Phys. **116**, 10909 (2002).

[58] A. Keller, O. Atabek, M. Ratner, V. Mujica, J. Phys. B **35**, 4981 (2002).

[59] I. Urdaneta, A. Keller, O. Atabek, V. Mujica, Int. J. Quantum Chem. **99**, 460 (2004).

[60] S. Kohler, J. Lehmann, S. Camalet, P. Hänggi, Israel J. Chem. **42**, 135 (2002).

[61] S. Kohler, J. Lehmann, M. Strass, P. Hänggi, Adv. Solid State Phys. **44**, 157 (2004).

[62] See, for example, S. Mukamel, *Principles of Nonlinear Spectroscopy* (Oxford Univ. Press, Oxford, 1995).

[63] Eq. (2.12) and the formulae for electron current in Sect. 2.1 were previously obtained in Refs. [18-21].

[64] Real metals are, of course, not perfect conductors; see, for example, F. Wooten, *Optical Properties of Solids* (Academic Press, NY, 1972). The effect of this departure from ideality remains to be investigated.

[65] To see that $a_{\alpha\beta}$ is actually dimensionless, it is useful to restore $\hbar$: "$E_0(\mu_\alpha - \mu_\beta)/\hbar\omega$".

[66] Although the main purpose of these model calculations is to illustrate basic principles of *ac*-field driven electron transport through molecular wires, we should bear in mind the relevant frequency regime in real systems, which is given approximately by the energy difference between the Fermi level of the electrode and the highest occupied or lowest unoccupied molecular orbital of the bridge molecule, i.e., typically on the order of electron volts [2].

[67] Note that in order to keep the a parameters fixed while varying the frequency, we must increase the laser field strength E_0 proportionally to ω so that the ratio E_0/ω remains constant.

[68] V. Mujica, A. Roitberg and M. Ratner, J. Chem. Phys. **112**, 6834 (2000).

[69] V. Mujica, M. Kemp, A. Roitberg and M. Ratner, J. Chem. Phys. **104**, 7296 (1996).

[70] In fact, if the site basis vectors $|I>$ are associated with atomic orbitals of the bridge molecule, this condition is not strictly fulfilled. However, as will be shown in Sect. 3.1.3, it is straightforward to replace the atomic orbital basis with a slightly modified, strictly orthogonal site basis.

[71] S. Y. Hong and J. M. Song, J. Chem. Phys. **107**, 10607 (1997).

[72] R. Hoffmann, J. Chem. Phys. **39**, 1397 (1963); John P. Lowe, *Quantum chemistry*, (Boston : Academic Press, 1993).

[73] GAUSSIAN 94, Revision D.4, M. J. Frisch, G. W. Trucks, H. B. Schlegel, P. M. W. Gill, B. G. Johnson, M. A. Robb, J. R. Cheeseman, T. Keith, G. A. Petersson, J. A. Montgomery, K. Raghavachari, M. A. Al-Laham, V. G. Zakrzewski, J. V. Ortiz, J. B. Foresman, J. Cioslowski, B. B. Stefanov, A. Nanayakkara, M. Challacombe, C. Y. Peng, P. Y. Ayala, W. Chen, M. W. Wong, J. L. Andres, E. S. Replogle, R. Gomperts, R. L. Martin, D. J. Fox, J. S. Binkley, D. J. Defrees, J. Baker, J. P. Stewart, M. Head-Gordon, C. Gonzalez, and J. A. Pople (Gaussian, Inc., Pittsburgh PA, 1995).

[74] I.V. Kurnikov and D.N. Beratan, J. Chem. Phys. **105**, 9561 (1996).

[75] M.J. Shephard, M.N. Paddon-Row, and K.D. Jordan, Chem. Phys. **176**, 289 (1993).

[76] R. B. Ross, J. M. Powers, T. Atashroo, W. C. Ermler, L. A. LaJohn and P. A. Christiansen, J. Chem. Phys. **93**, 6654 (1990).

[77] D.A. Papaconstantopoulos, *Handbook of the Band Structure of Elemental Solids*, (Plenum Press, New York, 1986).

[78] R. Wiesendanger, *Scanning probe microscopy and spectroscopy : methods and applications*, (Cambridge, England ; New York : Cambridge University Press, 1994).

[79] For this and subsequent calculations in which a nonzero value of the *dc* bias voltage is employed, we assume that the voltage drop is distributed linearly across the junction. Site energies of the bridge orbitals are shifted accordingly (cf. Eq. (3.1)) for each *dc* voltage considered.

[80] Y. Kawata, C. Xu, W. Denk, J. Appl. Phys. **85**, 1294 (1999).

[81] W.B. Davis, M.R. Wasielewski, M.A. Ratner, V. Mujica, and A. Nitzan, J. Phys. Chem. A **101**, 6158 (1997).

[82] A. Liebsch, *Electronic Excitations at Metal Surfaces*, (Plenum Press, New York, 1997).

Part 2.

Light Diffraction by Colloidal Crystals – Numerical Simulations for Realistic Finite Systems Using Single Scattering Theory.

Chapter 5. Introduction.

5.1 PHOTONIC CRYSTALS AND THEIR APPLICATIONS. THE SEARCH FOR THE FULL PHOTONIC BAND-GAP MATERIALS.

Propagation of waves through a medium containing a periodically or almost periodically arranged collection of scatterers is a very popular motif arising in different branches of physics. There is a deep analogy between the propagation of electrons through an atomic lattice, diffraction of X-rays from atomic lattices and propagation of light through a medium with dielectric constant periodically modulated on a scale smaller then the wavelength of light. The last research field, often referred to in this context "nanophotonics", has recently experienced explosive development. Its beginning is often associated with the proposal of E. Yablonovich to use photonic bandgap (PBG) materials to inhibit the spontaneous emission [1] and the idea by S. John to use modulated dielectric media for coherent localization of photons [2].

PBG materials, or "photonic crystals", are dielectric periodic structures designed to form energy band gaps for photons, which allow or prohibit the propagation of electromagnetic waves in certain ranges of frequencies and directions [3]. Similar to electrons in a periodic potential, the electromagnetic field in a periodic dielectric media can be expressed as a superposition of Bloch waves, where each Bloch wave form a separate solution for the master wave equation derived from Maxwell equations. The dispersion relationships for these waves form the structure of bands, specifying allowed frequencies for every Bloch wave direction. The band structure for the

photons arises from finding the Bloch type solution for Maxwell equations, which can be used to derive the master wave equation for the electric field vector $\vec{E}^{\omega}$ in CI units as [3]:

$$\vec{\nabla} \times \vec{\nabla} \times \vec{E}^{\omega}(\vec{r}) = \frac{\omega^2}{c^2} \varepsilon(\vec{r}) \vec{E}^{\omega}(\vec{r})$$

where ε is the dielectric function specifying the material properties of the medium, ω is the frequency and c is the velocity of light in the vacuum. This equation was obtained from the assumption that the magnetic permeability is unity everywhere, and the dielectric function ε is a local and linear function. Note that there is no time dependence in the equation, since it was obtained by Fourier transformation of the Maxwell equations from time to frequency domain. $\vec{E}^{\omega}$ is the Fourier component of the full time-dependent electromagnetic field corresponding to the frequency ω. Another assumption we invoke here is that the dielectric function is frequency independent. This assumption is valid for many dielectric structures in the visible and infra-red frequency ranges, but cannot be used for metals or for dielectrics having resonant interaction of light near the frequencies under consideration.

Since its inception, research in nanophotonics has focused heavily on design, manufacturing and characterization of complete PBG materials, i.e., possessing an omnidirectional band gap in some frequency range. This forbidden gap has no propagating Bloch states over this range, and PBG materials can exhibit novel optical properties. Besides the already mentioned inhibition of spontaneous emission, these materials can lead to a confinement and molding of light in engineered waveguides channels and cavities. Development of photonic materials enabling generation, localization, amplification and processing of light is central for creation of new devices for information and communication technologies [4]. The ability to manage photons similar to the way in which semiconductors manipulate electrons could lead to the creation of a photonic chip [5]. A photonic crystal with a complete PBG located around 1.55 mm – the wavelength region important for optical communications, was successfully produced [6, 7]. Many other materials, possessing a complete PBG in the infrared, microwave and visible regions were experimentally developed [8-12].

The development of complete PBG materials proved to be a challenging task, since it depends delicately on the symmetry of the crystal lattice, shape and type of the structural unit and the magnitude of the dielectric contrast. Scalar waves, such as electronic wavefunctions or sound waves, can readily form a complete PBG for such a simple structure as an fcc lattice of

spherical scatterers [13]. But the vector nature of electromagnetic radiation leads to more restrictive conditions. For the fcc lattice of spherical scatterers, exhaustive band structure calculations showed that this system does not posses a complete bandgap, but only a number of pseudo gaps. This pseudo gaps have bandgaps that exist for only a certain range of propagation directions. The existence of a complete PBG in such a system is inhibited primarily by symmetry-related band degeneracy near the W and U points, and this degeneracy is impossible to eliminate by increasing the dielectric constant or changing the volume fraction occupied by the particles [14].

But for the inverted system, the so called "inverse opals" which are prepared by filling the media between the spheres with higher dielectric constant materials, it is possible to lift this degeneracy and create the complete PBG. It was shown that for the closed-packed fcc inverted system the minimum dielectric contrast of approximately 2.8 is required for a complete PBG (between the 8^{th} an 9^{th} bands) [15]. In general the existence and characteristics of complete PBG depends on many factors, and for an inverted opal structure one can optimize the dielectric contrast, the volume fraction ratio between two different dielectric materials, and the geometrical shape of the lattice structural unit. It was found, that the sintering procedure increases the width of the complete stop band. But the nature and dependencies of the factors affecting the existence of complete PBG are not clearly established. Typically, separate band structure calculations are performed for each specific photonic crystal structure, and then the results of calculations are organized into "maps" showing the location and the width of PBG for different parameters. These maps of complete PBGs were obtained in [16] for different fcc space groups as a function of volume fraction of air spheres in an inverted structure.

Another approach toward the complete PBG proposes to reduce the symmetry of the 3D lattice from the fcc to the diamond structure. In this case, a complete gap forms between the 2^{nd} and the 3^{rd} bands. An inverse diamond lattice of overlapping air spheres in a high refractive index material exhibits a much larger gap [17]. Unfortunately, to the best of my knowledge, it has been impossible to fabricate the diamond type structure by utilizing spherical particles. In the microwave regime, the diamond symmetry structures were successfully manufactured by drilling cylindrical holes in a bulk dielectric material with a refractive index of 3.5, and the bandgap width to center frequency ratios as large as 20% were demonstrated [18].

Unlike the case of an fcc lattice of spherical particles immersed in the media of lower dielectric contrast, it is possible to obtain the complete PBG in the fcc lattice of non-spherical scatterers. The examples of such individual scatterers include the dimer, consisting of two interconnecting spheres [19], and the peanut shaped particles [20]. Besides the fcc and diamond lattices, other types of lattices can be used in photonic crystals. The calculations showed that the body centered type lattice as well as simple cubic lattice structure could exhibit large photonic omnidirectional band gap [21].

Although the search for theoretical characterizations and experimental manufacturing of photonic crystals with a complete PBG is important motif of the nanophotonics, there are many practical applications requiring less then complete PBG's. Some of these applications include creation of novel optical switches and filters, chemical sensors, optical fibers and other optical devices [22-25].

The evolution of photonics will depend on the development of new photonic crystal materials. Driven by the needs of applications in telecommunications and optoelectronics, computing, manufacturing of novel coatings, etc, recently there has been considerable progress in fabrication of photonic crystals. Fabrication of 1D and 2D photonic crystals is relatively straightforward and therefore these materials are widely used in many commercial devices. 1D systems can be easily manufactured by the deposition of alternating layers of different dielectric materials [26], while 2D systems can be produced by a variety of techniques, for example by selective etching of the substrate through the masks [27]. However, the efficient, large scale fabrication of the 3D photonics crystals remains a major materials science challenge.

To obtain photonic band gap materials, it is necessary to create periodic ensembles of scatterers with lattice parameters that are roughly half the relevant wavelength of light. There are several competing technologies to manufacture photonic crystals, including the sequential method of layer by layer microlithography [28], photoelectrochemical etching [29] and holographic lithography [30].

Another class of methods is based on the self-organization of a large group of individual particles, typically a spherical colloidal particles organized in a colloidal crystal array (CCA). A CCA is comprised of a periodic arrays of colloidal particles immersed in a dielectric medium. Various methods have been developed to fabricate photonic crystals by utilizing close-packing of spherical colloidal particles and creating artificial opals [31-33]. To fabricate opals, the spheres

are usually sequentially sedimented by gravitational or capillary force to create ordered arrangements of particles. In these structures the long range ordering is limited by the standard deviation in the size and shape of the constituent colloidal particles as well as limitations of self-organizing packing processes. The search for materials with a complete PBG fueled the study of the inverse opals, where the gaps between the closed packed colloidal particles are infiltrated by a high refractive index material, with the subsequent particles removed by etching leaving behind the spherical voids [34-35].

An alternative approach to the closed-packed system are CCA's where the colloidal particles self-assemble into the crystal structure in a low ionic strength aqueous solution [36, 37]. This procedure involves self-organization of previously negatively charged particles, which electrostatically repel each other to adopt a minimum energy configuration, typically with the fcc lattice structure. By altering the concentration of colloidal particles in the solution it is possible to manufacture CCA's with a desired lattice constant not restricted to closed packed systems.

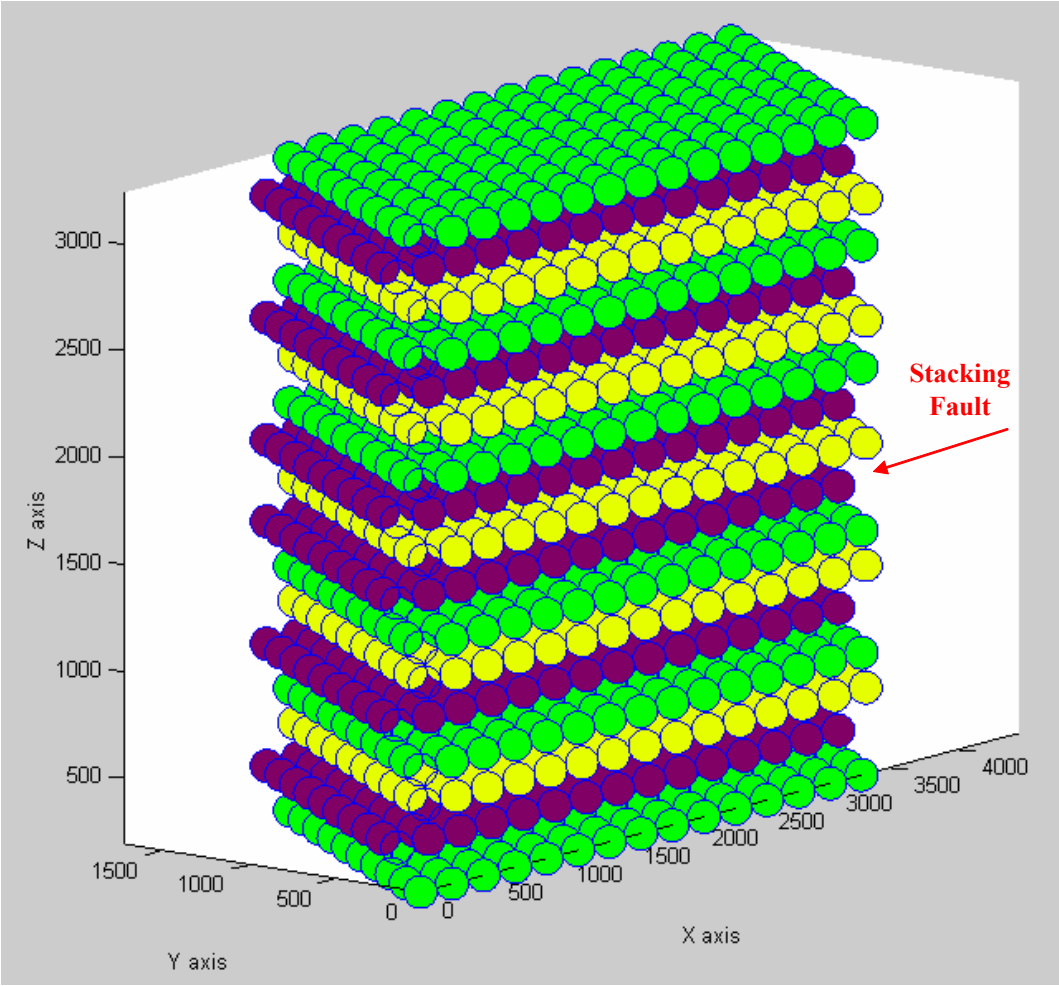

Figure 5-1 FCC colloidal crystal array, consisting of the (111) planes stacked together in according to the …ABCABC… order. A, B, C layers are shown in different colors. The location of the stacking fault is shown by the arrow.

Colloidal crystals obtained by this latter self-assembly method predominantly form an fcc type of lattice with the (111) planes oriented along the surface of the confining container (Fig. 5-1). The resulting (111) layered structure consists of alternating layers of three types - ..ABCABC.., shown in Fig. 5-1 in different colors. The change in layer ordering leads to a very common type of defect – namely, the stacking fault defect, shown in the figure by the arrow. Other defects typical for these structures come from the variations of colloidal particles sizes and shapes and locations in the crystal lattice.

The main purpose of this work is to develop a numerical tool to analyze a scattering of light by finite CCA, consisting of many (10^6-10^8) particles. Driven by practical experimental needs, we aimed to numerically simulate the full 3D map of light intensities scattered by a realistically macroscopic CCA. We don't restrict the incident light to be a plane wave, and the distribution of particles inside the CCA to be periodic.

5.2 THEORETICAL APPROACHES AND METHODS FOR CALCULATING DIFFRACTION OF LIGHT FROM FINITE ASSEMBLIES OF SCATTERERS.

There are many theoretical approaches to calculate interaction of light with photonic crystals. Methods derived from different areas of physics have found their applications in this field. Band structure theory, originally developed for electrons in an infinite periodic potential, was used to solve the vector Maxwell equations in periodic dielectric media [38, 39, 3]. Band gap theory is most often implemented via the plane wave expansion method, where the optical field Bloch solution for the wave equation (1) is expanded in many, typically hundreds of plane waves. Dispersion relations obtained for the Bloch waves were plotted as band structure diagrams and analyzed using standard concepts of band gap theory. When the frequency of light lies inside the

band gap, the dispersion relation $\omega(k)$ has no solutions for real k, thus no propagating wave solutions. But the solutions with the non-zero imaginary part k still exist inside the gap and correspond to the exponentially decaying Bloch waves. The total (complex) band structure of photonic crystals can be used to derive the boundary conditions for the electromagnetic field at the interface. Then the reflectance and transmission properties for a finite crystal can be calculated by matching the light fields inside and outside of the crystal through the boundary conditions [40, 41]. The disadvantage of this Fourier based method is that it requires many plane waves to expand the dielectric constant of spherically symmetric particles. This method calculates the $\omega(k)$ and not $k(\omega)$, and is not well suited for a transmission and reflection calculations at a fixed frequency, since it requires the calculation of full dispersion $\omega(k)$ for all frequencies.

A more efficient (and also more widely used) method for calculating diffraction and transmission properties is based on relating the electromagnetic field components at the opposite sides of a thin slab of dielectric material through a so-called transfer matrix [42-44]. This is done by dividing the space in each slab into parallelepiped cells with a coupling between these cells. Then the whole system is represented as a stack of slabs by using the multiple scattering formula familiar in the theory of low-energy diffraction [42]. This method belongs to the category of the so called on-shell methods, since it calculates $k(\omega)$ in contrast to the $\omega(k)$ calculated in the plane wave expansion method. It is sufficient to calculate all possible Bloch waves for only one frequency ω, and then obtain transmission and diffraction coefficients. The transfer matrix method is essentially a real-space finite-element method of computational electrodynamics, adopted for a system with a periodic dielectric function. The numerical solution for this system is a time-consuming process, and the disadvantage of the method is that it is restricted to the systems built from slabs infinite in lateral dimension. Recently, within the general framework of transfer matrix method, in addition to the real space implementation, different types of basis functions were used to represent electromagnetic fields, including Rayleigh multipoles and plane-waves [45, 46].

In the special case of dielectric spheres periodically arranged inside infinite slabs the layer-multiple-scattering method was developed [47, 48]. In this method spherical vector basis functions were used to expand the electromagnetic field around each particle, and these fields were summed for periodically spaced spherical scatterers in an infinite slab. Transfer matrices

were then utilized to couple fields between the different slabs. Recent extension of the method enables application to nonspherical particles, with scattering properties of individual particles calculated through the evaluation of the T-matrix [49]. All of these approaches include multiple scattering processes inside the crystal into the theoretical and numerical framework, but require either periodicity of the system or infinite extent in some dimension.

The idea to use localized Wannier-like functions constructed from the Bloch states was used to calculate the defect states of photonic crystals [50, 51]. The approximate perturbative behavior of electromagnetic wavepackets was obtained in the envelope-function approximation.

A number of computational electrodynamics techniques were developed to calculate the light scattering properties of arbitrary shaped, non-periodic systems [52, 53, 54]. These include the finite difference time domain method [55], the multiple multipole [56] and the generalized field propagator [57] methods, which have been utilized to calculate transmission and diffraction for photonic crystals containing various non-periodicities and defects. These methods are numerically expensive and are currently able only to treat systems with relatively small number of scattering particles.

There are methods which were developed specifically for systems consisting of arbitrary located spheres, including the T-matrix superposition method [58] and the generalized multisphere-Mie theory [59]. The total field scattered by a collection of spheres is represented as a superposition of individual sphere contributions, where each contribution is expanded in vector spherical harmonics. The multiple scattering between spheres is taken into account by representing the total field incident at each sphere as a sum of the initial incident wave and scattering contributions from every other sphere of the system. To perform the summation the method utilizes the translation addition theorem, where a vector spherical wave centered at one sphere is expressed through the spherical waves centered at other sphere. Currently these methods numerical overload allow the analysis of only small clusters of spheres (hundreds) [60], and cannot simulate realistic CCA's.

Scattering of light by photonic crystals can be understood as the interplay between two different scattering mechanisms. One is the single-particle scattering from individual colloidal particles comprising the CCA. In the case of non-CCA photonic crystals, where the dielectric material is distributed continuously in the volume, one can consider the single unit cell of photonic crystal as a single particle. The typical size of this single particle is about half of the

wavelength or smaller, resulting in possible resonance behavior of the light interacting with the dielectric volume confined inside the specific shape of the particle. Second mechanism is the macroscopic Bragg type interference between the contributions scattered from all particles of the system. In an ideal crystal the particles are periodically arranged, and the scattering of plane waves by the crystal results in a Bragg type diffraction maximums. There is a connection between the band-structure picture and the description utilizing the language of Bragg diffraction. The Bragg law connects the wavevector of incident plane wave $\vec{k}$ and reciprocal wave vector $\vec{G}$ by the relation $\vec{k} \cdot \vec{G} = ½\vec{G}^2$. Thus, the Bragg law states that when the incoming wavevector $\vec{k}$ lies on the surface of the Brillouin zone and the incident light Bragg diffracts, these wavevector values in the band diagram correspond to the opening of a band gap near the reduced zone edge.

The interaction of light with a photonic crystal can be understood as a scattering process, where the total amplitude of scattered light is the result of interference of all scattering contributions from particles of the system. The electromagnetic field incident at every particle, is the superposition of the incident light wave and the secondary waves originating from rescattering by all other particles. In this thesis, we assume the all scattering events are elastic: the wavelength of the light is not changed by the scattering.

The Bragg diffraction description is a simple picture based on a single scattering simplification of the whole scattering process. In a single scattering model, the scattered light results from the interaction of incident light with each scatterer. Secondary waves, arising from light scattered by all other particles are disregarded. Thus, in the single scattering picture we disregard all multiple scattering events, where the incident wave, scattered once by an individual particle, can be scattered again by another particle, as if "bouncing" around between scattering events.

The average distance that light travels between the consecutive scattering events is called the mean free path. Multiple scattering contributions are small when the mean free path is much larger then the size of the whole system. The mean free path depends on how efficient the individual particles scatter, and the smaller this efficiency the larger the mean free path. There are many factors responsible for a magnitude of individual particle scattering efficiency, including the value of the dielectric contrast between inside and outside of the particle, the

particle size and shape, and the direction of scattering. Single scattering is the dominant scattering mechanism for a low contrast dielectric media.

The opposite limit is a strongly scattering medium, where multiple scattering is important. For randomly and strongly scattering media, setting aside the wave nature of light and interference effects, the multiple scattering can be described as a random walk; the light is called diffuse and is described by a diffusion equation [61, 62]. Interference in multiple scattering of light in the random strongly scattering media leads to such interesting effects as the localization of light, speckles, enhanced backscattering and Anderson localization. In a realistic photonic crystal with disorder, where multiple scattering is important, scattering of light results in the interplay between the diffuse and Bragg type scattering [63, 64].

Many theoretical methods briefly described above, such as photonic band structure or transfer matrix derived methods, are focused on the numerical computation of total scattering intensity by solving master wave equation. Their conceptual framework does not distinguish between the single and multiple scattering, or between Bragg interference effects of collections of particles and scattering features of individual particles. Thus, the physical picture as an interplay between these different processes is largely lost, and although the quantitative description is rather accurate, the qualitative picture is unclear. Interpretation and prediction of light interaction with photonic crystals requires a richer conceptual basis describing the physical process involved. The practical theoretical description would benefit from the extensive use of such concepts as single and multiple scattering, Bragg interference and individual particle scattering resonances.

Another group of methods often applied to photonic crystals are focused on the single particle scattering properties, and then total scattering for the collection of particles is obtained in some suitable approximation [52, 65-67]. The shape and material dependent scattering properties of spherical and ellipsoidal particles, core-shell particles and particles built from the dielectric and metallic materials, are significant in the understanding of photonic crystals. The analysis of scattering from collections of particles is mainly based on independent particles approximation, where the particles forming the group can be considered as independent scatterers. This means that the scattering contributions between different particles are considered to be non-coherent, and the intensities of these contributions can be added without the regard to the phase. Multiple scattering in this approach is traditionally taken into account by a so-called radiative transfer

equation. Although the independent particles approximation misses the essential coherent properties of the photonic crystals, it is used in understanding the nature and properties of the diffused light resulting from incoherent scattering by real, disordered crystals.

Interference of light by the periodically arranged collection of weak scatterers is the subject of the methods utilized in the field of X-ray diffraction by solid state crystals [68, 69]. The main emphasis of X-ray diffraction theories is on the collective effects of constructive and destructive interference from collection of scatterers, and less on the properties of single scatterers. The dielectric contrast of the system is very weak, and multiple scattering effects are relatively less important. The light intensity diffracted by an atomic crystal can be calculated in the single scattering approximation and in the X-ray literature this approach is called kinematic theory.

In the regime of very weak dielectric contrast, the result of scattering of a plane wave by a macroscopic ideal crystal consist of predominantly the diffracted wave (or several waves for special incident conditions), directed in Bragg direction. The dynamical diffraction theory (DDT) [68, 69], often used to calculate the intensities of diffracted X-ray light, assumes that the self-consistent electromagnetic field inside a crystal can be represented as a superposition of just two (can be easily generalized to several) plane waves: propagating and diffracted. The propagating $\vec{k}_0$ and diffracted $\vec{k}_G$ wavevectors are connected through the Bragg law $\vec{k}_G = \vec{k}_0 + \vec{G}$. Taking into the account some of the multiple scattering in the form of allowing coupling between the diffracted and propagating waves, the equations of DDT can be derived. The DDT equations result from solving Maxwell equations for a periodic dielectric function under the assumption that inside the crystal the electromagnetic field can be represented as a sum of propagating and diffracted plane waves. Superposition of these two waves form Bloch solution for the wave equation and from this observation follows the connection with the band gap theory. In the band structure calculations, based on the plane wave expansion, each Bloch wave $\vec{E}^k(\vec{r})$ is expanded in the infinite series of plane waves

$$\vec{E}^k(\vec{r}) = \sum_G \vec{E}_G \exp(i(\vec{k} + \vec{G}) \cdot \vec{r})$$

The DDT retains only two plane waves from this expansion, neglecting other terms. Then the total field inside the crystal is represented as a sum of just two Bloch waves, and transmission

and reflection coefficients are obtained by matching the field outside and inside the crystal on the crystal boundary.

The DDT was applied to the photonic crystals in special case, when the incident direction is tuned to Bragg diffract light from the specific crystal planes. The light diffracted by this crystal planes dominates and approximated by a plane wave in the framework of DDT. The DDT theory was applied to model the photonic crystal experimental transmission spectra [70, 71], and it was shown that Applicability of DDT is restricted to systems with weak dielectric contrast [72].

At first glance the DDT seems to be a better theory then the kinematic theory, since it takes into account the coupling between the incident and diffracted waves. But the kinematic theory does not assume that total scattered light consist of a single plane wave, thus it provides a more complex description of the scattered light as distributed over all space directions. Also, the kinematic theory can be used for an arbitrary distribution of scattering particles, not just the ideal fully periodic crystals to which DDT theory is restricted.

5.3 SINGLE SCATTERING APPROACH. KINEMATIC THEORY AND ITS EXTENSIONS.

All existing theoretical methods which take into account multiple scattering effects, are not suitable for the analysis of finite, realistic, macroscopic non-ideal CCA. Exact methods require large amount of computational time, and only relatively small systems can be analyzed. Other methods require either periodicity or some simplification of the scattering process. We chose to utilize a single scattering method based on kinematic theory for several reasons. First, it can be applied to the macroscopic finite CCA characterized by arbitrary locations of spherical particles in a medium and arbitrary illuminating incident beam. Second, it allows calculating scattered intensities for all 3D directions. Third, the scattering results can be interpreted though an interplay of individual particle scattering and collective Bragg type interference.

Even when the system can be analyzed by other, more accurate multiple scattering method, application of the single scattering approach can be used to provide better understanding of physical processes and in particular the importance of multiple scattering by comparing with multiple scattering methods, and can be used as a benchmark and limiting case for more exact methods.

The kinematic theory is based on two approximations:

1) Single-scattering approximation, where the total diffracted light consists of interference between incident plane wave scattered by all individual particles. This approach disregards multiple scattering.

2) Neglecting extinction of the incident wave - all particles in the system are illuminated by an incident wave field of constant amplitude.

An obvious flaw in the standard kinematic theory ("KNM" theory) is the assumption of a constant electric field amplitude of incident light propagating through the CCA crystal. This results in an unrealistically large value of the diffracted intensity for geometrically large CCA's. We modified the kinematic theory to take into account extinction by considering attenuation of incident wave, and call it the "extended kinematic" ("EXKNM") theory. The incident plane wave, after entering the crystal, gradually decays while transferring the energy into the scattered light.

This simple method is applicable for relatively low-contrast systems where multiple scattering effects are small. It represents the diffraction of light from a system of periodically spaced scatterers in terms of the interplay between the resonances of individual particles and Bragg type interference.

A similar method based on KNM theory was previously used [73] to analyze light diffraction by a system of stacked together infinite slabs. The main difference between that method and ours is that we treat arbitrary shaped finite 3D systems and take into account attenuation of the incident light.

In a recent paper [74] we applied our method to examine the differences in integrated intensities of light diffracted by different crystal planes of a CCA. We also applied the method to investigate the influence of stacking faults on the scattering. In this thesis we provide the details of the method, and test its validity. We examine the importance of multiple scattering by

constructing an effective 1D system consisting of many dielectric slabs and analyzing diffraction from the stack of (111) layers of an ideal fcc CCA.

In Section 6.1 we briefly describe how to apply the kinematic method to calculate and interpret the scattering intensities from a finite perfectly ordered CCA. The extended kinematic theory is also presented. In Section 6.2 an effective 1D slab system was constructed and used to examine the importance of multiple scattering.

Section 6.3 explores how the integrated intensity of specific Bragg peak derives from the contribution of several different factors. We discuss some applications of the method to finite CCA's of different shapes and sizes. The dependence of diffracted intensities on the incident angle was analyzed near the Bragg diffraction maximum for several different crystal planes. We also studied the effect of the incident finite beam shape and crossectional profile on the CCA diffraction. Effective penetration depth for the incident light was calculated and compared for several incident directions, three CCA's with different volume fraction were studied.

In Chapter 7 we use single scattering methodology to analyze stacking faults in CCA's.

Chapter 6. Numerical Simulations for the Diffraction by CCA Using Single Scattering theory.

6.1 METHODS – KINEMATIC THEORY AND ITS EXTENSION.

When light illuminates a collection of scattering particles the overall amplitude of scattered light at any point in space is simply the sum of contributions from individual particles. In a single scattering approximation, we ignore multiple scattering between the particles by assuming that each particle is excited by only the external incident field, but not by the secondary fields scattered by other particles. Assuming the external incident light wave to be a plane monochromatic wave, the total scattered amplitude $\vec{E}_{sc}$ at some distant point $\vec{r}$ in the far-field approximation is

$$\vec{E}_{sc}(\vec{r}) = \sum_j \vec{E}_j(\vec{r}) = \sum_j A_j \vec{F}_j(\vec{r}) \exp(i\vec{\rho}_j \overrightarrow{\Delta k}) \tag{6.1}$$

where $\vec{E}_j$ is the amplitude of light at $\vec{r}$ scattered from individual particle *j* with coordinates $\vec{\rho}_j$, and the summation is performed over all particles of the system. We can express every individual contribution as a product of the absolute value of the electric field amplitude of the incident propagating wave A_j, a single sphere scattering form factor $\vec{F}_j(\vec{r})$ and phase factor $\exp(i\vec{\rho}_j \overrightarrow{\Delta k})$, where $\overrightarrow{\Delta k}$ is the difference between the wave vectors of the incident and scattered light. We assume our colloidal particles to be spheres of uniform dielectric constant embedded in a medium of another dielectric constant. We can calculate the form factor $\vec{F}_j(\vec{r})$ exactly from Mie Theory for scattering of a plane wave by a spherical particle [56].

In standard kinematic (KNM) theory the amplitude of the incident propagating wave is constant along the propagation direction in a media, $A_j = const$, and does not decay while

propagating through the crystal. This approximation assumes that the amplitude of the diffracted light is much smaller then that of the incident light.

In our EXKNM approach we assume that the CCA medium can be represented as a stack of layers with the amplitude of the incident propagating wave constant along each layer, but gradually attenuating while propagating. We determine the internal propagating wave amplitude by subtracting from the initial incident light the amount of light diffracted. Specifically, we calculate the amplitude of the light which propagates forward from the condition that the intensity of light after *n* layers equals the intensity of incident light minus the intensity of light scattered by all previous *n* layers. We determine amplitude A_{n+1} after layer *n* from the condition $|A_{n+1}|^2 = |A_0|^2 - |R_n|^2$ where A_0 is the amplitude of the incident wave before entering the CCA, and R_n is the effective amplitude of light diffracted by all layers from *1* through *n*. We calculate R_n by calculating the integrated intensity of all light scattered by the first *n* layers, then determine R_n as the square root of this integrated intensity. We assume that the incident wave is completely attenuated with all energy transferred to the diffracted light when R_n exceeds A_0 after layer $n=N_{eff}$. The effective number of layers, N_{eff} determines the penetration depth available for the incident light. When this number is larger then the actual number of layers in CCA sample, then some of the light is transmitted through the CCA, otherwise all incident light decays inside the sample over the effective number of layers N_{eff}.

The calculation procedure assumes that the CCA is a finite crystal consisting of *P* layers. Unless specified otherwise, each layer has the shape of a parallelepiped and contains *MxN* spheres, where *M* and *N* are the number of spheres along each parallelepiped side. These spheres are periodically arranged in …*ABCABC*… layers as the (111) planes of an fcc crystal, although the method can be easily generalized for any possible arrangement of spherical particles.

For a finite CCA consisting of a stack of ideal crystal layers having the same shape and size, we can write the coordinates of the CCA spheres as

$$\vec{\rho} = \vec{M}_p + m\vec{a} + n\vec{b}$$

where $\vec{a}$ and $\vec{b}$ are the layer lattice vectors and $\vec{M}_p$ is the vector specifying the location of layer *p*. Integers *m* and *n* define the locations of individual spheres inside the layer, and in case of layers shaped as an identical parallelepipeds *MxN,* these indices run through the set of integers *m=1..M, n=1..N*.

We calculate the total scattering amplitude by summing contributions from all *P* layers stacked together to form the CCA.

$$\vec{E}_{sc}(\vec{r}) = \sum_{p=1}^{P} \vec{E}_{p}^{(111)}(\vec{r}) \tag{6.2}$$

Assuming that all spheres are identical and the amplitude of the incident wave A_p is the same for all particles in each layer, the scattering contribution from the individual layer *p* we can write as:

$$\vec{E}_{p}^{(111)}(\vec{r}) = A_p \cdot \vec{F}_0(\vec{r}) \cdot \sum_{m=1}^{M} \exp(i \cdot m \cdot \vec{a} \cdot \overrightarrow{\Delta k}) \cdot \sum_{n=1}^{N} \exp(i \cdot n \cdot \vec{b} \cdot \overrightarrow{\Delta k}) \cdot \exp(i \cdot \vec{M}_p \cdot \overrightarrow{\Delta k}) \tag{6.3}$$

In this formula both sums can be easily performed analytically, making calculations very fast for the case of layers shaped as parallelograms.

This computational procedure simulates diffraction from any stacking pattern of ideal (111) layers. In particular, it allows the study of how stacking faults in finite CCA's effect diffraction efficiencies, and it can be easily generalized to investigate other disorder in the CCA.

In Fig. 6-1 we show the scattering intensities for an incident plane light wave diffracted by a perfect colloidal crystal consisting of *P=45* (111) layers with each layer containing 60x50 spherical particles organized in a parallelogram plane layer. Here the stacking sequence of (111) planes is of type …*ABCABC*… corresponding to an fcc crystal.

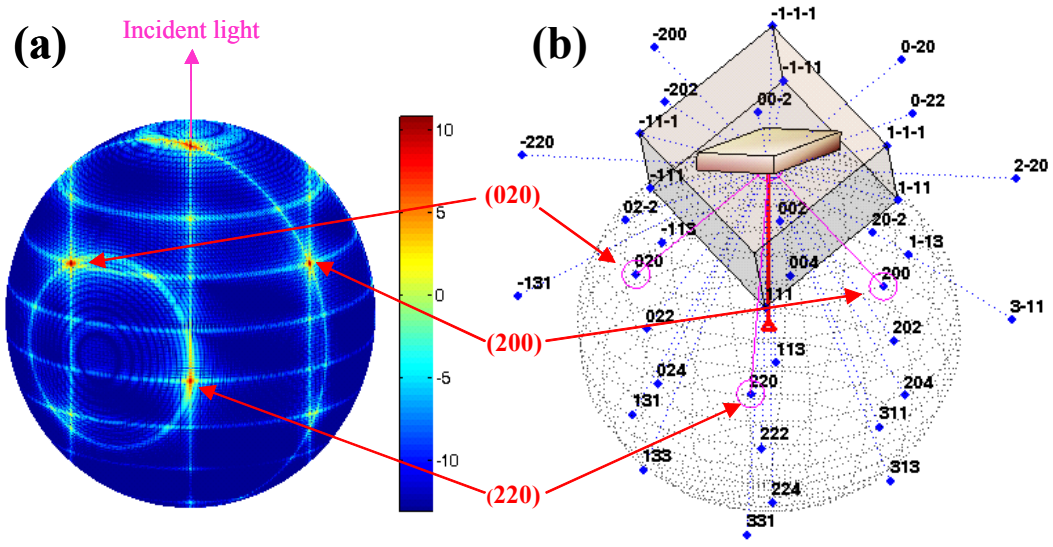

Figure 6-1 Spherical surface logarithmic scale color map ("scattering sphere") on panel (a) shows the scattered light intensity from a crystalline colloidal array (CCA). The large red arrow indicates the direction of the

incident light. The crystal was rotated about the z-axis to achieve diffraction by the (220) planes: the corresponding diffraction spot is shown at the center of (a). Two other diffraction spots correspond to Bragg diffraction from the (020) and (200) crystal planes. The diameter of the colloidal spheres is 270 nm, the lattice constant L=805 nm, the wavelength of incident light is 367 nm. Panel (b) plots the reflection (Ewald) sphere in reciprocal space. Reciprocal lattice points are shown by the blue dots, and the reciprocal points marked by the magenta circles are located near the surface of the reflection sphere and indicate the positions of the Bragg diffraction spots.

We simulated the diffraction of an incident plane wave (with direction shown by large magenta arrow in Fig. 6-1a of wavelength 367 nm by the crystal rotated such that it fulfills the Bragg condition for diffraction maximum from (200) planes, shown by the red spot in the middle of the scattering sphere. We define a Bragg angle as an incident glancing angle satisfying the Bragg condition. There are an infinite number of ways to orient the crystal such that the Bragg diffraction condition is satisfied for a particular crystal plane; all directions of incident light satisfying the Bragg condition occupy the surface of a cone whose axis is normal to the crystal planes. The diffracted intensity depends on the specific direction chosen along this Bragg cone surface, so one has to specify the exact orientation of the CCA relative the direction of incident light. In our calculations we assume the incident wave electric field is polarized perpendicular to the scattering plane, which contains the incident and Bragg scattering directions.

We choose a CCA orientation relative to the incident light for this calculation via the following procedure. The direction of incident light occurs along the *z* coordinate axis. Initially we orient the CCA such that the *z* axis is parallel to the [111] direction and the *x* axis is parallel to one of the sides of (111) layer parallelogram. Then we perform two rotations of the CCA: First, one around the *z* axis such that the normal to a particular diffracting plane occurs in the (*xz)* plane. A second rotation is done along the y axis until the glancing angle between the directions of incident light and the normal to the crystal plane fulfill the Bragg condition. The two rotation angles for the Fig. 6-1 calculation are $\pi/2$ and 0.2546 radians, respectively.

Some incident light directions along the (220) Bragg cone can also be diffracted by other crystal planes. For the specific CCA orientation in Fig. 6-1 367 nm incident light is Bragg diffracted simultaneously by the (220), (020) and (200) planes. The corresponding diffraction maxima are shown by the bright red spots and indicated by red arrows. This simultaneous diffraction by these crystal planes occurs only for this specific wavelength and direction of incident light.

A convenient way to determine the Bragg scattering directions is by using the Ewald sphere construction in reciprocal space (Fig. 6-1b). The yellow parallelepiped denotes the shape and orientation of the CCA crystal, while the blue dots are calculated points of reciprocal space labeled by their Miller indices. The grey cube indicates the cubic unit cell of the bcc reciprocal lattice. The length of the red arrow along the radius of the Ewald reflection sphere is equal to the wavevector of the incident light. The magenta reciprocal lattice points on the reflection sphere surface satisfy the Bragg diffraction condition.

The scattering sphere in Fig. 6-1a shows the values of the scattered intensities. Each point of the surface denotes a specific 3D direction whose color represents the logarithm of light intensity scattered into this direction by the crystal. The intensity at each point of the scattering sphere was calculated for a sphere of radius *r=1*.

We analyze the calculated CCA light scattering results and identify Bragg bright spots on the scattering sphere by plotting the scattering sphere together with the reflection Ewald sphere in reciprocal space. Thus, in Fig. 6-1 we would combine the plots (a) and (b) into a single plot, overlap the scattering and reflection sphere, and from the known positions of Bragg maxima in the reflection sphere identify the locations of bright spots in the scattering sphere.

For a perfect or nearly perfect crystal, the diffraction pattern consists of discrete "diffraction spots" that arise from the Bragg diffraction conditions. Each Bragg diffraction spot corresponds to constructive interference of light scattered by all individual particles. A Bragg maximum corresponds to simultaneous fulfillment of the three Laue equations for three lattice vectors $\vec{a}$, $\vec{b}$, $\vec{c}$, and any integer number *q*, *m*, *n*.

$$\vec{a}\cdot\overrightarrow{\Delta k}=2\pi q\,,\ \vec{b}\cdot\overrightarrow{\Delta k}=2\pi m\,,\ \vec{c}\cdot\overrightarrow{\Delta k}=2\pi n \qquad (6.4)$$

However, when only one or two of these equations are satisfied, only some of the colloidal particles in the crystal scatter light in phase, resulting in *partial* constructive interference. For a finite crystal this "partial constructive interference" is responsible for the appearance of bright lines and circles on the scattering sphere in Fig. 6-1a.

The CCA consists of stacked (111) crystal parallelograms layers, and each layer is represented by two 2D lattice vectors $\vec{a}'$ and $\vec{b}'$ along the parallelogram layer (these two vectors are not 3D fcc primitive translational lattice vectors, since not every lattice translation can be formed using these vectors). When either condition $\vec{a}'\cdot\overrightarrow{\Delta k}=2\pi q$ or $\vec{b}'\cdot\overrightarrow{\Delta k}=2\pi m$ is met, we

observe a bright circle on the surface of the scattering sphere as a result of partial constructive interference. When both of these conditions are simultaneously true, constructive interference occurs for every sphere from the same layer and results in 2D diffraction spots formed at the intersection of both lines. The identical (111) layers stacked together results in appearance of the "standard" 3D Bragg diffraction maximum.

The maximum intensity at the center of each Bragg peak results from the condition that scattering from every particle constructively interferes. Thus the total amplitude in this direction is just the single scattering form factor (calculated from Mie theory), times the total number of all particles in the crystal. Although the intensity value divided by the single sphere scattering form factor of the peak maximum is the same at the center of each Bragg diffraction spot, the area and the shape of the spots differ, resulting in a different values for the total integrated intensity for every peak.

For ideal periodic large crystals, the diffraction spots are very sharp peaks in specific Bragg directions, with very little light outside of these regions. We define the "integrated intensity of the diffraction from (nml) crystal planes" as the integrated intensity calculated over a solid angle large enough to contain the diffraction spot and then divided by the area of a single (111) layer.

The "Intensity", which refers to the square of the amplitude of the electric field at a point on the scattering sphere, is proportional to the electromagnetic energy irradiated into a specific direction.

6.2 VALIDITY OF THE METHOD: COMPARISON WITH THE EXACT SOLUTION FOR A 1D SLAB SYSTEM. ROLE OF MULTIPLE SCATTERING.

We tested the validity of our kinematic approach and the importance of multiple scattering by utilizing a 1D slab model and comparing the diffracted intensities calculated using kinematic theory with the exact results. First we modeled our 3D CCA set of (111) layers as a 1D array of slabs. It is generally accepted that the scattering efficiencies of light Bragg diffracted by (111) CCA planes can be modeled by scattering of light by 1D slabs [70]. To exactly determine the

light transmission and diffraction (the diffracted wave is simply a reflected wave in case of 1D slabs) in the 1D system we used the transfer matrix method (Appendix D).

When the Bragg diffraction condition is approximately satisfied for the (111) layers of a weak contrast fcc CCA crystal we can model the diffraction by replacing each (111) CCA layer with two slabs of different dielectric constant. The first slab with width L_1 and an effective refractive index n_{eff} marked as 1 in Fig. 6-2a represents the CCA particles layer depicted as a row of spheres, while the second "water" slab 2 has width L_2 and represents a water layer of refractive index n_w. The total width of both slabs equals the distance between (111) layers.

We define our effective 1D slab system by considering the diffraction of light by a single CCA (111) plane. The angular distribution of the light scattered intensities by a single (111) plane results from its 2D diffraction pattern, which in turn results from the hexagonally ordered spheres. Most of the light is concentrated in the narrow range of angles near the 2D Bragg maxima. Since we are modeling the Bragg diffraction from CCA (111) planes, we are consider only the light specularly reflected from the (111) planes at the zero order 2D maximum. It has previously been shown [75] that the scattering efficiency in the specular directions by a single plane of spherical particles can be approximated by the reflection from a single 1D slab.

We assigned the 1D slab system parameters, such as widths and refractive indexes of the slabs, by adjusting them until the intensities of light back-diffracted by a single (111) crystal layer was equal to that of a single colloidal slab of the 1D slab system. Specifically, the scattering by a CCA layer was calculated using kinematic theory and compared with exact result calculated for a 1D slab. The refractive index n_w of the water slab *2* was fixed to the value of the refractive index of bulk water, and the water slab width L_2 was fixed from the condition that the L_1+L_2 was the same as the distance between CCA (111) planes. The best match for a case of normal incidence was obtained for the L_1/L_2 ratio of 89/102 nm.

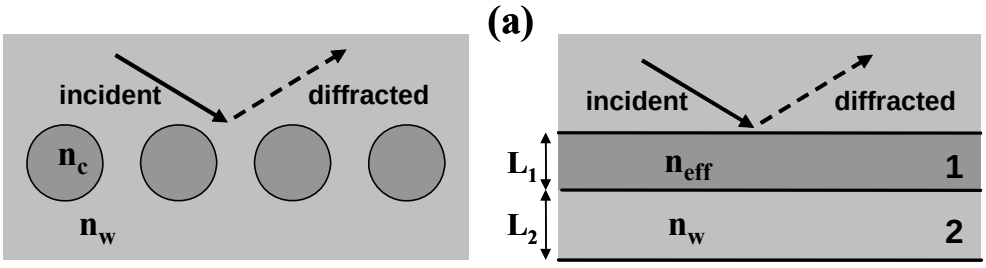

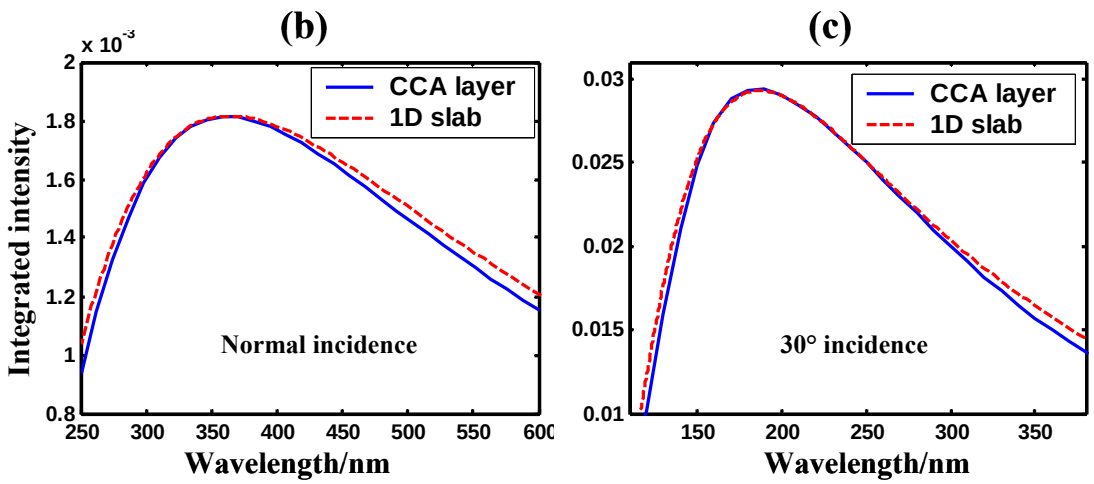

Figure 6-2 (a) CCA colloidal particles of a single (111) fcc CCA layer and the corresponding two slabs of the modeled 1D slab system. Colloidal particles have a refractive index n_c and are located in a water environment with a refractive index n_w. The 1D slab system consists of a bilayer of slab *1* with refractive index n_{eff} and the slab *2* with the refractive index of water. The total thickness of the two 1D slabs is the same as the distance between CCA (111) planes. (b) Integrated intensity of back-diffracted light by a single (111) crystal plane of 150x140 particles (blue solid curve) and by the 1D slab system (red dashed curve) is shown as a function of the wavelength of normally incident light. (c) same as (b), but for the light incident at glancing angle of 30°.

In Fig. 6-2b we plot the back-diffracted integrated intensity vs. wavelength of incident light of a single (111) layer of CCA (blue solid line) obtained in the KNM approximation, and by a corresponding slab of the effective 1D system (red dashed curve), obtained by an exact calculation. Incident light impinges normally on the (111) plane in Fig. 6-2b and at a 30° glancing angle of in Fig. 6-2c. The diffracted integrated intensity was obtained by integrating over the diffraction spot and ratioed to the integrated incident light intensity. The incident light energy flux is the intensity of the incident light multiplied by the area of the CCA layer. In the case of 1D slabs the normalized back-diffracted integrated intensity is simply the reflectance value.

The CCA crystal parameters used in calculations are as follows: the diameter of colloidal particles is 120 nm, and they constitute a 10% volume fraction giving a lattice constant of 330.8 nm. The refractive index of the colloidal particles and the surrounding medium (water) are n_c=1.6 and n_w =1.33, respectively.

At the Bragg direction of the exact reflection from the (111) plane all particles in this plane scatter coherently in phase for all wavelengths of the incident light wave. As a result, the

single sphere scattering efficiency dependence on the wavelength of light is the main factor contributing to the specific shape of the intensity curve in Fig. 6-2. The maximum of this curve results from a maximum of single sphere scattering efficiency at a particular wavelength.

Our calculated diffracted integrated intensities are proportional to the lateral size of the crystal layer and number of colloidal particles it contains. The width of the diffraction peak becomes narrower as the total number of colloidal particles in the crystal layer increase.

In the case of normal incidence we varied only the width L_1, and we were able to obtain a good fit between the two intensity curves. But this procedure would not work for angles of incidence other then normal. The dependence of the diffraction intensity vs. angle of incidence differs for a sphere compared to a 1D slab. The first dependence is determined by a single sphere Mie scattering amplitude dependence on the incident angle, while the later is determined by an interference of light scattered by a slab two plane boundaries. The single sphere scattering amplitude increases with the scattering angle much faster then the amplitude scattered from the 1D slab. Thus, if we simply increase the incident angle, the single (111) plane would scatter much more efficiently (for the spheres diameter comparable with the wavelength) then the 1D slab constructed for the case of normal incidence.

We use a different method to model the slabs scattering for light not normally incident. The increase in single sphere scattering efficiency at non-normal incidence we model by using 1D colloidal slab with higher refractive index, then in the case of normal incidence. Thus, in the case of non-normal incidence we vary two parameters of the 1D slab system, the colloidal slab refractive index n_{eff} and width L_1 until we obtain a good match between the 3D and 1D curves. For light incident at the glancing angle of $\alpha=30°$ the best fit value was $n_{eff}=1.837$. The 1D slabs width L_1/L_2 ratio was chosen by the fitting to be 78/113.

For perpendicularly polarized light a single CCA layer of colloidal spheres scatters 10-fold more light at $\alpha=30°$ incidence then at normal incidence (compare Fig. 6-2b and 6-2c). Thus as the incident glancing angle decreases, the dielectric contrast of the effective 1D slab system must increase.

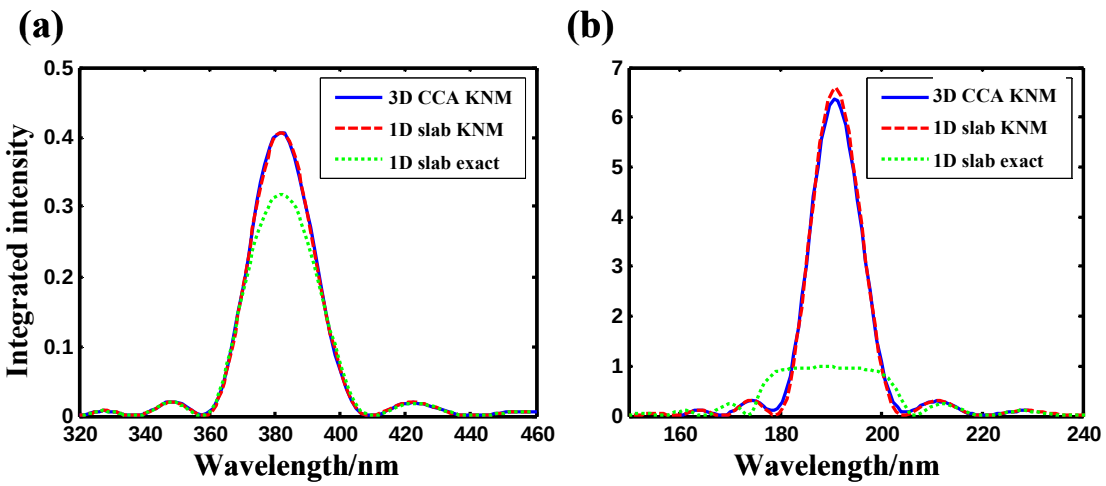

Figure 6-3 Integrated diffracted intensity scattered by a 150x140x15 particles 3D CCA (blue curve which overlaps the red curve) and by 1D system (red and green curves) versus wavelength of incident light. Red dashed curve was calculated using 1D KNM theory, while the green dotted curve is the 1D exact solution. (a) back-diffracted for normal incidence, (b) 30° glancing angle of incidence.

In Fig. 6-3 we compare the integrated intensity of light back-diffracted by a CCA of 15 (111) layers, each consisting of 150x140 colloidal particles, calculated in KNM theory using Eq. (6.1) and including all CCA layers. Light is incident normal to the crystal surface in Fig. 6-3a, while Fig. 6-3b shows the result for a 30° glancing angle of incidence. The results obtained for 3D CCA was compared with the results for the corresponding effective 1D slab system. We chose the range of wavelengths such as to analyze the spectral region around the 1st order Bragg diffraction maximum.

The back-diffracted and transmitted integrated intensity for the 1D system were calculated by the 1D exact and the 1D KNM methods. In the 1D KNM method (Appendix C) we simply calculate the reflection amplitude r_1 for a single 1D unit (consisting of two, colloidal and water, slabs) of thickness d and then summed contributions from all N units cells of the multi-slab system with the appropriate phase factor to obtain the total reflection amplitude r:

$$|r|^2 = |r_1|^2 \frac{\sin^2(\tfrac{1}{2} N \cdot \vec{d} \cdot \overrightarrow{\Delta k})}{\sin^2(\tfrac{1}{2} \cdot \vec{d} \cdot \overrightarrow{\Delta k})} \tag{6.5}$$

The red dashed curve shows the KNM theory result for the 1D slab system, where attenuation of the incident light in the crystal is ignored. The 3D and 1D KNM calculations give

almost identical results; the blue solid and the red dashed curves overlap. Since the KNM results for 3D and 1D case are so close, in the following analysis we examine the importance of multiple scattering and compare KNM and EXKNM results by utilizing only the 1D slab system.

The exact solution for diffraction from the 1D slab system calculated by using the transfer matrix method (see Appendix D) is shown in the Fig. 6-3 via the green dotted curve. By comparing the exact, KNM and EXKNM approximations we can examine the validity of kinematic theory and the relative importance of multiple scattering.

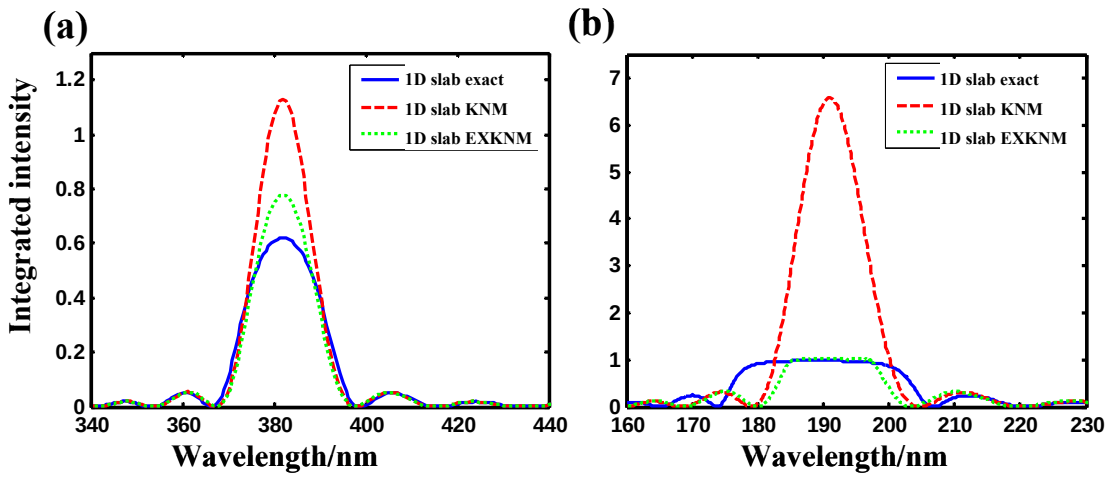

Figure 6-4 Reflectance versus wavelength of the incident light for a 1D slab system. Exact solution is plotted in the blue line, red dashed curve results from KNM theory with no attenuation of incident light, while the green dotted curve shows the EXKNM result. (a) normal incidence, 50 slabs, (b) 30° glancing angle for a system containing 30 slabs.

Fig. 6-4a shows the diffracted intensities for light normally incident on 1D slab system consisting of 50 slabs, while Fig. 6-4b shows the intensities for 30 slabs for a glancing incidence angle of 30°. The blue curve is the exact solution for the integrated intensity of the reflected light. The red dashed curve and the green dotted curve are the results of the KNM and EXKNM approximations respectively. KNM gives a reflectance greater then 1, because the intensity of incident light is not attenuated. EXKNM theory generates a much more accurate result.

The diffraction in Fig. 6-3b and 6-4b is much larger then in Fig. 6-3a and 6-4a, because the single spheres here scatter more efficiently for shorter wavelengths and for a larger scattering angle, resulting in more efficient Bragg diffraction. The increase in single scattering efficiency results in creation of stronger secondary rescattered waves and stronger multiple scattering. As a

result, the width of the diffraction peak, modeled by exact methods, becomes wider and the kinematic theory becomes less accurate.

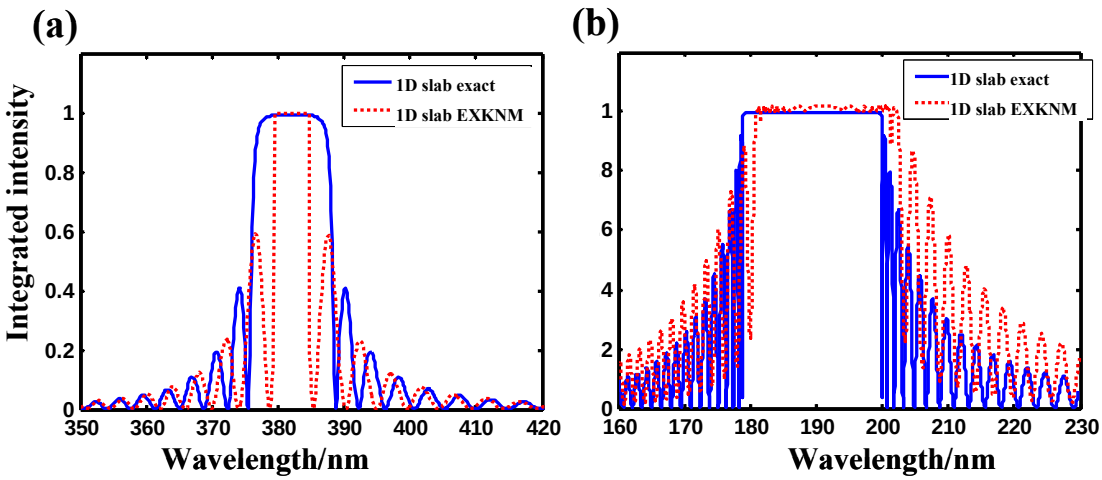

Figure 6-5 Diffracted intensities vs wavelength is plotted for 1D slab system consisting of 180 slabs, thick enough such that there is no transmitted light at the Bragg wavelength. Blue curve shows the exact result, while the red curve is calculated in accordance with EXKNM model. (a) normal incidence, (b) 30° glancing incidence angle.

Fig. 6-5 shows the diffracted intensities from a larger 1D slab system consisting of 180 slabs. The exact result is plotted in blue, while the EXKNM result is plotted in red.

KNM works well when the system is thin with a low dielectric contrast, where the total diffraction is significantly less then *1*. Thus, good agreement between the exact and kinematic results was obtained in Fig. 6-4a, especially in the wings of the main Bragg diffraction peak, where the reflected intensity is small.

EXKNM results in a value of the Bragg peak width 2-fold less then the exact result (Fig. 6-4b, 6-5a). In Fig. 6-5b, the Bragg peak widths are similar for both the exact and EXKNM calculations. The center of the exact result peak is slightly blueshifted relative to the EXKNM result.

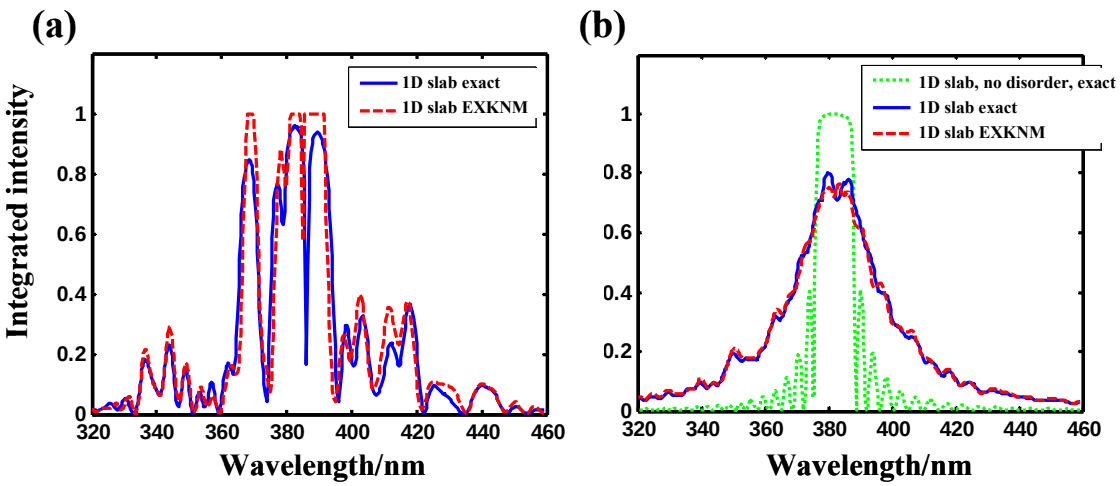

Figure 6-6 Wavelength dependence of diffracted intensities for disordered 1D slab system consisting of 180 slabs. Blue solid curve is the exact result. Red dotted curve is the EXKNM result. (a) single configuration of the disordered system, (b) diffracted intensities averaged over 80 random configurations. In (b) the exact result for a periodic system (dotted green curve) is compared to the exact and EXKNM results for the average over a disordered system (blue solid and red dashed lines).

Disorder in the 1D slab system broadens the Bragg peaks and increases the intensity of diffuse scattering. The total light scattering and the Bragg diffraction becomes more diffuse, the incident wave is less attenuated. We compare the exact and EXKNM calculations for a disordered 1D slab system (Fig. 6-6) and normally incident light. Disorder is included in both the high and low refractive index slabs into by assigning slabs thickness uniform random variations of 20% magnitude. We only varied the thickness of slabs comprising the system, but the refractive index of the slabs was kept constant at the value employed for the perfectly periodic system of Fig. 6-5.

Fig. 6-6a shows the diffracted intensities of a single configuration of a disordered 1D slab system. We see that the Bragg peak subdivides into a series of narrow peaks which are spread over a wider spectral region. Smaller features in the wings became more intense.

As a simple model of disorder we simply calculated a random ensemble of many configurations of 1D slab systems with random width slabs and averaged the diffracted intensities over this ensemble. In Fig. 6-6b we averaged the diffracted intensity over 80 random configurations and plotted the exact result in blue and the EXKNM result in red. As a reference, the exact result for a non-disordered periodic system is plotted in green. Averaging the disorder widens the Bragg peak and decreases its maximum value, the wings "smooth out". The exact and

EXKNM results are very similar. A more realistic model of a disorder in a system of many slabs would also include imperfection in the individual slabs, i.e., the boundaries of a slab would no longer be shaped as parallel planes resulting in thickness fluctuations within the slab.

6.3 LIGHT INTENSITIES SCATTERED BY DIFFERENT CRYSTAL PLANES OF CCA – WHICH FACTORS ARE IMPORTANT.

Perfect CCA's with a weak dielectric contrast diffract incident monochromatic plane waves into very small spots on the scattering sphere. In kinematic theory, the intensity of light diffracted exactly in the Bragg directions is simply the result of constructive interference of scattering contributions from all individual particles. The maximum total amplitude is thus proportional to the product of the single sphere scattering form factor and the total number of scattering particles in the crystal. The useful experimental quantity is the integrated intensity obtained by integrating over the diffraction spot on the scattering sphere.

A recent experimental study [74] examined the integrated intensities diffracted by different CCA planes for the same frequency of incident light (the crystal was rotated to achieve the Bragg condition for the different crystal planes). The intensities significantly differed for diffraction from different crystal planes. To explain this difference and analyze which factors affect the value of the integrated intensity, we calculate here the integrated intensities of light scattered by a CCA with the parameters similar to that of this study.

Our numerical model consist of an ideal fcc crystal consisting of several stacked (111) layers of a parallelogram shape and dimensions *MxN*. Unless specified otherwise, each colloidal particle has a diameter of 270 nm and we set the CCA fcc lattice constant at 805 nm, corresponding to a 10% particle volume fraction. We assume the refractive index of colloidal particles and the water as 1.6 and 1.33 correspondingly. The wavelength of incident light in the medium (water) was 337 nm.

We examined a thin CCA with a small dielectric contrast between colloidal particles and the surrounding media. We analyzed the integrated intensities diffracted by the (111), (222), (200), (220), and (311) planes. The monochromatic incident wave was oriented to meet the Bragg condition.

The factors affecting the integrated intensity over a diffraction spot include the magnitude of the single scattering form factor, the shape and the size of the diffraction spot, the effective number of layers, the shape and cross-sectional intensity profile of the incident light

Another important factor stems from the fact that often the size of CCA used in experiments is larger then the diameter of the incident beam. Upon changing the angle of incidence, we change the area of the CCA illuminated by the incident light and consequently change the number of colloidal particles participating in the scattering. This area is inversely proportional to the cosine of the angle β between the [111] and the incident direction. In what follows we assume for simplicity that the diameter of the incident beam is larger then the CCA size, although the opposite case can be easily treated by taking into account the mentioned above dependence from the cosine of the angle between the [111] and incident direction.

6.3.1 Single scattering form factor.

The single scattering contribution (the form factor of kinematic theory) of the colloidal particles depends on the scattering angle and the polarization of the incident light and thus will be different for diffraction from different crystal planes which have different Bragg diffraction angles.

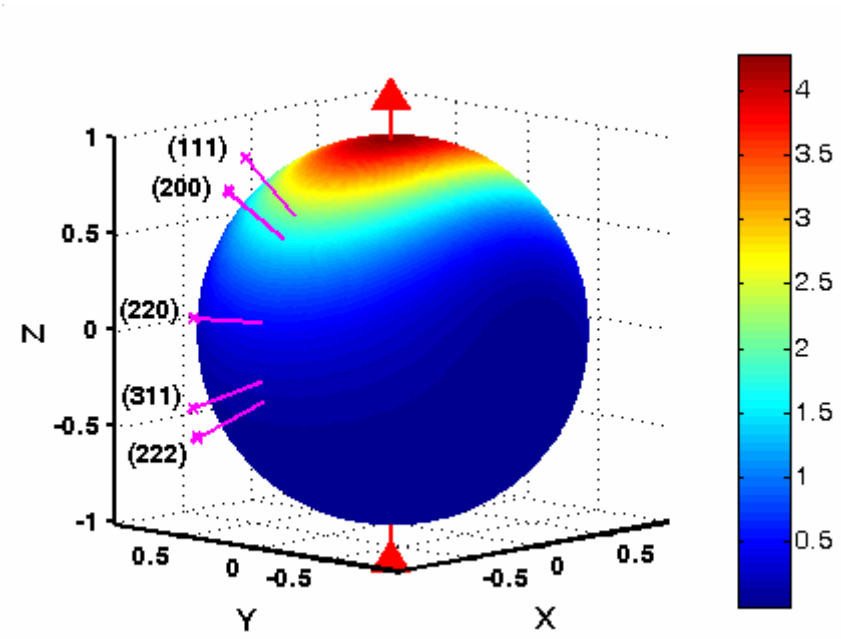

Figure 6-7 Spherical sphere color map shows the Mie scattering efficiency from a single spherical particle. We show the Bragg diffraction directions for several crystal planes, labeled by the Miller indices of corresponding crystal planes. Incident wavelength is 337 nm and sphere diameter is 270 nm.

We plot the 3D Mie scattering diagram (Fig. 6-7) for the light scattered by a single sphere and indicate the scattering directions for Bragg diffraction of specific crystal planes, for a light polarized perpendicular to the incident plane. The crystal was rotated about the z-axis to achieve diffraction by the different crystal planes. Different colors on the scattering sphere surface (Fig. 6-7) represent different scattered intensities as labeled in the color map (not the logarithmic scale). The ratios of diffracted intensities scattered by a single sphere at the Bragg directions for (111), (222), (200), (220) and (311) plane differ by relative proportions 1, 0.02, 0.75, 0.18 and 0.04 respectively.

This Mie scattering diagram shows that much more light is scattered in the forward direction then in the backward direction. This asymmetry becomes stronger as the ratio of the particle diameter to the wavelength of light increases. Exact formulas for Mie single sphere scattering in the far field approximation are given in Appendix E.

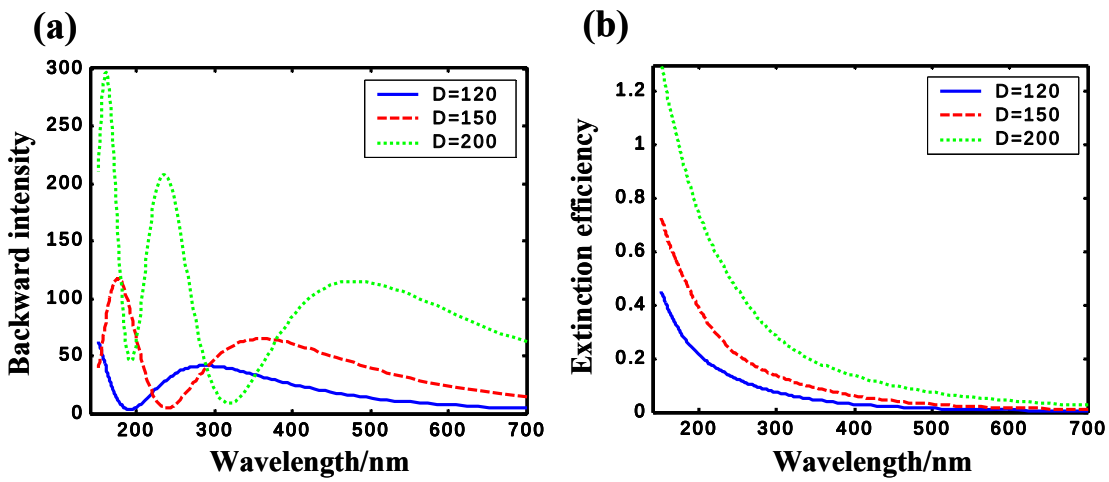

Figure 6-8 (a) intensity of the backscattered light from a single sphere is plotted vs wavelength (in water) of an incident light for three different sphere diameters: 120, 150 and 200 nm. The sphere refractive index is 1.6, the water refractive index is 1.33. (b) extinction efficiency is plotted for the same three spheres.

The distribution of intensities in the Mie scattering diagram at a fixed wavelength of the incident light is a function of the sphere diameter and the ratio between the refractive indices of spheres and the surrounding media. As a result, the scattering intensity at a specific direction depends on the sphere diameter and the dielectric contrast. In Fig. 6-8a we plot the dependence on the wavelength of incident light of the scattered intensity in the direction of exact backscattering for three different sphere diameters: 120, 150 and 200 nm.

The wavelength of the incident light in Fig. 6-8 is defined as a wavelength in water with refractive index 1.33. The green color light of 510 nm in vacuum corresponds approximately to a wavelength of 350 nm in water. At this wavelength a sphere with diameter 150 nm scatters backward most efficiently, approximately twice more efficiently then both 120 and 200 nm spheres. At approximately 310 nm the scattering intensity from the 200 nm sphere reaches a minimum, and is almost an order of magnitude smaller then the intensity from the 150 nm sphere.

Although the backward intensity oscillates as a function of wavelength in Fig. 6-8a, the extinction efficiency is monotonically increases with the decrease of the wavelength (Fig. 6-8b). The extinction efficiency (defined in in Appendix E) shows how much light is removed from the incident beam as a result of scattering in all 3D directions. The total amount of light scattered by the sphere is larger for a larger sphere, and increases with the decrease of the wavelength. But as

a result of interference effects, the intensity in a specific direction doesn't follow this monotonic trend observed for the extinction efficiency.

6.3.2 Shape of the diffraction spot.

Given an ideal crystal illuminated by a plane wave that is larger in area then the crystal, the single scattering theory predict that the total scattered light intensity at the exact Bragg direction is just the sum of intensities originating from all particles of the crystal, scattering perfectly in phase. But the integrated intensity taken over the entire Bragg diffraction spot on the scattering sphere depends on the area and shape of the diffraction spot and the distribution of intensity inside the spot. The shape and distribution of light intensities inside a diffraction spot are strongly dependent on the relative orientation of the crystal in space with respect to the incident and scattering light directions.

In this section we are going to study the dependence of the shape and area of a diffraction spot from the crystal orientation by utilizing KNM theory, where the simple analytical expression for the amplitude of scattered light can be derived. This understanding can be applied to the more realistic EXKNM approach, by assuming that the thickness of a finite CCA is determined by the effective number of layers calculated in EXKNM. We assume that the size of the CCA is smaller then the diameter of the incident beam. We assume that the incident beam is a plane wave, uniformly illuminating entire of the CCA surface at some glancing angle. In this situation, the shape and size of the Bragg diffraction spot is defined by the size and shape of the CCA. The results here are not relevant for experimental observations, since the size of CCA is always larger then the incident beam, in which case the shape and the size of the diffraction spot is determined by only the part of the CCA that is illuminated. Nevertheless, the study of the diffraction by a CCA smaller than the beam is important since it provides an understanding of how the finite size of the scattering volume of a CCA affects its diffraction properties. Another possible utility is the study of the "mosaic" crystals, which consist of many small crystals organized into a large polycrystalline sample.

The diffraction of an electromagnetic plane wave by M spheres along a 1D periodic array can be described by the interference function $\frac{\sin^2(\frac{1}{2}M \cdot \vec{a} \cdot \overrightarrow{\Delta k})}{\sin^2(\frac{1}{2} \cdot \vec{a} \cdot \overrightarrow{\Delta k})}$. The principal maximum value

of this function is M^2, and the width of the principal maximum is proportional to λ/M: thus for large M the integrated intensity is approximately proportional to M.

For a CCA shaped as a parallelepiped and having the dimensions $MxNxP$ along the lattice vectors $\vec{a}$, $\vec{b}$ and $\vec{c}$, the angular dependence of intensities is proportional to the Laue interference function

$$\frac{\sin^2(\frac{1}{2}M \cdot \vec{a} \cdot \overrightarrow{\Delta k})}{\sin^2(\frac{1}{2} \cdot \vec{a} \cdot \overrightarrow{\Delta k})} \times \frac{\sin^2(\frac{1}{2}N \cdot \vec{b} \cdot \overrightarrow{\Delta k})}{\sin^2(\frac{1}{2} \cdot \vec{b} \cdot \overrightarrow{\Delta k})} \times \frac{\sin^2(\frac{1}{2}P \cdot \vec{c} \cdot \overrightarrow{\Delta k})}{\sin^2(\frac{1}{2} \cdot \vec{c} \cdot \overrightarrow{\Delta k})} \tag{6.5}$$

and thus depends on the angles between the vector $\overrightarrow{\Delta k}$ and crystal lattice vectors $\vec{a}$, $\vec{b}$ and $\vec{c}$. From the form of the interference function it is easy to define a "diffraction spot": an exact Bragg direction is defined as the center of a diffraction spot and corresponds to the maximum of this function, which satisfies the Laue conditions (6.4). The first minimum of the interference function near the Bragg maximum defines the edges of the diffraction spot and can be easily obtained from the interference function.

If we plot the Laue interference function in reciprocal space, the volume around a primary maximum is bounded by the first minimum of the interference function, and all corresponding values of $\overrightarrow{\Delta k}$ inside this volume occupy a parallelepiped in reciprocal space with surface faces perpendicular to the crystal lattice vectors with dimensions proportional to λ/M, λ/N, λ/P. Thus the size of the reciprocal parallelepiped is proportional to the wavelength of light and inversely proportional to the size of the real crystal. We can determine the range of solid angles forming the diffraction spot by plotting the Ewald reflection sphere and the reciprocal parallelepiped having its center at the reciprocal lattice point location. The diffraction spot area is the intersection of the sphere of reflection with the reciprocal parallelepiped.

In our calculations the model of the CCA is comprised of stacks of parallelograms made out of (111) crystal planes, stacked according to the …ABCABC… pattern. All crystal layers of the same type are stacked exactly as one on a top of another, but the layers of different types are shifted relative to each other in a direction parallel within the (111) plane. Thus, this CCA is not aligned along primitive lattice vectors of FCC crystal, and its diffraction intensity is not represented by the Laue interference function (6.5). This CCA can be represented as consisting of three parts, each part consists of the layers of only the same type either A, or B, or C and has a shape of a parallelepiped and can be represented by the Laue interference function. The

scattering amplitude of light diffracted by the whole CCA can be represented as a sum of these three partial amplitudes resulting from each part and taken into account with the correct phase difference. Assuming that there is the same number of A, B and C layers, the interference function for the whole CCA can be represented as Laue interference function of one part times the sum of three phase factors. These phase factors do not depend on the size of the crystal. Thus the Bragg spot for the stacked CCA is the result of interference of three contributions, each represented by a reciprocal parallelepiped still approximately inversely proportional to the size of the CCA.

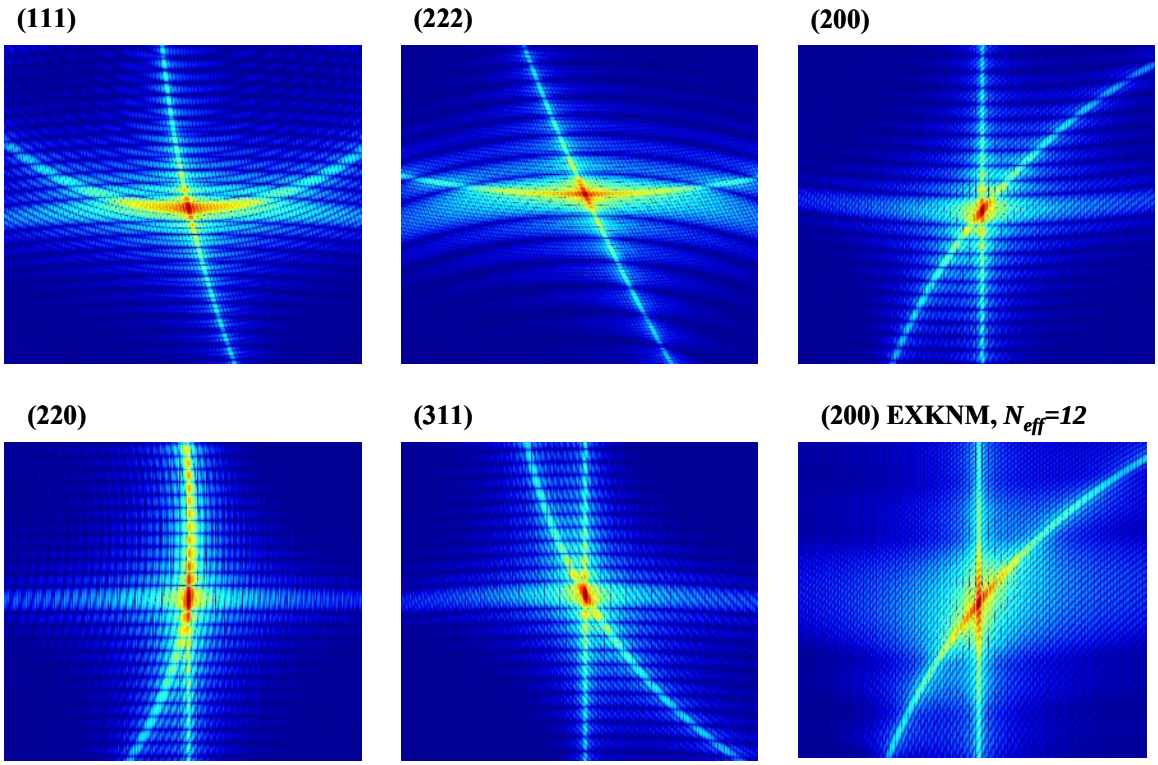

Figure 6-9 Small section of the scattering sphere around the Bragg maxima for the (111), (222), (200), (311) and (220) crystal planes. The color of the plot represents the logarithm of the light intensity. The number of particles in the crystal is 150x140x45 and the wavelength of incident light is 367 nm. All but the bottom right figure was calculated using KNM theory. The bottom right figure was calculated by using EXKNM theory.

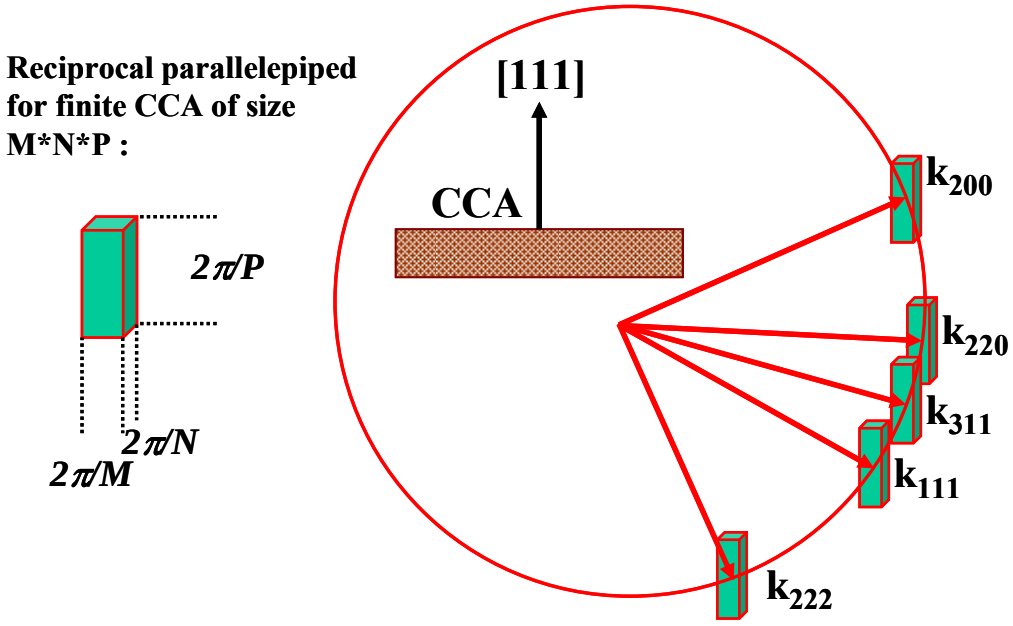

Figure 6-10 The shape and size of diffraction spots are determined by the intersection of a specific reciprocal lattice parallelepiped with the sphere of reflection. On the left we schematically plot individual reciprocal parallelepiped. Red arrows shows the approximate direction of the Bragg diffracted light relative to the specific CCA orientation, indicated at the figure.

In Fig. 6-9 we plot the small area of the scattering sphere near the Bragg diffraction maxima of the (111), (222), (200), (311) and (220) planes. The CCA parallelepiped consists of 45 (111) hexagonal layers of 160x150 spheres. To obtain Bragg diffraction from specific planes we rotate the CCA to the relevant Bragg diffraction condition and calculate the intensity around the diffraction spot. The diffraction spot occurs at intersection of three bright lines. For example, the long and narrow shape of the Bragg spot from (220) planes occurs as a result of two narrow bright lines intersecting at a small angle. All plots except the bottom right plot of Fig. 6-9 are obtained in the KNM approximation, and illustrate how the calculation of diffractions intensities using the Laue interference function (6.5) results in specific shape and size of the diffraction spot for different crystal planes.

More realistic EXKNM calculations would result in a different diffraction pattern: we study this pattern by comparing the diffraction spot obtained in KNM and EXKNM approximations. The bottom right panel of Fig. 6-9 shows an area of the scattering sphere near the (200) Bragg maximum calculated using the EXKNM approximation. In the EXKNM

approximation the amplitude of the propagating wave diminishes as it moves through the crystal, and for the case shown in Fig. 6-9 it decays to zero after $N_{eff} = 12$ layers.

Since only 12 layers participate in the scattering and the incident propagating light decays from layer to layer, the spacing between the dark and bright interference lines becomes larger while the contrast between them "smooth out" compared to the KNM case.

The shape and size of a diffraction spot is obtained by analyzing the intersection of the reflection sphere with the reciprocal parallelepiped. In Fig. 6-10 we plot the reflection sphere and the reciprocal parallelepipeds for all crystal planes under consideration and indicate by the arrows the orientation of the scattering angle relative to the [111] direction (indicated in the diagram as perpendicular to the CCA parallelepiped).

The typical CCA used in experiments typically has the shape of a rectangular thin film of a small number P of rather wide MxN layers, where $M = N >> P$. The corresponding reciprocal space parallelepiped is a long, narrow parallelepiped much longer in the [111] then the two other directions. Intersection of such a cylindrically shaped narrow parallelepiped with the reflection sphere for angles α not very close to $\pi/2$ is approximately proportional to $1/\cos(\alpha)$, where α is the angle between the diffracted light and the [111] directions.

Another geometric interpretation of a Bragg diffraction spot shape and size follows from the understanding of Bragg spot as an intersection of three bright lines (see, for example, Fig. 6-9). These lines are the result of the CCA finite size and specific shape, and each bright line represents the principal maximum of one of the three terms of the Laue interference function (6.5). In the case depicted in Fig. 6-9 two lines occurs as a result of the 2D diffraction from a single (111) plane shaped as a parallelogram MxN. The third line arises as a result of stacking together many (P) identical (111) layers. The width of each line scales inversely proportionally with the corresponding number of particles M, N and P. By increasing both M and N we decrease the widths of two of the bright lines comprising the Bragg spot.

Table 1. Integrated intensity W for the light diffracted from different crystal planes of CCA with dimensions 160x150x45 and 1800x1800x45 calculated in KNM theory. The single sphere scattering factor F is normalized relative to the value obtained for the [111] direction. N_{eff} is the EXKNM effective number of layers, obtained for a CCA of 1800x1800x100.

		160x150x45 (KNM)			1800x1800x45 (KNM)			(EXKNM)
Crystal planes	F/F_{111}	W	W/F	$\cos(\alpha)*W/F$	W	W/F	$\cos(\alpha)*W/F$	N_{eff}
(111)	1	37.21	24.43	9.65	44.81	29.43	11.62	6
(222)	0.02	0.383	13.99	11.05	0.407	14.87	11.74	97
(200)	0.75	22.21	19.48	9.03	28.42	24.93	11.55	12
(220)	0.18	9.085	32.23	2.74	33.95	120.6	10.27	10
(311)	0.04	1.380	23.55	7.9	1.994	34.05	11.43	48

The calculated values of the integrated intensity W for different crystal planes of a CCA with dimensions 160x150x45 and 1800x1800x45 was calculated using KNM theory for the same 367 nm wavelength of incident light (Table I). The quantity describing the geometrical shape and size of the diffraction spot in the KNM approximation is the intensity integrated over the diffraction spot and divided by single scattering efficiency F at the Bragg direction. We report this value as the W/F in Table I. Larger areas of diffraction spots results in the larger W/F values. The shape and area of the diffraction spots can be understood by analyzing an intersection of reflection sphere and reciprocal parallelepiped. For the wide and thin CCA with dimensions 1800x1800x45 the values of $\cos(\alpha)*W/F$ are close to each other, giving a simple formula for the scattering efficiency at specific Bragg directions. For the smaller CCA with dimensions 160x150x45 the intersection of the reciprocal parallelepiped and the reflection sphere has a complicated shape and area of the diffraction spot cannot be approximated by the simple relation $\cos(\alpha)*W/F$.

The practical utility of the area of the diffraction spot is that together with the single scattering form factor, it determines the scattering efficiency in the direction of Bragg diffraction from specific crystal planes. When a CCA is thin and some of the incident light is transmitted, then the amount of diffracted light is proportional to the diffraction spot area. For a thicker CCA's, when all incident light is diffracted and nothing is transmitted, then the scattering efficiency determine the effective number of layers after which the incident light completely decays. We have shown in this section, that when the CCA dimensions satisfy $M,N>>P$ and the diameter of the incident beam is larger then the CCA size, then the scattering efficiency is simply proportional to the $F/\cos(\alpha)$ When the CCA is larger then the diameter of the incident beam, then the scattering efficiency is proportional to the $F/\big(\cos(\alpha)\cos(\beta)\big)$, where α is the angle

between the [111] and scattering Bragg direction, β is the angle between the [111] and incident direction.

6.3.3 Effective number of layers.

In order to determine the effect of finite size and geometry on the diffraction we utilize the EXKNM theory. In Table I we report the effective number of layers involved in the diffraction N_{eff}, calculated using EXKNM for a CCA with dimensions 1800x1800x100. We use this large number of layers $P=100$ to ensure that the incident light completely decays inside the crystal at the chosen Bragg direction. This number of layers N_{eff} effectively determines the penetration depth available for the incident light and depends on the scattering efficiency of the CCA at the specific direction. The larger is the scattering efficiency W, the smaller is the penetration depth N_{eff}.

Table 2. EXKNM results were obtained for three different diameters D of colloidal particles organized in the CCA with dimensions 400x400x60 with lattice constant 380 nm. Effective number of layers N_{eff} was calculated for the light incident normally to the specific set of crystal planes. The single sphere scattering factor F is normalized relative to the value obtained for the [111] direction.

400x400x60, L=380 nm		**D=100 nm**		**D=150 nm**		**D=200 nm**	
crystal planes	***λ(nm)= $2d_{nml}$***	***F***	***N_eff***	***F***	***N_eff***	***F***	***N_eff***
(111)	438.79	0.0016	78	0.0108	29	0.0221	20
(222)	219.39	0.0221	85	0.0155	102	0.1401	33
(200)	380	0.0033	43	0.0174	18	0.0176	18
(220)	268.70	0.0146	59	0.0121	66	0.0590	28
(311)	229.15	0.0213	72	0.0060	145	0.1522	26

We calculated N_{eff} for the three different CCA's comprised of the colloidal particles of different diameters. The 400x400x60 dimensions and lattice constant 380 nm were used for all CCA's (Table II). The direction of incident light was tuned to be normal to the specific set of crystal planes, and the wavelength of light was chosen to satisfy the Bragg condition for these planes. The main factor responsible for the determined value of N_{eff} is the single scattering efficiency F obtained from the Mie theory for spheres. For diffraction from the (111) planes the

Table II single scattering efficiency increases with the size of the particles decreasing the penetration depth of the incident light, while in case of diffraction from (220) and (311) planes in Table II the *F* first decrease then increase with the increase of the *D*.

Another factor affecting the diffraction efficiency and the value of N_{eff} is the area of the diffraction spot, which is proportional to the wavelength of the diffracted light. In Table II, the value of $N_{eff}=20$ is smaller for the light back-diffracted by (111) planes made of spheres with $D=200$ *nm*, compared to the value of $N_{eff}=85$ in the case of diffraction by (222) planes made of spheres of $D=100$ *nm*, although the single scattering factor *F* is the same in both cases. But in the later case of diffraction by (222) planes the incident light has a smaller wavelength, therefore, smaller area of the diffraction spot and thus smaller value of the integrated intensity over the (222) diffraction spot, resulting in larger N_{eff}.

6.3.4 Dependence on crystal geometry.

So far in our presentation we have assumed that a CCA is a ...ABCABC... stack of (111) identical layers shaped as parallelepipeds and the incident plane wave uniformly illuminates the whole crystal. In this case the finite crystal geometry acts as a source of scattered light restricted by the aperture of CCA size, and the final scattering distribution of light is the combined effect of light diffraction on this solid aperture and coherent interferences of light coming from all colloidal particles regularly distributed inside the CCA. If we change the shape of the CCA, we would change the shape of the aperture and the light scattering pattern.

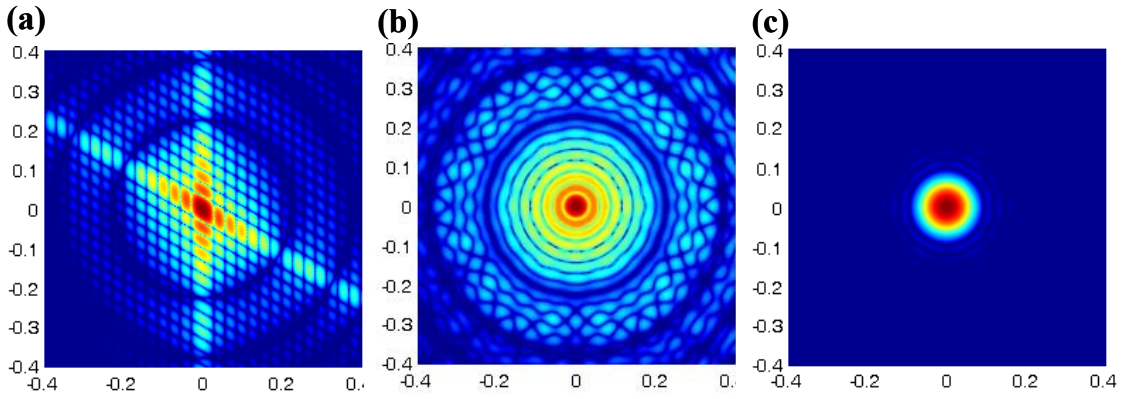

Figure 6-11 Small area of the scattering sphere around the backscattering direction is plotted using logarithmic scale for a CCA consisting of 21 (111) layers. (a) represents intensity distribution for a light diffracted by a CCA with (111) layers shaped as a 29x29 parallelograms, while (b) and (c) show the light distribution for (111) layers shaped as a circles. (c) was calculated for a Gaussian distribution of incident light, while (a) and (b) figures were calculated for a incident plane wave of constant amplitude.

In Fig. 6-11 470 nm light is normally incident to a CCA surface. We plot part of the 2D projection of the scattering sphere (with radius equal to one). The center of the picture corresponds to the direction of exact backscattering.

Light intensities diffracted by two CCA's were compared. In Fig. 6-11a each CCA (111) layer is a parallelogram of 29x29 spheres organized in hexagonal array. Diffraction from a CCA with (111) layers shaped as a circles is calculated in Fig. 6-11b and Fig. 6-11c. Each circular layer contains 823 colloidal particles. In (a) and (b) figures the incident light is a plane wave of constant amplitude, while for the figure (c) the incident beam crossectional profile has a Gaussian intensity distribution $f(r) = \exp\left(\frac{-r^2}{D^2/32}\right)$, where r is the distance from the center of the CCA layer, and D is the layer diameter.

When a single layer shaped as a parallelepiped diffracts a constant amplitude plane wave the diffraction pattern on the scattering sphere can be described by the Laue interference function $\frac{\sin^2(\frac{1}{2}M \cdot \vec{a} \cdot \overrightarrow{\Delta k})}{\sin^2(\frac{1}{2} \cdot \vec{a} \cdot \overrightarrow{\Delta k})} \times \frac{\sin^2(\frac{1}{2}N \cdot \vec{b} \cdot \overrightarrow{\Delta k})}{\sin^2(\frac{1}{2} \cdot \vec{b} \cdot \overrightarrow{\Delta k})}$ and consists of series of primary and subsidiary maxima, which are visible in the left figure as straight bright lines. The textbook example of the diffraction of a plane wave going through a parallelepiped hole reveals a similar pattern of straight bright lines (fringes) parallel to the edges of the parallelogram. Continuing the analogy, the angular width of the main diffraction maximum of the CCA layer is approximately λ/D, where $D = M \cdot a$ is the length along one of the dimensions of the parallelogram. The angular width of the light after transmitting through the hole is the same value. When we stack together several of the layers, another set of lines in the shape of the rings appear in Fig. 6-11a, visible as circular dark lines. The width and the spacing of these rings depend on the total number of layers. The value λ/D for the width of the Bragg spot is the same as a width of the reciprocal parallelepiped.

A CCA layer of circular shape results in the set of circular fringes in the diffraction pattern in Fig. 6-12b, similar to diffraction from a circular hole. Both Fig. 6-11a and Fig. 6-11b contain large dark rings as a result of multi-layer structure of the CCA.

Because of the Gaussian distribution profile of the incident beam in Fig. 6-11c the CCA acts as a "soft" aperture as the incident light gradually decreases in intensity toward the edges of the aperture. This tends to smooth out the whole diffraction picture and suppress the sharp variations of the diffracted light resulting from the sharp CCA boundaries. Notice that the larger rings originating from the multi-layer structure are still visible in Fig. 6-11c, but their intensity is much smaller due to the fact that there is very little scattered light in the dark regions beyond the bright 2D diffraction spots. The complex scattering pattern of diffracted light as the intersection of a large number of bright and dark lines forming subsidiary maxima and minima at their points of intersection is the result of the boundaries of the illuminated finite crystal: these lines are partially suppressed when the intensity of incident light is decreasing toward the CCA boundaries.

6.4 CONCLUSION.

In this chapter we used the single scattering approach to investigate light diffraction by weak dielectric contrast CCA's, consisting of a stack of (111) crystal layers. Although this method does not take into account multiple scattering effects, it can be used to analyze the macroscopically large CCA's consisting of many particles. The kinematic approach provides clear treatment of the effect of CCA finite size and specific shape on its diffraction properties. Another advantage of the method is its ability to treat arbitrary shapes of the incident light beam.

We extended the standard kinematic theory by including the attenuation of the incident light intensity while propagating through the crystal. This extension allows to calculate the effective depth of penetration of the incident light inside the CCA and is important in understanding the diffraction properties of realistic systems. The effective penetration depth was calculated and explained for several crystal planes of several CCA's.

We tested the impact of multiple scattering by comparing a results obtained by both kinematic methods with exact solutions for a 1D slab system. We suggested a method for

constructing an effective 1D system of dielectric slabs to model the diffraction from a (111) planes of a 3D CCA. We showed that for low contrast CCA's the diffracted intensities calculated by a EXKNM are close to the exact result obtained for an effective 1D slab system. Although modeling of 3D CCA by an effective 1D system is too simplistic, and does not account for all multiple scattering inside CCA, this model works reasonably well for analyzing the diffraction of (111) planes and provides a good benchmark of the validity of kinematic theories.

Kinematic methods can be used to study the large varieties of realistic experimental systems. Finite CCA's with the arbitrary size and shape and arbitrary distribution of colloidal particles inside the CCA can be easily incorporated intro the numerical model.

As the first step toward the study of arbitrary disordered CCA's, we focused in this chapter on the numerical study of the finite CCA's with perfect crystal structure. We studied the effects of the CCA finite size and shape on its diffraction properties. The different factors affecting the diffraction efficiencies were studied, including the single scattering form factor, the area and the shape of the diffraction spot, the shape and the intensity distribution in the incident light beam.

We showed that for the experimentally relevant CCA configuration of $M, N >> P$ that the area of the diffraction spot and thus the scattering efficiency is proportional to the $1/\cos(\alpha)$, where α is the angle between the [111] and scattering Bragg direction. We have also studied how deep the incident light penetrates into the CCA depending on the CCA shape and size, direction of the incident light and the diameter of the colloidal particles.

Chapter 7. Effect of stacking faults on diffraction by CCA, kinematic theory approach.

7.1 STACKING FAULTS IN CCA'S.

Stacking fault defects are probably the most common type of defects in CCA's manufactured by self-organization methods [32]. Most often fcc CCA's consist of a stack of (111) crystal layers characterized by an ABCABC.. stacking sequence. When this ideal crystal stacking order is destroyed, i.e. after C the next layer becomes B instead of A, we have a stacking fault at position C. Thermodynamics studies showed, that free energy differences between these two configurations are very small, resulting in a high possibility of stacking fault occurrences [77]. A stacking fault changes a (111) layer stacking order from ABCABC… (ABC) to ACBACB… (ACB), and there are only these two possible stacking sequences for a fcc crystal stacked from (111) layers. An ACB type crystal can be obtained from ABC type by rotation around [111] axis by 60° and the two sections on the opposite sides of the fault are referred to as twins.

The effect of stacking faults on the diffraction by CCA is to broaden the stop bands while at the same time reducing the peak diffracted intensities. The effect of stacking faults is much weaker in the case of diffraction by (111) planes compared to other crystal planes [32, 78]. The first stop band of (111) planes remains practically unaffected by the stacking faults, while the

higher order stop bands experience a considerable distortion [78]. In general, stacking faults, as the other types of disorder, affect more strongly the higher energy band gaps.

Kinematic theory has been applied to study X-ray diffraction by atomic crystals with stacking faults [79-81]. We will utilize a similar kinematic approach and derive the expressions for intensities diffracted by CCA and study the effect of stacking faults on the diffraction by different crystal planes. Here we investigate the effect of the number of stacking faults and their location inside CCA on diffracted intensities from several crystal planes.

Because we have defined the stacking fault as a change in stacking order of (111) planes but the distance between these planes has not changed, there is no stacking faults effect on diffraction efficiencies from (111) planes in standard kinematic (KNM) theory. Stacking faults may have considerable effects on intensity of scattering from other crystal planes, since the stacking faults in the [111] direction alter the periodic arraignment of crystal planes along directions other than [111].

In extended kinematic theory (EXKNM) the stacking faults can affect the diffraction efficiencies from the (111) planes through the mechanism of coupling with light Bragg diffracted from other crystal planes. When the Bragg condition is satisfied for other crystal planes in addition to (111) planes, the incident wave attenuates faster by diffracting in several simultaneous Bragg directions. This effect explains the results of reference [78], when the transmission spectrum calculated for the normal incidence was practically unaffected by stacking faults in the spectral range near the first stop band, but was strongly affected at the frequencies corresponding to higher stop bands. Since near the (111) first stop band there are no other planes satisfying the Bragg condition, the transmission spectra is then dominated by the diffraction from (111) planes and is unaffected by stacking faults. Near the second stop band, planes other then (111) start to diffract, resulting in a transmission spectrum affected by stacking faults.

7.2 GENERAL SOLUTION FOR DIFFRACTION INTENSITIES AT BRAGG DIRECTIONS FOR A CCA WITH STACKING FAULTS.

We represent a CCA having stacking faults as a combination of several crystal parts stacked on top of each other (Fig. 7-1a). Each part is an ideal crystal of either ABC or ACB type, and the change from one type to another occurs at the specific stacking fault in a (111) plane. The total diffraction amplitude $\vec{R}$ scattered from a whole CCA is the interference of scattered contributions from all these parts:

$$\vec{R} = \vec{R}^{ABC} + \vec{R}^{CBA} \tag{7.1}$$

where $\vec{R}^{ABC}$ ($\vec{R}^{CBA}$) is the contribution from all parts of ABC (CBA) type.

Note: Our definition of a stacking fault (as a change from ABC to CBA type) is completely general, and can be applied to any stacking order of A, B and C type layers. But, when the whole faulted crystal has many stacking faults, the description of the crystal as a combination of only ABC and CBA types is rather limited. If the distance between two stacking faults is only one or two (111) layers, then the part between the fault consists of only one or two layers. The diffraction maximums from such a small crystal can occur at all 2D Bragg directions of a (111) hexagonal crystal layer, and not only at the directions of ABC and CBA fcc crystals. For example, the Bragg directions corresponding to the hcp crystal structure can be significant for the crystal with stacking faults. We focus in this chapter on studying only Bragg directions of ABC and CBA fcc types crystals, assuming that the whole CCA is relatively weakly faulted and only these directions are important.

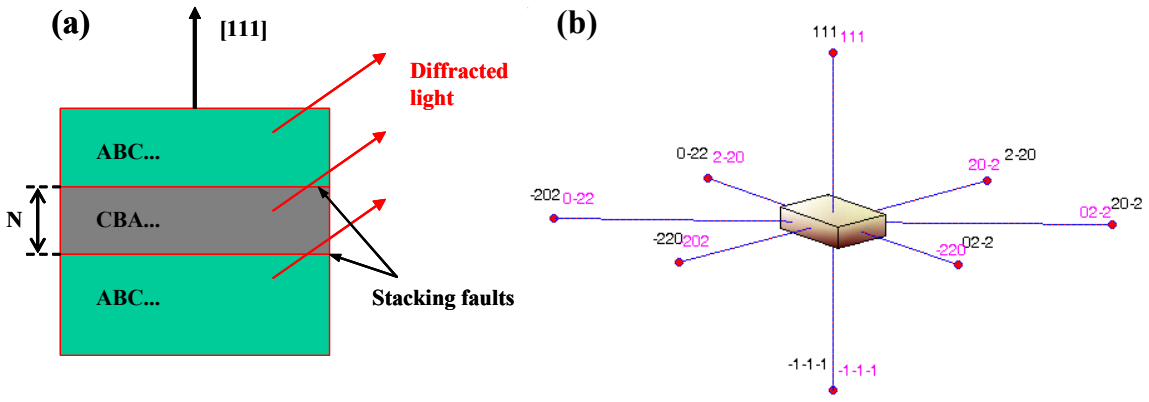

Figure 7-1 (a) CCA crystal with stacking faults along [111] direction can be represented as a stacked together several twinned parts, of ABC and CBA types. Each twinned pair is separated by a stacking fault. (b) Several points of reciprocal lattice are plotted for both ABC and CBA crystals. The twinned crystal is rotated by 60° relative to the [111] direction, and some reciprocal points for the twinned crystal (indicated in magenta) coincide with the reciprocal points of the regular crystal (in black). For example, the 0-22 reciprocal point coincides with the 2-20 reciprocal point for the twin.

Let's first analyze the $\vec{R}^{ABC}$ contribution. At Bragg directions this contribution consists of only three terms:

$$\vec{R}_{ABC} = \vec{R}_1 + \vec{R}_2 \cdot e^{i\phi_2} + \vec{R}_3 \cdot e^{i\phi_3} = \vec{R}_1 + \vec{R}_2 \cdot e^{i\cdot\overrightarrow{\Delta k}\cdot\vec{d}} + \vec{R}_3 \cdot e^{i\cdot\overrightarrow{\Delta k}\cdot 2\vec{d}} \qquad (7.2)$$

The first term $\vec{R}_1$ is the amplitude of light diffracted from all ABC parts interfering constructively with the top part of the CCA in Fig. 7-1a. The diffraction contributions from the different parts are in phase when the number of layers N separating these parts (indicated in the Fig. 7-1a) is divisible by 3 and can be expressed as $N=3n$, where n is an arbitrary integer. The second term represents the contributions from all ABC parts, with the number of layers separating them and the top part being $N=3n+1$ and phase difference $\phi_2 = \overrightarrow{\Delta k}\cdot\vec{d}$, where the $\overrightarrow{\Delta k}$ is the difference between the incident and diffracted wavevectors and $\vec{d}$ is the vector in the [111] direction with the magnitude of distance between the (111) layers. The third term sums the contributions from all ABC parts separated from the top part by $N=3n+2$ layers, and with a phase difference of $\phi_3 = \overrightarrow{\Delta k}\cdot 2\vec{d}$.

Expressing the Bragg condition as $\overrightarrow{\Delta k} = \vec{G}_{hkl}$, noting that the reciprocal vector corresponding to the (hkl) planes is $\vec{G}_{hkl} = \frac{2\pi}{L} \cdot (h,\ \ k,\ \ l)$, and using $\vec{d} = \frac{L}{3} \cdot (1,\ \ 1,\ \ 1)$ we obtain:

$$\overrightarrow{\Delta k} \cdot \vec{d} = \vec{G}_{hkl} \cdot \vec{d} = \tfrac{2}{3}\pi \cdot (h + k + l) \tag{7.3}$$

Now, depending on the Miller indices h, k, l, there are three possible options for a phase $\phi_2 = \overrightarrow{\Delta k} \cdot \vec{d}$ in the interval between –π and + π:

$$\overrightarrow{\Delta k} \cdot \vec{d} = \begin{cases} 0, & \text{for } h + k + l = 3n \\ \frac{2}{3}\pi, & \text{for } h + k + l = 3n + 1 \\ -\frac{2}{3}\pi, & \text{for } h + k + l = 3n + 2 \end{cases} \tag{7.4}$$

here *n* is any integer number. Therefore, the total contribution from all ABC parts depends on Miller indices h, k, l and take be one of the three values:

$$\vec{R}_{ABC} = \begin{cases} \vec{R}_1 + \vec{R}_2 + \vec{R}_3 & \text{for } h + k + l = 3n \\ \vec{R}_1 + \vec{R}_2 \cdot e^{i\frac{2}{3}\pi} + \vec{R}_3 \cdot e^{-i\frac{2}{3}\pi} & \text{for } h + k + l = 3n + 1 \\ \vec{R}_1 + \vec{R}_2 \cdot e^{-i\frac{2}{3}\pi} + \vec{R}_3 \cdot e^{i\frac{2}{3}\pi} & \text{for } h + k + l = 3n + 2 \end{cases} \tag{7.5}$$

When the Miller indices of the (hkl) planes satisfy *h+k+l=3n*, contributions from all ABC parts are always in phase at the Bragg direction, and stacking faults have no effect on the diffraction from (hkl) planes of all ABC parts.

The reciprocal points of the twinned CBA crystal can be obtained by the rotation of the ABC crystal reciprocal points by 60° around the [111] axis. An additional fact that can be derived by inspecting on the same plot the reciprocal space of both ABC and twinned CBA crystals is that some of the reciprocal points for both types coincide, while others don't. Specifically, when the condition *h+k+l=3n* is satisfied for ABC crystal, for every reciprocal point (hkl) there is always reciprocal point (h',k',l') of the twinned CBA crystal coinciding with it (non-primes are for the ABC crystal, primes indicate reciprocal points of the CBA crystal). These (h',k',l') reciprocal points of a twinned crystal satisfy the similar relationship *h'+k'+l'=3n.* As an example we calculate and plot at Fig. 7-1(b) several coinciding reciprocal points for both ABC and twinned CBA crystals. The conclusion that follows is that, when the condition *h+k+l=3n* holds, contributions from all ABC and all CBA parts are in phase at the

Bragg direction, and the stacking faults have no effect. The examples of these special planes include the (111), (2-20), (3-11), etc.

For all other crystal planes satisfying the condition $h+k+l=3n+1$ or $h+k+l=3n+2$, the contributions from different ABC parts are not necessarily in phase, and in general can be combined into three terms, depending on how many layers separate these parts. The absolute amplitude values of these terms are R_1, R_2 and R_3, and since we are calculating amplitudes in an exact Bragg direction, every amplitude is simply a scattering efficiency of an individual particle multiplied by the number of particles contained in the corresponding crystal section. The diffraction contributions absolute values R_1, R_2, R_3 are constant, the phase differences between them are constant, and therefore they do not depend on the crystal plane, or parameters of incident light. We conclude that the stacking faults affect the diffracted intensity at Bragg directions similarly for all crystal planes, and the diffracted intensities at these Bragg directions are the same.

These conclusions were obtained using KNM methodology. Including the attenuation of the incident wave in the framework of EXKNM theory does not change the final diffracted amplitude in expression (7.5). But in EXKNM the absolute values R_1, R_2 and R_3 are no longer independent of the crystal planes. The contribution of each individual ABC part depends on the intensity of the propagating wave reaching this part, and thus depends on how efficiently the specific crystal planes scatter. Crystal planes with high diffraction efficiency attenuate incident light faster, with the result that there are an effective number of layers of the CCA surface region participate in scattering. Only the stacking faults located within the relevant attenuation length (defined as effective number of layers) affect diffraction efficiencies. And, if the Miller indices of the crystal planes satisfy $h+k+l=3n$, the stacking fault(s) have no effect on the diffraction efficiencies.

7.3 EFFECT OF THE NUMBER AND LOCATIONS OF STACKING FAULTS ON INTEGRATED INTENSITIES DIFFRACTED BY (111), (200), (220) AND (311) PLANES.

We numerically studied (using the KNM approach) the diffraction efficiencies from the crystal planes with Miller indices satisfying the condition $h+k+l=3n$ and confirmed that these intensities, as expected, are unaffected by stacking faults. The planes we studied include (111), (-220) and (3-11) planes. In contrast, the directions and intensities of scattered light by other planes strongly depend on the exact location of the stacking faults within the CCA. In Fig. 7.2 we illustrate this dependence by plotting the ratios of integrated diffraction intensities from different crystal planes relative to the diffraction intensity from the (111) plane as a function of specific locations of the stacking faults inside the crystal. Fig. 7.2(a) is a calculation for a single stacking fault. Here, a single stacking fault splits the CCA into two parts, of ABC and CBA twin type, where the ABC part is on the top and CBA part is at the bottom of the CCA. The CCA consists of 60 stacked together (111) layers and every layer is a parallelogram 1900x1800 of colloidal particles. The CCA lattice constant is 805 nm and the wavelength of the incident light is 367 nm.

We calculate light intensities near the Bragg diffraction direction from the (111), (200), (220) and (311) crystal planes of the ABC type crystal. These directions are not Bragg directions of the CBA twin, thus the twin part does not produce appreciable intensities at these directions. Moving the stacking fault from the top layer (1) to the bottom layer (60), we increase the number of layers in the single ABC part of the crystal and therefore monotonically increase the total diffracted intensity.

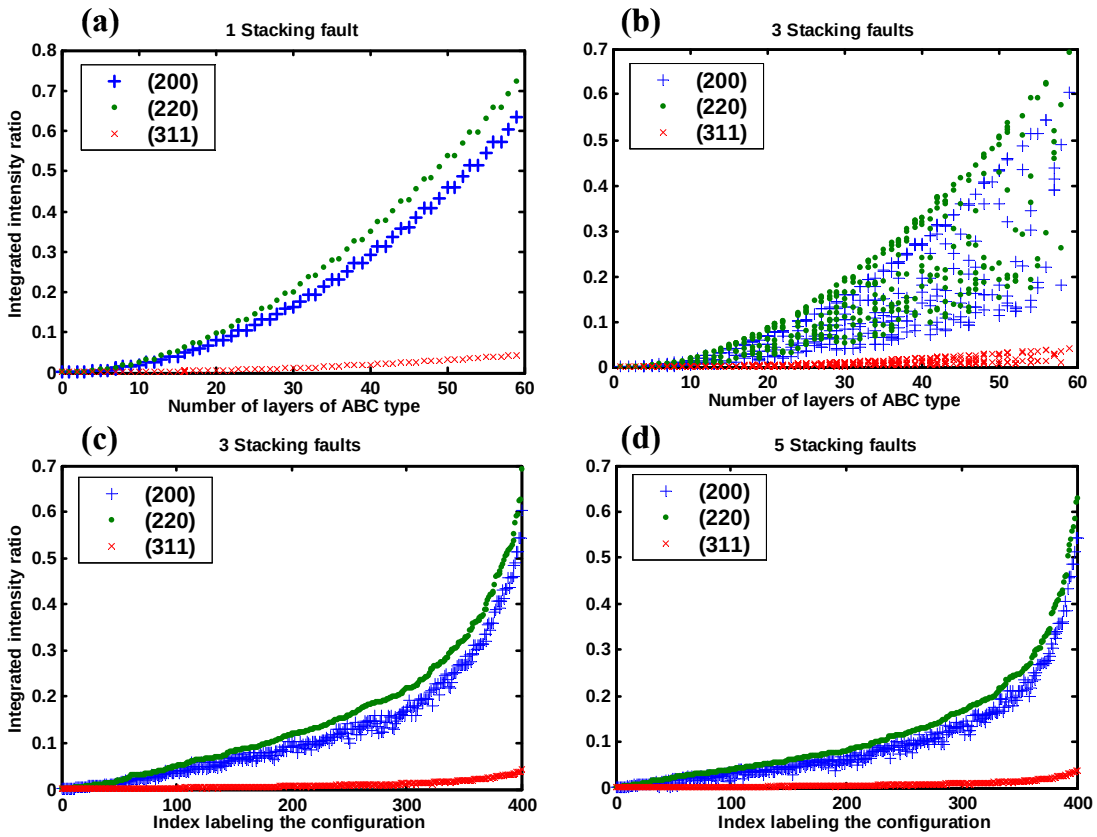

Figure 7-2 Diffraction integrated intensity from (200), (220) and (311) planes relative to that from the (111) plane as a function of a number and locations of stacking faults. (a) For the single stacking fault diffracted intensity are plotted vs. the number of layers in ABC part of the crystal. (b), (c) and (d) - calculations were performed for 3 and 5 stacking faults which were randomly placed inside 60 (111) layers, and then repeated for 400 different configurations. In (b) the diffracted intensities were plotted vs the total number of layers in all ABC parts. In (c) the same results as in (b) are plotted by sorting all configurations in the direction such that intensities diffracted by (220) planes are monotonically increasing. (d) the same as (c) calculated for 5 stacking faults.

Fig. 7-2(b) and (c) plots the ratios of diffraction integrated intensities for each of 400 possible locations of three randomly placed stacking faults within the 60 (111) layers. As the absicca in Fig. 7-2(b) we use the total number of layers of all crystal parts of ABC type. When we have 3 stacking faults, our crystal consists of four parts, two of type ABC and other two parts are of type CBA. We see that by using the number of ABC layers as a plotting parameter for the X axis, we calculate multiple values for the diffracted intensity ratio depending on the sites of the stacking faults. Diffracted intensity in this case results from the interference between

contributions arising from two parts of ABC type, and hence depends strongly on the exact locations of the faults inside the crystal.

The same diffracted integrated intensity data as in Fig. 7-2(b) is plotted in Fig. 7-2(c) but here we use a different plotting parameter for the absicca. We sorted all 400 configurations of characterized random fault locations such that the diffraction intensity from (220) planes monotonically increases. Fig. 7-2(d) represents similarly sorted diffracted intensities obtained for the CCA with 5 stacking faults.

The data plotted at Fig. 7-2 indicates a very strong dependence of the intensity of light scattered by different crystal planes from the locations of the stacking faults. But for any specific stacking fault configuration inside the CCA, for any point of the abscissa in Fig. 7-2(c) and (d) the ratio between the integrated intensities diffracted by different crystal planes is similar. Diffracted efficiencies from different crystal planes in figures (c) and (d) are reduced by stacking faults, and the reduction ratio is very similar for all planes in accordance with our conclusions from the theory of stacking faults.

Although the diffraction efficiencies for (220) planes increase monotonically in (c) and (d), the results from other planes deviates from the exact monotonic increase. This is easily seen for the (200) plane as a distribution of intensities in contrast with the monotonically increasing curve for the (220) plane. This effect can be explained as follows. We plot the diffraction intensities integrated over the diffraction spot intensity, which depends not only on the amplitude at the exact Bragg direction, but also on the width of the spot and the distribution of intensities inside the diffraction spot. The kinematic theory expression for the amplitude at the exact Bragg direction (7.5) results in the same reduction of amplitude for all crystal planes (except the planes satisfying $h+k+l=3n$). Outside this exact Bragg condition the effect of the stacking faults on the scattered amplitudes is different. For a small width Bragg spot we would expect that the value of the integrated intensity is mainly determined by the amplitude in the center of the diffraction spot, resulting in similar ratios between different planes diffracted efficiencies in Fig. 7-2(c) and (d). Another factor that could affect the diffracted efficiencies from different planes is the contributions from the twinned CBA part. Although in the Bragg direction of the ABC crystal the scattering amplitude from the (111) planes of the CBA parts are not perfectly in phase, still, they can partially constructively interfere to produce some finite amount of light scattered in Bragg ABC directions, especially for a small total number of (111) layers in the CCA.

Comparing Fig. 7-2(c) and (d) we conclude that the number of stacking faults has relatively less effect on the diffraction efficiencies than does the exact location of the stacking faults. The shapes of the curves in (c) are similar to those obtained in (d), but curves in (d) on average correspond to lower scattering efficiencies than the results presented in (c).

We investigated the impact of the number of stacking faults on the diffraction efficiencies from different crystal planes by calculating the average diffraction intensity as a function of the percentage of stacking faults (Fig. 7-3). Zero percent stacking faults corresponds to a perfect fcc crystal. Two stacking faults within 60 layers correspond to 3.33% of stacking faults. We take the average of all diffracted intensities from the (200), (220) and (311) planes obtained in Fig 7-2 to extract the average value of intensities for 3.33 % of stacking faults and plot this single value in Fig 7-3.

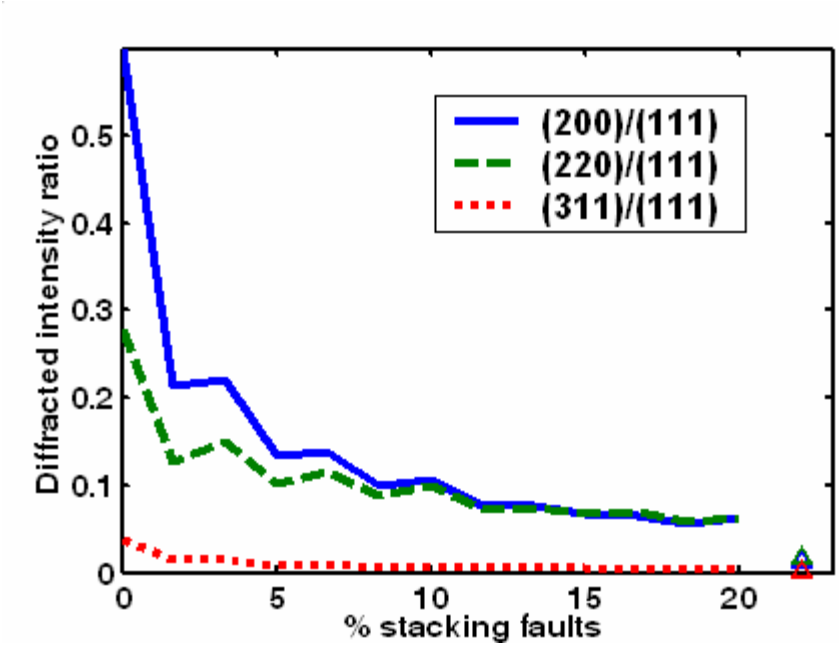

Figure 7-3. Dependence of the diffraction intensity from the (200), (220) and (311) planes on the percentage of stacking faults for a CCA containing 60 layers stacked along z with 250 x 240 particles in each layer. The value plotted is the average intensity ratio relative to the intensity diffracted by the (111) planes. The average values were calculated by averaging the effect of 400 possible configurations of the indicated number of stacking faults. The triangles indicate the diffraction from a random stacked CCA.

The average diffraction efficiencies from the (200), (220) and (311) planes decrease with the number of stacking faults. The impact of a stacking fault depends strongly on its location, as

we illustrated in calculations in Fig. 7-2. For example, a single stacking fault located in the middle of the crystal reduces the diffraction efficiencies by more then 2-fold. Fig. 7-3 plots the average diffraction intensity calculated from 400 randomly selected stacking fault configurations. In the case of a single stacking fault only 60 configurations are possible. For two faults, 60 x 59 configurations occur, etc.

These (111) plane stacking faults affect the diffraction of different Miller index planes to a similar degree - the ratio between the average diffraction efficiencies of (200), (220) and (311) planes remains practically the same for different numbers of stacking faults (taken at the same value of abscissa).

We also calculated the diffraction intensities for a CCA with complete random stacking of the (111) planes. The diffraction efficiencies ratios for the (111), (200), (220) and (311) planes in a random stacked CCA were calculated to be 1, 0.0131, 0.0165 and 0.0009, respectively. These values are indicated by triangles in Fig. 7-3, and again, the relative ratios between them are the same as the ratio between the curves of Fig. 7-3.

7.4 EFFECT OF STACKING FAULTS ON DIFFRACTION PEAKS SHAPES, WIDTH AND MAXIMUM INTENSITIES.

In this section we study how the stacking faults affect the spectrum of light diffracted by a CCA. We calculated the dependence of diffraction intensities integrated over the backward scattering hemisphere on the wavelength of incident light for a CCA consisting of 45 stacked together (111) layers, where each layer has a parallelogram shape containing 60x50 colloidal particles. We define the backward hemisphere as the half of the 3D space containing the incident wavevector and delineated by the infinite (111) plane.

In Fig. 7-4(a) we calculate the diffraction spectrum for an ideal crystal, in Fig. 7-4(c) the CCA contain the single stacking fault located in the middle of the crystal, while in Fig. 7-4(b) and (d) the CCA contains two stacking faults, located at different positions inside the crystal, specifically at 15 and 29 layers in (b), and at the 12 and 26 layers in (d).

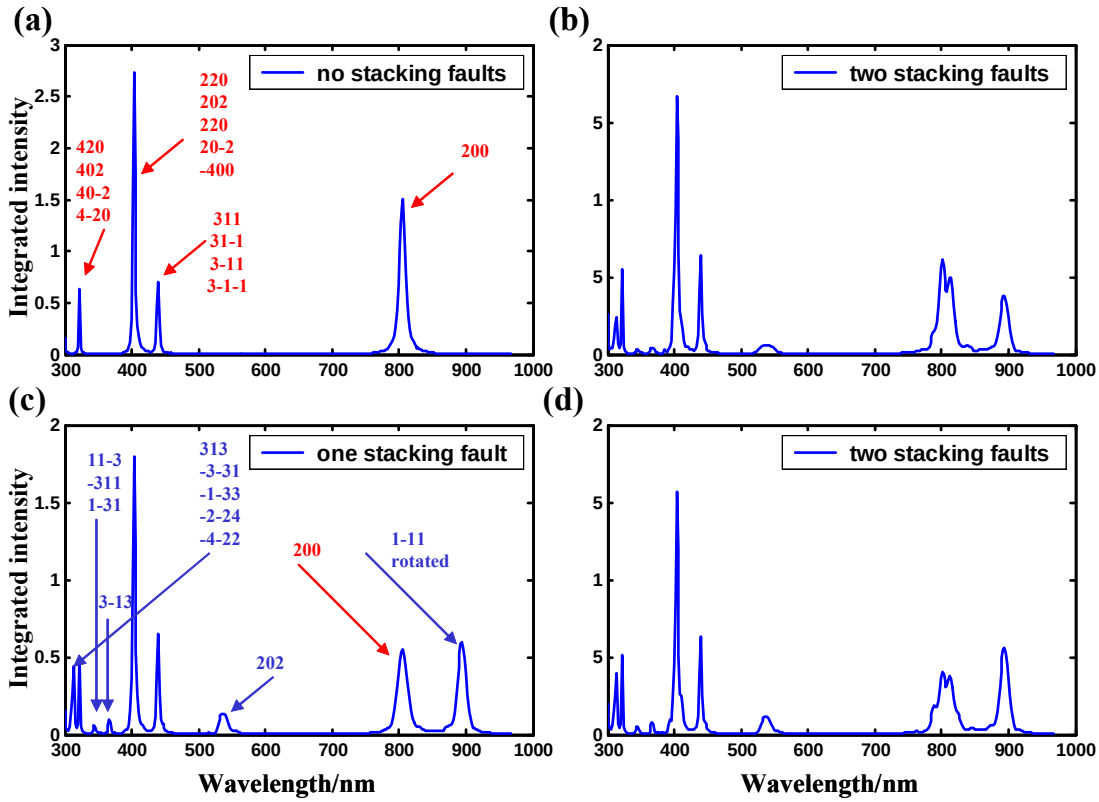

Figure 7-4 Total integrated intensity scattered at backward hemisphere vs wavelength of incident light. CCA dimensions are 60x50x45, colloidal spheres diameter 270 nm, incident light is oriented along [200] direction. (a) – ideal crystal with no stacking faults, (c) – there is a single stacking fault in the middle of the CCA. (b) and (d) are the diffraction spectra for the CCA with two stacking faults, and the locations of the faults are at 15 and 29 layers in (b), and at 12 and 26 layers in (d). Individual peaks resulting from the diffraction by the planes of ABC type crystal are labeled in red, and from the diffraction by the planes of CBA type - in blue.

The calculations in Fig. 7-4 were performed for incident light oriented along the [200] direction, and the diffraction spectrum consist of a series of peaks. For an ideal crystal each diffraction peak corresponds to the Bragg diffraction from specific set of crystal planes, which we label in red in Fig. 7-4(a). The large peak near 800 nm results from the diffraction by (200) planes, and the diffraction light is directed exactly backwards with respect to the incident light. The three peaks in the blue range of the spectrum result from simultaneous diffraction by several crystal planes. We assume that the CCA in (a) is of the ABC type. Introducing a single stacking fault in the middle of the CCA dramatically changes the diffracted intensity spectrum (Fig. 7-

4(c)). The diffraction spectrum now consist of peaks of two types, in addition to the peaks diffracted by a crystal part of ABC type there are also peaks produced by the planes of the CBA crystal part, indicated by blue labels. As a result of the stacking fault, the intensity of the peaks from the ABC part decreases relative to the ideal crystal peak intensities shown in (a), since there are a smaller number of ABC layers.

Diffracted intensity for the CCA with two stacking faults is calculated in Fig. 7-4(b) and (d). The CCA with two stacking faults consist of the three parts, two of ABC type separated by a part of CBA type. As a result of the interference of light diffracted by the two parts of ABC type, the corresponding diffraction peaks might broaden and split into double peaks, as is visible for the (200) peak. The specific shape of the resulting double peak depends on the phase difference between the two contributions, and thus is sensitive to the exact location of the stacking faults, as illustrated by comparing figures (b) and (d).

The effect of the stacking faults on the intensity distribution over the Bragg spot is studied in Fig. 7-5. The small area of the scattering sphere around the (200) diffraction spot is plotted, for the same CCA and direction of incident light as in Fig. 7-4. The wavelength of the incident light corresponds to the Bragg maximum, and is the same as the middle of the (200) peak in Fig. 7-5.

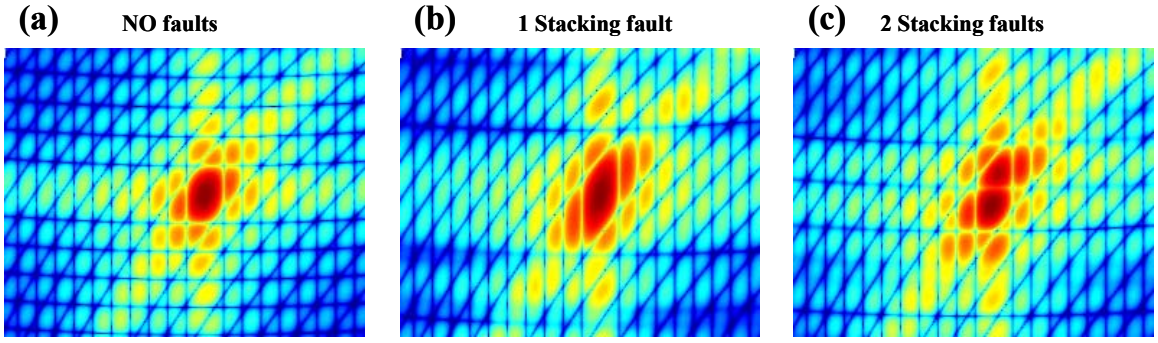

Figure 7-5 Small area of the scattering sphere around the (200) Bragg maxima, corresponding to the diffraction peak from the (200) planes of Fig. 7-4. (a) Ideal crystal with no stacking faults. (b) Single stacking fault in the middle of the CCA. (c) Two stacking faults located at 15 and 29 layers.

Inserting the single stacking fault in the middle of the CCA increases the width of the diffraction spot in Fig. 7-5(b) relative to the CCA without the stacking faults in Fig. 7-5(a). The

increase of the width is the simple result of the smaller number of diffracting layers contained in the crystal part of ABC type. When the CCA has a two stacking faults, the interference between the two parts of ABC type results in the splitting of the (200) spot into two, illustrated in Fig. 7-5(c).

The calculated diffraction spectrum of Fig. 7-4 can be used to explain the colors of the CCA's under ordinary lighting conditions. Imagine that we position the observer's eye to look at the CCA along the (200) direction. In the situation where there is diffuse white light incident to a CCA at every direction, only the light with frequencies corresponding to the peaks of the spectrum in Fig. 7-4 will reach the eye. Thus, the observed color would be determined by the combination of light frequencies from all peaks of the spectrum.

In this chapter we studied the effect of stacking faults on the diffraction by a CCA's. We subdivided all possible cases into two classes: the first, with Miller indices satisfying the condition $h+k+l=3n$, where there is no effect of the stacking faults at the Bragg directions. Other crystal planes are strongly affected by stacking faults, resulting in decreased diffraction efficiencies and broadened diffraction spots. However, the change of diffraction efficiencies due to the stacking faults is the same for different planes.

APPENDIX C

Kinematic 1D theory.

We developed a 1D analog of KNM theory and used these formulas to investigate the role of multiple scattering in the 1D case by comparing the result to the exact expressions for scattering intensities of a 1D slab system. We assume that each unit cell is the combination of two physical

layers, one with high and another with low refractive index. This two physical layers form a repeating unit cell of the relevant 1D periodic structure.

We assume that our 1D slab system consists of N units each of length d. In KNM theory, we further assume there is no extinction of the incident propagating wave; amplitude remains constant everywhere inside the system. Then far-field scattering amplitude is single unit scattering factor r_1 times the phase factor $e^{i\overrightarrow{\Delta k}\cdot\vec{d}}$ summed over all N units as geometric series. We obtain for the total scattered amplitude r:

$$|r|^2 = |r_1|^2 \frac{\sin^2(\frac{1}{2} N \cdot \vec{d} \cdot \overrightarrow{\Delta k})}{\sin^2(\frac{1}{2} \cdot \vec{d} \cdot \overrightarrow{\Delta k})}$$

We calculate single cell scattering factor r_1 by using exact Transfer Matrix 1D theory applied to a single dielectric layer.

APPENDIX D

Exact solution by the transfer matrix method for the problem of light scattering by 1D periodic layers system.

We solved Maxwell equations for 1D layered (along z) system by the standard transfer matrix method [76]. Reflection and transmission coefficients can be obtained by solving Maxwell equations for either the H or E field. Here we examine it for the H field. In the case of TM modes (magnetic field H vector is parallel to the interface between layers) we solve the wave equation for the H(z) field:

$$\left(-\frac{1}{\varepsilon}\frac{\partial^2}{\partial z^2}+\frac{k_x^2}{\varepsilon}\right)H(z)=\left(\frac{\omega}{c}\right)^2 H(z)$$

The solution for the magnetic field inside each layer can be represented as a combination of two plane waves, one is in the forward and another is in the backward direction:

$$H_n(z)=A_n\cdot e^{i\alpha_1 z}+B_n\cdot e^{-i\alpha_1 z}$$

For a layered 1-D system consisting of a finite number of identical unit cells (each unit cell contain two layers) we can connect coefficients A_n and B_n for two arbitrary cells. For example, we can connect cell n=0 and cell n=N separated by N cells with the matrix equation:

$$\begin{pmatrix}A_0\\B_0\end{pmatrix}=\underline{\underline{L}}^N\cdot\underline{\underline{T}}^*(\alpha_1,Nd)\cdot\begin{pmatrix}A_N\\B_N\end{pmatrix}$$

where $\underline{\underline{L}}$ and $\underline{\underline{T}}$ are 2x2 matrices (the exact expression for these matrices are complex and can be found in reference [76], where d is the unit cell length and $\alpha_1=\sqrt{\left(\omega/c\right)^2\cdot\varepsilon_1-k_x^2}$.

The exact result for the transmission r and reflection t amplitudes then can be obtained from:

$$\begin{pmatrix}1\\r\end{pmatrix}=\underline{\underline{L}}^N\cdot\underline{\underline{T}}^*(\alpha_1,Nd)\cdot\begin{pmatrix}t\\0\end{pmatrix}$$

The reflection intensity $|r|^2$ can be calculated by

$$|r|^2=\frac{L_{12}L_{21}}{L_{12}L_{21}+\left(\dfrac{\lambda_1-\lambda_2}{\lambda_2^{\,N}-\lambda_2^{\,N}}\right)^2}\quad ,$$

where λ_1 and λ_2 are the eigenvalues of matrix $\underline{\underline{L}}$. The reflection coefficient r_1 (used in 1D kinematic theory) for just one cell is obtained by

$$|r_1|^2=\left|\frac{L_{21}}{L_{11}}\right|$$

In the case of TE modes we can solve a similar wave equation but for the E electric field vector, resulting in slightly different matrix elements for matrix $\underline{\underline{L}}$ but otherwise the same formulas for the reflection and transmission coefficients.

APPENDIX E

Scattering of light by single sphere.

It is well known that when a plane electromagnetic wave is scattered by a dielectric sphere, it is possible to obtain exact analytical solution for the scattered intensity by solving Maxwell equations [65-66].

When an incident plane wave of amplitude E_0 is polarized along the *x* axis we can calculate the single sphere 3D scattering amplitude $\vec{E}_s(r,\theta,\varphi)$ (form factor $\vec{F}_j(\vec{r})$ for sphere j in formula 1) as a function of spherical coordinates *r*, θ and φ with the coordinate origin at the sphere center as

$$\left|\vec{E}_s(r,\theta,\varphi)\right|^2 = \frac{{E_0}^2}{kr}\left[{S_1}^2(\theta)\cos^2(\varphi) + {S_2}^2(\theta)\sin^2(\varphi)\right]$$

Asymptotic far-field expressions for parallel and perpendicular polarization scattered effective intensities $|S_1|^2$ and $|S_2|^2$ are given by

$$S_1(\theta) = \sum_{n=1}^{\infty}\frac{2n+1}{n(n+1)}\left(a_n\frac{P_n^1(\cos(\theta))}{\sin(\theta)} + b_n\frac{dP_n^1(\cos(\theta))}{d\theta}\right), \quad S_2(\theta) = \sum_{n=1}^{\infty}\frac{2n+1}{n(n+1)}\left(b_n\frac{P_n^1(\cos(\theta))}{\sin(\theta)} + a_n\frac{dP_n^1(\cos(\theta))}{d\theta}\right)$$

where P_n^l are associated Legendre polynomials, and the expressions for the scattering coefficients a_n and b_n can be found, for example, in [65-66].

The extinction cross-section of the single sphere can be obtained as

$$C_{ext} = \frac{4\pi}{k^2}\mathrm{Re}\{S(0°)\}$$

where the scattering coefficient $S(0°) = S_1(0°) = S_2(0°)$ is taken in forward direction at $\theta = 0°$. The ratio between the extinction cross section and the sphere cross-sectional area projected onto a plane perpendicular to the incident beam is called the extinction efficiency and is equal to:

$$Q_{ext} = \frac{C_{ext}}{\pi a^2}$$

for a sphere of radius *a*.

BIBLIOGRAPHY

[1] E. Yablonovich, Phys. Rev. Lett. **58**, 2059 (1987).

[2] S. John, Phys. Rev. Lett. **58**, 2486 (1987).

[3] J.D. Joannopoulos, R.D. Meade and J.N. Winn, *"Photonic Crystals: Molding the Flow of Light"*, (Princeton Univ. Press, Princeton, NJ, 1995). *"Photonic Band Gap Materials"*, edited by C.M. Soukoulis (Kluwer, Dordrecht, 1996).

[4] S. Y. Lin, E. Chow, V. Hietala, P. R. Villeneuve, J. D. Joannopoulos, Science **282**, 274 (1998).

[5] G. A. Ozin and S. M. Yang, Adv. Funct. Mater. **11**, 95, (2001).

[6] S. Noda, K. Tomoda, N. Yarnamoto, and A. Chutinan, Science, **289**, 604 (2000).

[7] A. Blanco, E. Chomski, S. Grabtchak, M. Ibisate, S. John, S. W. Leonard, C. Lopez, F. Meseguer, H. Mıguez, J. P. Mondia, G. A. Ozin, O. Toader, and H. M. van Driel, Nature **405**, 437 (2000).

[8] S. John, Phys. Today **44**, 32 (1991).

[9] E. Yablonovitch, J. Opt. Soc. Am. B **10**, 283 (1993).

[10] S. Y. Lin, J. G. Fleming, D. L. Hetherington, B. K. Smith, R. Biswas, K. M. Ho, M. M. Sigalas, W. Zubrzycki, S. R. Kurtz, J. Bur, Nature **394**, 251 (1998).

[11] J. E. G. J. Wijnhoven and W. L. Vos, Science **281**, 802 (1998).

[12] A. Blanco, E. Chomski, S. Grabtchak, M. Ibisate, S. John, S. W. Leonard, C. López, F. Meseguer, H. Míguez, J. P. Mondia, G. A. Ozin, O. Toader, H. M. van Driel, Nature **405**, 437 (2000).

[13] S. John and R. Rangarajan, Phys. Rev. B **38**, 10101 (1988).

[14] Y. Xia, B. Gates, Z.Y. Li, Adv. Mater. **13**, 409 (2001).

[15] K. Busch, and S. John, Phys. Rev. E **58**, 3896 (1998).

[16] M. Maldovan, C. K. Ullal, W. C. Carter and E. L. Thomas, Nat Mater **2**, 664 (2003).

[17] K. M. Ho, C. T. Chan, C. M. Soukoulis, Phys. Rev. Lett. **65**, 3152 (1990).

[18] E. Yablonovitch, T. J. Gmitter and K. M. Leung, Phys. Rev. Lett. **67**, 2295 (1991).

[19] Z.-Y. Li, J.Wang, B.-Y. Gu, J. Phys. Soc. Jpn. **67**, 3288 (1998).

[20] Y. Xia, B. Gates, and Z. Y. Li, Adv. Mater. **13**, 409 (2001).

[21] O. Toader, T. Y. M. Chan, S. John Phys. Rev. Lett. **92**, 043905 (2004).

[22] S.A. Asher, "Adventures with Smart Chemical Sensing; Electrooptically Responsive Photonic Crystals", Nanoparticles: Building Blocks for Nanotechnology, Rotello, V.M., ed. Kluwer: New York, 145-172 (2004).

[23] J. Broeng, D. Mogilevstev, S. E. Barkou, and A. Bjarklev, Opt. Fiber Technol. **5**, 305 (1999).

[24] P. R. Villeneuve, D. S. Abrams, S. Fan, and J. D. Jonannopoulos, Opt. Lett. **21**, 2017 (1996).

[25] S. A. Asher, G. Pan, and R. Kesavamoorthy, Nonlinear Optics **21**, 343 (1999).

[26] J. D. Rancourt, "Optical thin films: user handbook" (Bellingham, USA, SPIE Optical Engineering Press, 1996).

[27] J. S. Foresi, P. R. Villeneuve, J. Ferrera, E. R. Thoen, G. Steinmeyer, S. Fan, J. D. Joannopoulos, L. C. Kimerling, H. I. Smith, E. P. Ippen, Nature **390**, 143, (1997).

[28] S. Noda, K. Tomoda, N.Yamamoto, and A. Chutinan, Science **289**, 604 (2000).

[29] S. Ottow, V. Lehmann, and H. Foll, Appl. Phys. A: Mater. Sci. Process. **63**, 153 (1996).

[30] M. Campbell, D. N. Sharp, M. T. Harrison, R. G. Denning and A. J. Turberfield, Nature **404**, 53 (2000).

[31] M., F. Holgado, Garcıa-Santamarıa, A. Blanco, M. Ibisate, A. Cintas, H. Mıguez, C. J. Serna, C. Molpeceres, J. Requena, A. Mifsud, F. Meseguer, and C. Lopez, Langmuir, **15**, 4701 (1999).

[32] Yu. A Vlasov, V. N. Astratov, A. V. Baryshev, A. A. Kaplyanskii, O. Z. Karimov, and M. F. Limonov, Phys. Rev. E **61**, 5784 (2000).

[33] Y. Xia, B. Gates, Y. Yin, and Y. Lu, Adv. Mater. **12**, 693 (2000).

[34] J. E. G. J. Wijnhoven, and W. L. Vos, Science **281**, 802 (1998).

[35] B. T. Holland, C. F. Blanford, A. Stein, Science **281**, 538 (1998).

[36] R. J. Carlson, S. A. Asher, Appl. Spectrosc. **38**, 297 (1984).

[37] R. D. Pradhan, J. A. Bloodgood and G. H. Watson, Phys. Rev. B **55,** 9503 (1997).

[38] E. Yablonovitch, T. J. Gmitter and K. M. Leung, Phys. Rev. Lett. **67**, 2295 (1991).

[39] K. M. Ho, C. T. Chan and C. M. Soukoulis, Phys. Rev. Lett. **65**, 3152 (1990).

[40] M. Doosje, B. J. Hoenders, and J. Knoester., Optics Communications **206**, 253 (2002).

[41] E. E. Istrate, A. A. Green, and E. H. Sargent, Phys. Rev. B **71**, 195122 (2005).

[42] J. B. Pendry, J. Phys.: Condens. Matter, **8**, 1085 (1996).

[43] M. Sigalas, C. M. Soukoulis, E. N. Economou, C. T. Chan, and K. M. Ho, Phys. Rev. B **48**, 14121 (1993).

[44] J. B. Pendry, J. Mod. Opt. **41**, 209 (1994).

[45] L.C. Botten, N.A. Nicorovici, R.C. McPhedran, C. Martijn de Sterke, and A.A. Asatryan, Phys. Rev. E **64**, 046603 (2001).

[46] Z-Y Li and L-L Lin, Phys. Rev. E **67**, 046607 (2003).

[47] N. Stefanou, V. Karathanos and A. Modinos, J. Phys.: Condens. Matter **4,** 7389 (1992).

[48] K. Ohtaka and Y. Tanabe, J. Phys. Soc. Jpn. **65**, 2265 (1996).

[49] G. Gantzounis and N. Stefanou, Phys. Rev. B **73**, 035115 (2006).

[50] L. Braginsky and V. Shklover, Phys. Rev. B **73**, 085107 (2006).

[51] O. Painter, K. Srinivasan, and P. E. Barclay, Phys. Rev. B **68**, 035214 (2003).

[52] M. I. Mishchenko, L. D. Travis, and A. A. Lacis, "Scattering, Absorption, and Emission of Light by Small Particles", (Cambridge University Press, Cambridge 2002).

[53] F.M. Kahnert, J. Quant. Spectrosc. Radiat. Transfer, **79–80,** 775 (2003).

[54] T. Wriedt, Part. Part. Syst. Charact. **15**, 67 (1998).

[55] A. J. Ward and J. B. Pendry, Physical Review. B. **58**, 7252 (1998).

[56] E Moreno, D Erni, C Hafner, Physical Review B, **65,** 155120 (2002).

[57] O. J. F. Martin, C. Girard, D.R.Smith and S. Schultz, Phys. Rev. Lett. **82**, 315 (1999).

[58] D. W. Mackowski, and M. I. Mishchenko, J. Opt. Soc. Am. A, **13**, 2266 (1996).

[59] Y. Xu, App. Opt., **36**, 9496 (1997).

[60] H. Kimura, L. Kolokolova, and I. Mann, A&A, **449**, 1243 (2006).

[61] "Photonic crystals and light localization in the 21st century", edited by C.M. Soukoulis (Kluwer Academic Publishers, Dordrecht, 2001).

[62] Proceedings of the NATO ASI "Wave Scattering in Complex Media: From Theory to Applications", ed. B. van Tiggelen and S. Skipterov (Kluwer, Dordrecht, 2003).

[63] A. F. Koenderink and W. L. Vos, Phys. Rev. Lett. **91**, 213902 (2003).

[64] A. Yu. Sivachenko, M. E. Raikh, and Z. V. Vardeny, Phys. Rev. B. **63**, 245103 (2001).

[65] H. C. van de Hulst, "Light Scattering by Small Particles" (Dover, New York, 1957);

[66] C. F. Bohren and D. R. Huffman, "Absorption and Scattering of Light by Small Particles" (John Wiley and Sons, Inc. N.Y., N. Y., 1983).

[67] L. Tsang, J. A. Kong, and K.-H. Ding, "Scattering of Electromagnetic Waves: Theories and Applications" (Wiley-Interscience, New York, 2000).

[68] R.W. James, "The optical principles of the diffraction of X-Rays" (G.Bell and Sons LTD, London, 1962).

[69] W. H. Zachariasen, "Theory of X-Ray Diffraction in Crystals" (Dover, New York, 1945).

[70] D. M. Mittleman, J. F. Bertone, P. Jiang, K. S. Hwang and V. L. Colvin, J. Chem. Phys. **111**, 345 (1999).

[71] P. A. Rundquist, P. Photinos, S. Jagannathan, and S. A. Asher, J. Chem. Phys. **91**, 4932 (1989).

[72] W. L. Vos, R. Sprik, A. van Blaaderen, A. Imhof, A. Lagendijk, and G. H. Wegdam, Phys. Rev. B **53**, 16231 (1996).

[73] R. M. Amos, J. G. Rarity, P. R. Tapste, T. J. Shepherd, and S.C. Kitson, Phys. Rev. E **61**, 2929 (2000).

[74] S. A. Asher, J. M. Weissman, A. Tikhonov, R. D. Coalson, and R. Kesavamoorthy, Phy. Rev. E. **69**, 066619 (2004).

[75] M.Inoue, K. Ohtaka and S.Yanagawa, Phys. Rev. B **25**, 689 (1982)

[76] P. Yeh, A. Yariv, and C.-S. Hong, J. Opt. Soc. Am. **67**, 423 (1977).

[77] L.V. Woodcock, Nature (London) **388**, 236 (1997).

[78] V. Yannopapas, N. Stefanou and A. Modinos, Phys. Rev. Lett. **86**, 4811 (2001).

[79] E. Estevez-Rams, B. Aragon-Fernandez, H. Fuess, and A. Penton-Madrigal, Phys. Rev. B **68**, 064111 (2003).

[80] R. Berliner and S. A. Werner, Phys. Rev. B **34**, 3586 (1986).

[81] D. P. Varn, G. S. Canright, and J. P. Crutchfield, Phys. Rev. B **66**, 174110 (2002).